Assessing precision and accuracy in acoustic scattering matrix measurements

LUCK PEERLINGS

Doctoral Thesis
Stockholm, Sweden, 2017

Sammanfattning

Akustiska spridningsmatriser används för att beskriva inverkan av olika element på ljudutbredning i vågledare. När man experimentell bestämmer akustiska egenskaper hos dessa matriser, är det ofrånkomlig att det finns fel i mätresultat och om man ska kunna bestämma överenstämmelsen mellan modeller och mätningar måste felen kunna beskrivas.

I denna avhandling undersökas effekten av slumpmässiga och systematiska fel i mätningen av akustiska spridningsmatriser. Olika aspekter av mätprocessen undersökas, med början i beskrivningen av noggrannheten i uppmätta komplexa ljudtryck. Därefter behandlas beskrivningen av slumpmässiga fel på spridningskoefficienterna. Dessa koefficienter är beräknade från mätdata och felet i mätdata måste propageras till koefficienterna. Detta görs med noggranhetsanalyser och användningen av linjära metoder för att bestämma osäkerheten i koefficienterna undersöks.

Impedansröret är en väsentlig del vid experimentell bestämning av akustiska spridningsmatriser och tredje delen behandlar beskrivningen av systematiska felet som kan uppstår vid mätningar i impedansrör. Inverkan av systematiska fel på mätresultat visas och metoder att minska systematiska fel presenteras. Det visar sig att det finns resterande systematiska fel och källor till dessa fel diskuteras.

De erhållna kunskaperna används sedan för att bestämma strömningsakustisk växelverkan vid ett areasprång med hjälp av spridningsmatriser. Den uppmätta absorptionen stämmer kvalitativ med teoretiskja modeller, men skillnaden mellan modellerna och mätningar är större än mätningarnas konfidensintervall. Ändkorrektionen stämmer väl överens med modellerna vid högre Strouhaltal, men vid lägre Strouhaltal är spridningen i uppmätta data för stor for att identifiera inverkan av strömningakustisk växelverkan på ändkorrektionen.

Nyckelord: strömningsakustik, areasprång, akustik i vågledare, akustiska spridningsmatriser, impedansrör, noggrannhetsanalys, systematiska fel.

Abstract

Acoustic scattering matrices are used to characterize the influence of inline duct elements on the acoustic wave propagation in wave guides. When measuring the properties of these matrices, errors are always present in the results and need to be characterized to make valid statements on the correspondence between model predictions and measurements.

In this study the random and systematic errors in acoustic scattering matrix measurements are investigated. Several aspects of the measurement cycle are examined, starting with the determination of the random error on the measured transfer functions between the acoustic source signal and the measured acoustic pressure.

The second aspect is the determination of the random error on the scattering matrix coefficients. They are mathematically derived from the measurement data and the error has to be propagated from the data to the coefficients. This is done using uncertainty analyses and the use of linear methods to calculate the uncertainty of the coefficients is investigated.

The impedance tube is an essential element of acoustic scattering matrix measurements and the third topic is a description of the systematic errors that can occur in these tubes. The effect of various systematic errors are shown, together with methods to account or reduce them. It is shown that there are still systematic errors remaining, and hypotheses to the source of these errors are discussed.

In the last part, the knowledge is put to use to measure the aero-acoustic interaction present at a sudden area expansion. It is shown that the measured acoustic absorption agrees qualitatively with the models, however the deviation between the measurements and predictions are larger than the uncertainty of the measurements. The end correction agrees well with the models at high Strouhal numbers, but the scatter on the measurements at lower Strouhal numbers is too large to identify flow-acoustic interaction effects on the end correction.

Keywords: aero-acoustics, sudden area expansion, in-duct acoustics, Acoustic scattering matrix, impedance tube, uncertainty analysis, systematic errors.
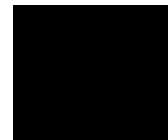
Contents

Contents

CHAPTER 1

Introduction

Acoustic noise is a nuisance that everybody experiences in their daily life. To effectively reduce it, the creation and propagation of noise has to be understood and the understanding comes through the modelling of these phenomena. To verify that the modelling is correct, the results have to compared against accurate experimental observations.

Noise pollution has long been recognized as affecting the quality of life and well being. According to a recent report of The World Health Organization [1], noise is the second worst environmental cause of ill health, only behind ultra-fine particulate matter. In the European Union, road traffic is the most dominant source of environmental noise, followed by railway noise and air traffic noise. In the Seventh Environment Action Programme, the European Union has committed itself to significantly decrease the noise pollution in the European Union and move closer to levels recommended by the World Health Organization [2].

Vehicles are the largest contributor to environmental noise and their internal noise sources are often encapsulated, with distinct openings to the outside world. Usually these openings are used to exchange fluids with the environment and examples are automotive mufflers, cooling intakes of trains and in- and outlets of aircraft engines.

The fluid flow to and from the internal noise sources can be confined by ducts, which act as waveguides for the acoustic disturbances. These ducts can contain discontinuities, such as bends, side branches and area expansions at which the fluid may separate. When there is flow separation, a pathway is opened for the acoustic field to interact with the hydrodynamic field and energy can be exchanged between the fields. This acoustic-hydrodynamic interaction can significantly alter the prevailing wave fields in the ducts, and need to be taken into account to describe the noise radiating from the vehicle to the environment.

The interaction between fluid flow and acoustics is known as aero-acoustics and the beginning of the field is marked by the pioneering work by Sir James Lighthill, more than half a century ago [3]. The field of aero-acoustics has been intensively studied for more than 6 decades and consequently, the major mechanisms of the acoustic hydrodynamic interactions have been identified and model improvements only lead to a relatively small changes on the predictions. For the experimentalist, it becomes increasingly more difficult to obtain results that can confirm whether model results are valid, as the differences between the various models approach the size of the experimental errors. To still infer reliable conclusions of the agreement between model and experiments, it is important that the effect of errors on the measurements are assessed.

Acoustic disturbances travel as waves and when these disturbances are confined by ducts, their vibrational pattern in the cross section of the duct is limited to a finite number of modes. When the propagation of the acoustic wave is impeded by the presence of duct irregularities, only a part of the wave is transferred to the other side, whereas a part of the wave is reflected back. A convenient way to describe this scattering is the acoustic scattering matrix. It relates the acoustic waves propagating toward the discontinuity, to the acoustic waves travelling away from the discontinuity.

A well defined problem where aero-acoustic interaction is present is the sudden area expansion. When a fluid flow passes the sudden area expansion, flow separation occurs and the acoustic field interacts with the hydrodynamic field. A variety of models have been created which characterize the interaction using the acoustic scattering matrix, but the experimental evidence is scarce. The goal of this thesis is to obtain reliable data of this interaction in the form of scattering matrices, to achieve it is imperative that the measurements errors on the results are accurately assessed.

1.1 Description of errors

Errors on measurements can be classified in two broad categories, random errors and systematic errors. These two categories are also indicated by resp. precision and accuracy and a pictorial representation of the categories is given in figure 1.1. Random errors occur through stochastic effects on the measurements and if the measurement would be repeated an infinite amount of time, the true value would be obtained from the average of these measurements. Systematic errors on the other hand cause a deviation of the measured value from the true value and are deterministic in nature. Performing multiple measurements will give the same measured value.

Stochastic errors on measurements can be quantified using an uncertainty analysis. The basis of the uncertainty analysis is to systematically describe the errors that occur during the
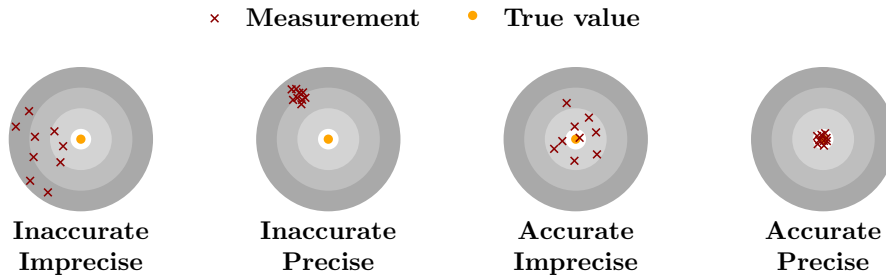
Figure 1.1: *Pictorial representation of the accuracy and precision of a measurement.*

measurements and propagate them through the function that relates the measured values, also called the measurands, to the value that is of interest. The stochastic error is often described with uncertainty intervals and the size of the interval depends on the standard deviation and the desired confidence level. The standard deviation is defined as the square root of the variance of the measured value and is sometimes also referred to as the standard uncertainty. The confidence level gives the relative proportion of intervals that will contain the true value, when the experiment would be repeated an infinite amount.

To identify and reduce the systematic error, a systematic approach has to be taken, represented schematically in figure 1.2. The systematic error that is present can only be assessed by performing a calibration measurement. With such a measurement, a calibration standard of known accuracy is measured. The deviation between the measured value and the calibration standard indicates the presence of an error, but not the origin of it. By performing an uncertainty analysis on the measured results, the contribution of stochastic errors can be assessed using the confidence intervals. If the deviation between the measurement and the calibration standard is small compared to the confidence intervals, the stochastic error dominates. The major contributors to the stochastic error can then be identified with the uncertainty analysis and the measurements can be improved by reducing these error sources.

On the other hand, if the measurements are repeatable and the size of the deviation is much larger than the confidence interval, a systematic error is present. To identify the systematic error, the source of error has to be hypothesized and measurements performed to test the hypothesis. When a source of error is identified, it can be reduced or taken into account in the measurement analysis. This procedure has to be repeated until the obtained deviations are acceptable.
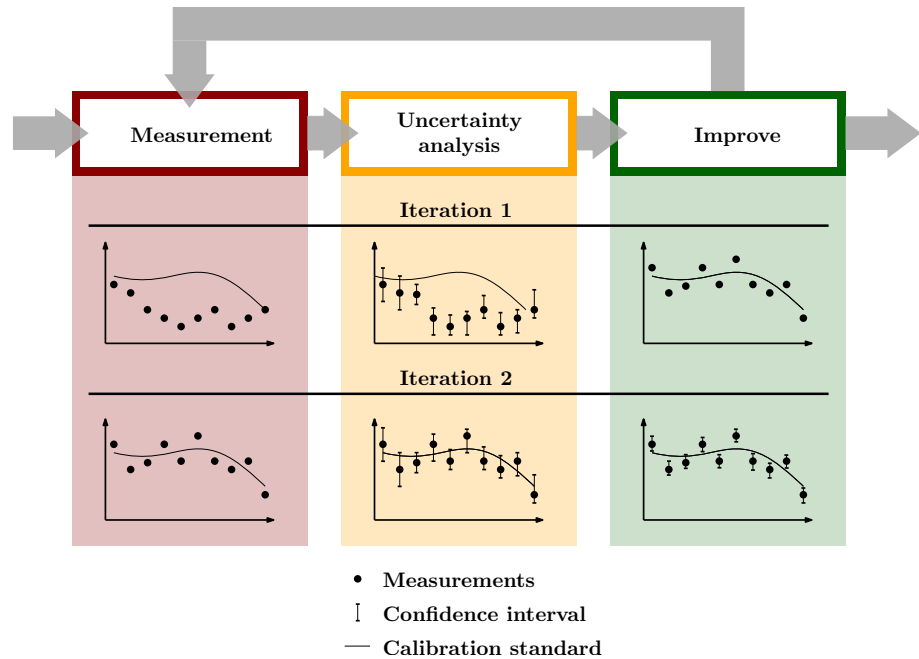
Figure 1.2: *Pictorial representation of the error reduction workflow.*

1.2 Thesis outline

To reach the stated goal of the thesis, several aspects of the errors and their analysis in acoustic scattering matrices will be investigated. The studies presented in this thesis can be summarized in four questions:

- *How can the stochastic error on transfer functions measured with stepped sine excitation be determined?*

- *Are linear uncertainty analyses appropriate to quantify the stochastic errors on measured scattering matrices?*

- *Which systematic errors are present in acoustic impedance tubes?*

- *Do measurements agree with recent predictions of the area-acoustic interaction at an area expansion?*

In the first part (chapter two) a method to determine the stochastic error on measured transfer functions is discussed. The transfer function for a system with noise on the output and a harmonic signal as input is determined using a method based on synchronous

demodulation. The random error on the transfer function is characterized with the auto spectral density of the noise and the expressions are validated against experiment.

The general acoustic theory is briefly reviewed in chapter three. The mathematical description for waves travelling in waveguides is given and the concept of the acoustic scattering matrix is introduced. In chapter four, the use of linear uncertainty analyses to determine the random error on the acoustic scattering matrix as function of the random error on the measurements is investigated. The results are compared against a non-linear uncertainty analysis and is shown that the linear uncertainty analysis can only be used in specific cases.

The accuracy of the scattering matrix measurements is determined in the fifth chapter by measuring the acoustic reflection coefficient of a calibration standard. Various systematic errors are identified and the influence and methods to reduce these errors are discussed. After the systematic errors have been accounted for, there is still a discrepancy between the measurements and the calibration standard The sixth chapter discusses these systematic error and two general trends are identified. Several hypotheses of the origin of the error are discussed and the discussion shows the probable sources of errors.

In the seventh chapter, the measurements of the aero-acoustic interaction at the area expansion are given. Using the methods and theory presented in the previous chapters, the accuracy of the measurements is shown to be good and the precision assessed using the linear uncertainty analysis. The results are compared against recent models.

The last chapter concludes the thesis with an overview of the contributions and achievements.

1.3   Contributions and division of work

The main contributions of the thesis can be found in chapter 2, 4, 6, 7.

In chapter 2 a novel method to estimate the uncertainty of measured transfer functions from the background spectrum is proposed and compared with experimental data. In chapter 4, a thorough investigation of linear methods to express the uncertainties in measured scattering matrices is performed and compared with Monte-Carlo simulations. In chapter 6, a thorough discussion of the prevailing systematic error in impedance tubes is given. Various hypotheses of the error are tested and probable error sources are given. In chapter 7, new experimental data for aero-acoustic interaction at an area expansion is presented and compared with recent models.

Luck Peerlings initiated the direction and performed the studies, the measurements, made the analysis and produced the thesis. Hans Bodén and Susann Boij supervised the work, discussed ideas and reviewed the work.

Introduction

During the study, research visits where made to the Laboratoire d'Acoustique de l'Université du Maine (LAUM) in Le Mans, France and the Deutsches Zentrum für Luft- und Raumfahrt in Berlin, Germany. At the LAUM, Yvés Auregan supervised the work and discussed ideas. These contributions are mainly incorporated in chapter 5 and 6. Friedrich Bake supervised the research visit to the DLR in Berlin and discussed ideas. These contributions can be found in chapter 4, 5 and 6.

CHAPTER 2

Estimating the statistical parameters of transfer functions based on the background signal

In this chapter the determination of the variance of transfer functions is investigated. Using the synchronous demodulation technique, expressions for the variance and kurtosis of the real and imaginary part of the transfer functions are obtained for various noise models. The expressions are validated against experimental results and it is shown that it is possible to determine the variance and kurtosis of the transfer functions solely based on the auto spectral density of the noise. Also, using the derived expressions, the commonly made assumptions on the measured transfer functions, that is that the imaginary and real part are uncorrelated and that their variance are of equal magnitude is analyzed. It is shown that these assumptions can be violated when strong tonal components are present in the background signal.

2.1   Introduction

Recently, the application of statistical methods to determine the uncertainty in acoustic measurements within ducts has gained interest [4–6]. These methods propagate the uncertainty of the measured quantities to the quantities of interest. To apply such an analysis, the probability density functions and statistical parameters of the measured data have to be determined accurately.

As acoustic measurements are often analysed in the frequency domain, one important quantity in such measurements are transfer functions between electric and acoustic signals. In the case of flow duct acoustics, the flow noise has a large contribution in the measured pressure signal and to obtain good signal to noise ratios, single sine excitations are often used to determine the transfer functions.

The statistical properties of the transfer function can be inferred from the coherence between the input and output signal [7] under the assumption that the random error in the transfer function is normally distributed and has equal variance for the real and imaginary part and that the real and imaginary part are uncorrelated. Auweraer et al. [8] review the stepped sine measurements and briefly addresses the uncertainty in the estimates and shows that the estimation error is inversely proportional to the square root of the measurement time. Pintelon et al. [9] show that exact confidence intervals of frequency response functions measurements for arbitrary input/output noise signal to noise ratios can be computed when the input and output noise are circular complex normally distributed. Schultz et al. [10] demonstrate the use of a multivariate statistical analysis to describe the uncertainty in measured transfer functions. The real and imaginary parts are treated as two separate uncertain variables and the error on the measured transfer functions is determined from the measured cross spectra.

To apply the above methods, several assumptions have to be made about the errors, such as they are normally distributed, the real and imaginary part are uncorrelated and the variance of the real and imaginary part are equal. These assumptions have to be verified and to do so enough statistically independent measurements have to be taken of a transfer function.

On the other hand, obtaining enough statistically independent samples could lead to too long measurement times which could jeopardize the time invariant behaviour of the system. Therefore, a single measurement is often taken and the statistical properties of the final results are determined by dividing the measurement data in separate samples and averaging the results. It is possible that the underlying assumptions are violated, due to the short measurement time of a single sample. In these cases, the obtained statistical parameters, such as the variance, have a different relation to the uncertainty in the measurement because the underlying probability density function is not a normal distribution.

In this chapter a different approach is investigated to obtain the statistical properties. When measuring the transfer function using a stepped sine signal, the relation between the input signal and output signal is deterministic, when there is no added noise at the output signal. The addition of noise makes the measured transfer function stochastic and thus the stochastic properties are defined by the properties of the noise signal.

The goal of this chapter is to determine the stochastic properties of the transfer func-
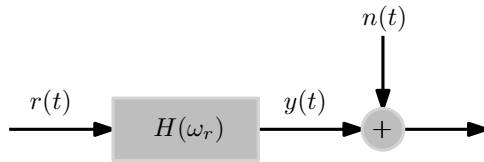
Figure 2.1: *Schematic representation of the single input, single output system.*

tion with the information of the noise signal. First, the relation between the variations in the measured transfer function and the noise is determined in the time domain using the synchronous demodulation technique [11]. Thereafter, three models are introduced for the noise, for which the parameters only dependent on the auto spectral density of the noise. With the help of the noise models, the variance and kurtosis are determined as function of the auto spectral density. The variance gives information on the spread of the estimated transfer functions and the kurtosis on the shape of the probability density function of the transfer function estimates. To construct confidence intervals, the probability density function should be known and it is common to assume that the distribution follows a normal distribution, but with the help of the kurtosis this assumption can be checked. The relation for the variance and kurtosis are validated against measurements, showing a good agreement between the predicted and measured statistical properties.

2.2 Theory

The theory is based on a linear, time invariant, single input, single output system with noise $n(t)$ on the output, as shown in figure 2.1. The input is to be considered to be a harmonic signal, with an angular frequency of ω_r, $r(t) = A_r \cos \omega_r t$. The output $y(t)$ is of the form $y(t) = A_y \cos \left[\omega_r t + \theta_y \right]$ and the relation between the input and output is given by the true transfer function $H(\omega)$.

An estimate of the true transfer function, $\tilde{H}(\omega)$, at the frequency ω can be obtained in the continuous time domain using the concept of synchronous demodulation and the analytic representation of the input [11].

The idea is that the reference signal consists of a harmonic signal with a slowly varying instantaneous amplitude and frequency. By multiplying the measurement signal with a reference signal that has two components that are orthogonal with each other, e.g. a real and a complex part, the result will be the projection of the measurement signal on both components of the reference signal. This approach gives then the in-phase and the out-of-phase part of the measurement signal w.r.t. the reference signal.

To represent a (random) signal in the complex domain such that it has two orthogonal components, the signal has to be transformed to a so-called analytic signal $\hat{x}(t)$. The analytic signal allows for an arbitrary signal $x(t)$ to represented by a time dependent amplitude $A(t)$ and phase $\psi(t)$, that is,

$$\begin{aligned} \hat{x}(t) &= x(t) + i\mathscr{H}\left[x(t)\right], \\ &= A(t)\exp\left[i\psi(t)\right], \end{aligned} \tag{2.1}$$

where $\mathscr{H}\left[x(t)\right]$ is the Hilbert transform of the signal $x(t)$ [11]. This phasor notation gives the time dependent information of the measured signal, $A(t)$ is the instantaneous amplitude (envelope) and $\psi(t)$ is the instantaneous phase of the measured signal. The relation between the instantaneous phase and the instantaneous frequency is given by [11]:

$$\omega(t) = \frac{d\psi}{dt}. \tag{2.2}$$

If the signal $x(t)$ is harmonic and the amplitude is time invariant, the analytic signal reduces to $\hat{x}(t) = A\exp[i\omega t]$.

If the system under study is linear, the response signal will also be a harmonic which has the same frequency (instantaneous phase) as that of the excitation signal. The amplitude $A_y(t)$ and phase $\phi(t)$ relative to the excitation signal may be time dependent and thus the measured signal, under the assumption that the noise on the output is not present $n(t) = 0$ can be written as:

$$y(t) = \frac{1}{2}A_y(t)A_r(t)\left(e^{i(\psi(t)+\phi(t))} + e^{-i(\psi(t)+\phi(t))}\right). \tag{2.3}$$

If the excitation signal is time independent and harmonic, the relation between the output and input can be obtained by dividing the measured signal with the reference,

$$\frac{y(t)}{r(t)} = \frac{1}{2}A_y(t)e^{i\psi(t)} + \frac{1}{2}A_y(t)e^{-i\psi(t)-2i\omega_r t}. \tag{2.4}$$

Consider now the case that the phase and relative amplitude between the excitation and measurement signal is time independent, $\partial A_y(t), \psi(t)/\partial t = 0$. Then the first term in equation (2.4) is time independent and the frequency of the second term is the double of the reference frequency. By taking the time average, an estimate of transfer function between the reference and the excitation signal is obtained at the specific frequency ω_r.

When noise is present on the measurement signal, the estimate of the transfer function is given by,

$$\tilde{H}(\omega_r) = \frac{2}{\tau}\int_0^\tau \frac{y(t)+n(t)}{\hat{r}(t)}dt, \tag{2.5}$$

where τ is the integration time [11]. When the noise is considered to be a random variable with zero mean, the expected value of the transfer function is given by,

$$\mathrm{E}\left[\tilde{H}\right] = \frac{2}{\tau} \int_0^\tau \frac{y(t)}{\hat{r}(t)} dt. \tag{2.6}$$

where the notation of (ω_r) has been omitted for concise writing. From here onward, this convention will be applied wherever possible.

Only when the integration time, τ is a multiple of half of the excitation frequency, the true transfer function $H(\omega)$ is obtained from equation (2.6),

$$\mathrm{E}\left[\tilde{H}\right] = H = \frac{2}{\tau} \int_0^\tau \frac{y(t)}{\hat{r}(t)} dt, \quad \text{when } \tau = \frac{\pi}{\omega_r}n;\ n \in \mathbb{Z}. \tag{2.7}$$

Otherwise a bias error will be introduced, as the double frequency term, (2.4), will contribute to the time average. In the remainder of the text the integration τ is considered to uphold the condition given in (2.7) such that the expected value is always the true value of the transfer function.

The deviation from the expected transfer function can then be written as,

$$\tilde{H} - \mathrm{E}\left[\tilde{H}\right] = \frac{2}{\tau} \int_0^\tau \frac{n(t)}{\hat{r}(t)} dt, \tag{2.8}$$

which shows that the variation is solely induced by the noise. With the above expression, the j-th and k-th order statistical moments with respect to the real and imaginary parts, $\mu_{j,k}$, can then be calculated,

$$\mu_{j,k} = E\left[\left(\Re\left[\tilde{H} - \mu_H\right]\right)^j \left(\Im\left[\tilde{H} - \mu_H\right]\right)^k\right], \tag{2.9}$$

where $\mu_H = \mathrm{E}\left[\tilde{H}\right]$, $\Re\left[\square\right]$ denotes the real part of $\square$ and $\Im\left[\square\right]$ denotes the imaginary part of $\square$. For ease of comprehension, the statistical moments with respect to only the real or imaginary part of the deviation, will be denoted by $\mu_{\Re,j}$ and $\mu_{\Re,k}$ respectively. If expressions are similar for both the imaginary and real part of the statistical moments, the notation $\mu_{\Re,\Im,k}$ is used to indicate the kth statistical moment for the real $\mu_{\Re,k}$ and the imaginary part $\mu_{\Im,k}$.

Noise models

To determine the statistical moments of the transfer function, a model for the noise $n(t)$ has to be given. Three models will be investigated. The first two models are commonly used in literature to describe random noise [12]. Both models have the property that their average value is zero and that the variance as function of frequency is equal to auto spectral
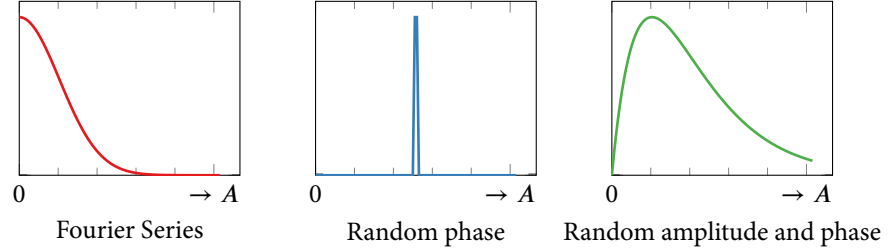
Figure 2.2: *Schematic representation of the probability density function of the amplitude as function of the amplitude for the various models.*

density function of $n(t)$. The first model is a Fourier series with normal random distributed coefficients and the second a Fourier series with a known amplitude and a random phase with uniform distribution. The third model uses a Fourier series with an amplitude that has a Gamma distribution and a phase with a uniform distribution. It is inspired by looking at the statistics of measured noise spectra of flow noise, for which the distribution resembled a Gamma distribution. To have an expected value of zero, the phase is chosen to have a uniform distribution. The probability density function of the Fourier coefficients of the three models are circular symmetric in the complex plane and in figure 2.2 a schematic overview of the probability density function of the amplitude as function of the amplitude is given for the three models. For all the models, it is assumed that the random variables associated to a single Fourier term are uncorrelated with the other Fourier terms. The first model is given by,

$$n(t) = \sum_{i=0}^{\infty} a_i \cos(\omega_i t) + b_i \sin(\omega_i t), \quad a_i, b_i \in \mathbb{N}(0, \sigma_i), \quad (2.10)$$

where the random variables a_i and b_i are normally distributed with a zero mean and a variance $\sigma_i = \sqrt{S_{nn}(\omega)\Delta\omega}$. Herein $S_{nn}(\omega)$ is the single sided auto spectral density of the noise and $\Delta\omega$ the frequency spacing of the consecutive Fourier coefficients of the spectrum.

The second model is given by,

$$n(t) = \sum_{i=0}^{\infty} C_i \cos(\omega_i t + \theta_i), \quad \theta_i \in \mathbb{U}(0, 2\pi). \quad (2.11)$$

Where c_i is the amplitude of the Fourier term and given by $c_i = \sqrt{2S_{nn}\Delta\omega}$. The phase, θ_i, is a random variable, for which the probability density function is uniform and the values are bounded by 0 and 2π.

The third model is given by

$$n(t) = \sum_{i=0}^{\infty} c_i \cos(\omega_i t + \theta_i), \quad \theta_i \in \mathbb{U}(0, 2\pi) \quad \text{and} \ c_i \in \text{Gamma}(\alpha_i, \beta_i), \tag{2.12}$$

where the phase of the Fourier terms, θ_i, is modelled as a random variable with a uniform probability density function over the interval $[0, 2\pi]$.

$$f(c_i; \alpha_i, \beta_i) = \frac{1}{\Gamma(\alpha)\beta^\alpha} c_i^{\alpha_i - 1} e^{-\frac{c_i}{\beta}}, \tag{2.13}$$

where α_i is the shape parameter, β_i the scale parameter and Γ the Gamma function. The shape and scale parameters can be estimated from the square root of the measured single sided power spectral density and its corresponding variance,

$$\alpha_i = \frac{\mathrm{E}\left[\sqrt{S_{nn}(\omega_i)}\right]^2}{\mathrm{Var}\left[\sqrt{S_{nn}(\omega_i)}\right]}, \quad \beta_i = \frac{\mathrm{Var}\left[\sqrt{S_{nn}(\omega_i)}\right]}{\mathrm{E}\left[\sqrt{S_{nn}(\omega_i)}\right]}. \tag{2.14}$$

2.3 Statistical moments

The effect of the noise on the determination of the transfer function can be determined using the introduced noise models. By introducing the noise models into the equation (2.8), the deviation from the true transfer functions due to the noise can be determined. From the obtained expressions, the statistical moments can be determined for the various noise models wit the help of equation (2.9).

In the following, the real and imaginary part of the variation from the expected transfer will be given for each of the noise models and the variance $\sigma^2_{\Re,\Im}$ will be determined,

$$\sigma^2_{\Re,\Im} = \mu_{\Re,\Im,2}. \tag{2.15}$$

The variance gives information on the variation of the measured transfer function, however to compute confidence intervals the probability density functions also has to be known.

It is often assumed that the probability density function is normally distributed, but with the help of the kurtosis that assumption can be strengthened and the kurtosis $\kappa_{\Re,\Im}$ of the real and imaginary part will also be determined,

$$\kappa_{\Re,\Im} = \frac{\mu_{\Re,\Im,4}}{\mu^2_{\Re,\Im,2}}. \tag{2.16}$$

For a normal distribution, the kurtosis equals 3. Care should be taken when interpreting the kurtosis estimate the underlying probability density functions, because if the measured

kurtosis equals 3 it does not automatically imply that the probability density function is normally distributed. The odd statistical moments will not be discussed, as they are zero for all the used models.

Fourier Series

For the Fourier Series, the real and imaginary part of the deviation from the expected transfer function are given by,

$$\Re\left[\tilde{H} - \mu_H\right] = \sum_{i=0}^{\infty} a_i \underbrace{\frac{2\omega_i \sin\left(2\tau\omega_i\right)}{A_r\tau\left(\omega_i^2 - \omega_r^2\right)}}_{A_{\Re,i}} + b_i \underbrace{\frac{2\omega_i\left(1 - \cos\left(2\tau\omega_i\right)\right)}{A_r\tau\left(\omega_i^2 - \omega_r^2\right)}}_{B_{\Re,i}}, \qquad (2.17a)$$

$$\Im\left[\tilde{H} - \mu_H\right] = \sum_{i=0}^{\infty} a_i \underbrace{\frac{2\omega_r\left(1 - \cos\left(2\tau\omega_i\right)\right)}{A_r\tau\left(\omega_i^2 - \omega_r^2\right)}}_{A_{\Im,i}} - b_i \underbrace{\frac{2\omega_r \sin\left(2\tau\omega_i\right)}{A_r\tau\left(\omega_i^2 - \omega_r^2\right)}}_{B_{\Im,i}}. \qquad (2.17b)$$

The deviation from the true transfer function is undefined for $\omega_i = \omega_r$, but the limit for ω_i approaching ω_r exists and the real and imaginary part of this limit are given by,

$$\lim_{\omega_i \to \omega_r} \Re\left[\tilde{H} - \mu_H\right] = a_i \frac{2}{A_r}, \qquad \lim_{\omega_i \to \omega_r} \Im\left[\tilde{H} - \mu_H\right] = -b_i \frac{2}{A_r}. \qquad (2.18)$$

In equation (2.17), the deterministic part of the random terms are grouped in constants, denoted by the under-brackets. Using the grouping, the second order statistical moment, the variance, and the fourth order statistical moment for the real and imaginary part are given by,

$$\mu_{\Re,\Im,2} = \left[\sum_{i=1}^{\infty} \sigma_i^2\left(A_{\Re,\Im,i}^2 + B_{\Re,\Im,i}^2\right)\right], \qquad (2.19)$$

$$\mu_{\Re,\Im,4} = 3\left[\sum_{i=1}^{\infty} \sigma_i^2\left(A_{\Re,\Im,i}^2 + B_{\Re,\Im,i}^2\right)\right]^2. \qquad (2.20)$$

Herein σ_i given in equation (2.10) and determined by the auto spectral density of the noise. The odd moments are equal to zero and for this model, the kurtosis is not dependent on any statistical parameter and is equal to three, resembling that of a normal distribution.

Random Phase

For the random phase model, the real and imaginary part of the deviation from the expected values are given by,

$$\Re\left[\tilde{H} - \mu_H\right] = \sum_{i=0}^{\infty} C_i \underbrace{\frac{2\omega_i \sin\left(\tau\omega_i\right)}{A_r \tau \left(\omega_i^2 - \omega_r^2\right)}}_{A_{\Re,i}} \cos\left(\theta_i + \tau\omega_i\right), \qquad (2.21a)$$

$$\Im\left[\tilde{H} - \mu_H\right] = \sum_{i=0}^{\infty} C_i \underbrace{\frac{2\omega_r \sin\left(\tau\omega_i\right)}{A_r \tau \left(\omega_i^2 - \omega_r^2\right)}}_{A_{\Im,i}} \sin\left(\theta_i + \tau\omega_i\right). \qquad (2.21b)$$

The real and imaginary part of the deviations are undefined for $\omega_i = \omega_r$, but the limits $\omega_i \to \omega_r$ exist for both the terms and are given by,

$$\lim_{\omega_i \to \omega_r} \Re\left[\tilde{H} - \mu_H\right] = C_i \frac{2}{A_r} \cos\theta_i, \qquad \lim_{\omega_i \to \omega_r} \Im\left[\tilde{H} - \mu_H\right] = C_i \frac{2}{A_r} \sin\theta_i. \qquad (2.22)$$

Using the grouping of the terms as in equation (2.21), the variance and fourth order statistical moment of the real and imaginary parts are given by

$$\mu_{\Re,\Im,2} = \frac{1}{2} \sum_{i=1}^{\infty} A_{\Re,\Im,i}^2, \qquad (2.23)$$

$$\mu_{\Re,\Im,4} = \frac{3}{8} \left[2\left(\sum_{i=1}^{\infty} A_{\Re,\Im,i}^2\right)^2 - \sum_{i=1}^{\infty} A_{\Re,\Im,i}^4 \right]. \qquad (2.24)$$

It follows that the kurtosis, as given by equation (2.16), for this model has a theoretical maximum value of 3. If there is only one term present in equation (2.11), the kurtosis reduces to 1.5, agreeing to the kurtosis of the arcsine distribution.

Random phase and amplitude

For the random phase and amplitude model, the expression for the real and imaginary part of the deviation are similar to those of the random phase model, except that the determin-

istic part of the terms now exclude the amplitude,

$$\Re\left[\tilde{H} - \mu_H\right] = \sum_{i=0}^{\infty} c_i \underbrace{\frac{2\omega_i \sin\left(\tau\omega_i\right)}{A_r\tau\left(\omega_i^2 - \omega_r^2\right)}}_{A_{\Re,i}} \cos\left(\theta_i + \tau\omega_i\right), \qquad (2.25a)$$

$$\Im\left[\tilde{H} - \mu_H\right] = \sum_{i=0}^{\infty} c_i \underbrace{\frac{2\omega_r \sin\left(\tau\omega_i\right)}{A_r\tau\left(\omega_i^2 - \omega_r^2\right)}}_{A_{\Im,i}} \sin\left(\theta_i + \tau\omega_i\right), \qquad (2.25b)$$

and the limits for $\omega_i \to \omega_r$ are given by,

$$\lim_{\omega_i \to \omega_r} \Re\left[\tilde{H} - \mu_H\right] = c_i \frac{2}{A_r} \cos\theta_i, \quad \lim_{\omega_i \to \omega_r} \Im\left[\tilde{H} - \mu_H\right] = c_i \frac{2}{A_r} \sin\theta_i. \qquad (2.26)$$

The second order and fourth order statistical moments of the real and imaginary part of the deviation are given by,

$$\mu_{\Re,\Im,2} = \frac{1}{2} \sum_{i=1}^{\infty} c_i^2 \alpha_i^2 (1 + \alpha_i)\beta_i^2, \qquad (2.27)$$

$$\mu_{\Re,\Im,4} = \frac{3}{4}\left(\left[\sum_{i=1}^{\infty} a_i^2 \alpha_i^2 (1 + \alpha_i)\beta_i^2\right]^2 - \frac{1}{2}\sum_{i=1}^{\infty} a_i^4 \alpha_i (1 + \alpha_i)(-6 - 3\alpha_i + \alpha_i^4)\beta_i^4\right). \qquad (2.28)$$

2.4 Results and discussion

In the previous section, equations were derived to express the variance and kurtosis of a measured transfer function as function of the single sided auto spectral density of the background spectrum. In this section, the resulting expressions are validated against experiments.

In the experiments, the transfer function between the signal exciting a loudspeaker and a microphone measuring the emitted sound field from the loudspeaker is measured. Two other loudspeakers are used to provide an acoustic background signal $n(t)$, measured by the microphone. The first loudspeaker creating the background signal emits white noise, generated by a Brüel and Kjætype 1405 noise generator, and the second loudspeaker emits a pure sine wave at 1180Hz. The transfer function is measured at 1280 Hz, and the sampling frequency was 12800 Hz, such that a full period is sampled with 10 samples.

The transfer function has been measured for a duration of three seconds and the measurement has been repeated for 2000 times. Between each measurement a random amount of time has been passed before measuring the transfer function. In this way, the starting
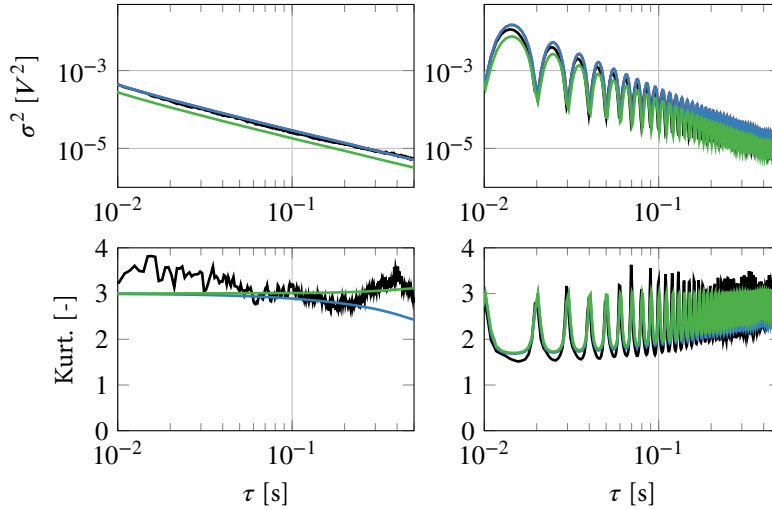
Figure 2.3: *The variance and kurtosis of the real part of the transfer function from the measurement and models as function of integration time for two different background signals. Top row shows the variance and the bottom row the kurtosis. Left column, only white noise present as the background signal. Right column, white noise and a single harmonic signal present as background signal. Kurtosis and variance as function of integration time. The measurement is denoted by(——), the random Fourier coefficient model by (——), the random phase model by (——) and the random amplitude and phase model by (——).*

phase of the measurement excitation relative to that of the background sine wave is non-deterministic. The background signal was measured for 60 seconds without the presence of the excitation at a sample frequency of 12800 Hz. The corresponding background spectrum was determined by using 150 averages with a rectangular window function.

In figure 2.3, the measured variance and kurtosis of the real part of the transfer function are shown as function of the integration time τ for two different measurements. For clarity, the results for the imaginary part have been omitted as they behave similarly. The background signal consisted only of white noise for the first measurement. For the second measurement, the background signal consisted of both the white noise and the sine signal.

When only white noise is present, the variance decays monotonically with the integration time. The decay is exponential and proportional to the inverse of the integration time, $\sigma^2 \propto \tau^{-1}$, agreeing to the theoretical results [8]. The kurtosis for the first measurement case is around three, corresponding to that of a normal distribution in accordance with theoretical results and assumptions.

The match between the measured and estimated statistical parameters is not perfect.
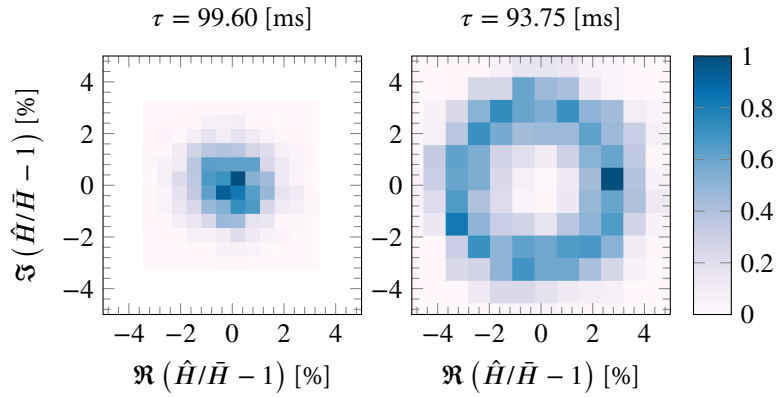
Figure 2.4: *Normalized histogram of the real and imaginary part of the relative deviation from the mean value of the measured transfer functions for two different integration times. The background signal consists of white noise and a sine signal.*

Therefore, the variance has been also determined for different sets of measurement samples and it shows that the variance does not converge, but shows a slight drift as function of time. This indicates that the properties of $n(t)$ and H are not completely time invariant and the measurement conditions are violating the imposed assumptions.

For the second measurement case, shown in the right column of figure 2.3, the variance has distinct minima and maxima and the envelope of these extrema decays exponentially with increasing integration time, that is $\sigma^2 \propto \tau^{-1}$. Due to synchronous demodulation, the harmonic background signal will introduce a slow oscillating component, which oscillates at the difference of the excitation frequency and the background signal, which is in this case 100 Hz. When the integration time is exactly a multiple of the period, the slowly varying component will not contribute to the measured transfer function in (2.5), leading to the minima occurring at integration times which are a multiple of 10 milliseconds.

The measured kurtosis shows that at the positions where the contribution of the harmonic background signal is zero, the kurtosis is around three. For the other integration time, the kurtosis is lower than 3. For these integration times, the background tone contributes to the variance. When this contribution is the largest, the kurtosis is similar to that of the arcsine distribution, which has a theoretical kurtosis of 1.5. The model results are also plotted in figure 2.3. For the variance, all three models agree reasonably well with the measurement results. The model with the random amplitude and phase under predicts the variance for both the measurement cases. The Fourier coefficient model and the random phase predict the same variance and agree well when there is only white noise present. When

the sine signal is present in the background signal, the variance is slightly over predicted by these models.

For the kurtosis only the random phase model and the random amplitude with random phase model are shown as the Fourier coefficient model does not predict the kurtosis. When the sine signal is not present in the background signal, the models predict a kurtosis close to three and this compares reasonably well with the measurements.

When the sine signal is present in the background signal, the kurtosis varies between 1.5 and 3 as function of the integration time. The predictions by the random phase model and the random amplitude and phase model are very similar and follow the trend of the measurements. For the measurements, the measured kurtosis is larger than three for certain integration times, but as shown the random phase model cannot be larger than three. For the random amplitude and phase model, the kurtosis can be larger than three, but in general both models underestimate the depth of the troughs and the height of the peaks.

Comparing the random phase model and the random amplitude and random phase model, they both predict similar values for the kurtosis and variance. However, the latter model needs more information, that is the variance of the auto spectral density. Therefore, the random phase model is the stronger candidate to model the variance and kurtosis of the transfer function, as the expressions to calculate statistical parameters are simpler and the model needs less information compared to the random phase and amplitude model.

The difference in the kurtosis as function of the integration time when the sine signal is present in the background signal can be appreciated by looking at the histograms of the measured transfer functions. In figure 2.4 the histograms of the real and imaginary parts of the transfer function relative to the mean value of the transfer function are shown for two different integration times. For the first integration time, $\tau = 99.60$ms, the integration time is a multiple of the period of the slowly-varying component and its contribution to the estimate of the transfer function is not present. The histogram shows that the transfer function estimates are approximately circularly distributed indicating that the measured transfer function can be modelled as a bivariate normal distribution, where there is no correlation between the real and imaginary parts.

For the second integration time $\tau = 93.75$ms the presence of the harmonic background signal modulates the measured transfer function. The resulting histogram has the form of torus and the probability density function of the real and imaginary parts resemble that of an arcsine distribution. In such a situation, the assumption of the normally distributed probability density function of the transfer function is not appropriate.

From the measurements, it can be shown that the variance of the real and imaginary parts are not equal. The difference can be estimated by interpreting the variance as a weighted sum of the noise spectrum. As an example, evaluating and rewriting equation (2.23) using
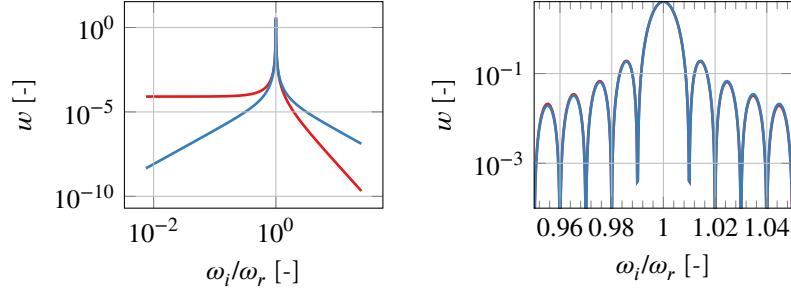
Figure 2.5: *The weighting function of the real part of the variance $w_{\Re,i}$, (——), and imaginary part $w_{\Im,i}$, (——), as function of frequency relative to the excitation frequency, ω_i/ω_r. The left column shows the envelope of the function, evaluated at the positions $\cos(2\tau\omega_i) = 1$, the right column shows a close up of the function in the neighbourhood of $\omega_i/\omega_r = 1$. The integration time, τ, is 50ms and the excitation frequency 1000Hz.*

weights for the real and imaginary parts, $w_{\Re,i}$, $w_{\Im,i}$, the following expression can be obtained,

$$\sigma_{\Re}^2 = \frac{1}{2}\sum_{i=1}^{\infty} A_i^2 w_{\Re,i}, \quad w_{\Re,i} = \frac{8\omega_i^2(1 - \cos\left(2\tau\omega_i\right)}{A_r^2\tau^2\left(\omega_i^2 - \omega_r^2\right)^2}, \tag{2.29a}$$

$$\sigma_{\Im}^2 = \frac{1}{2}\sum_{i=1}^{\infty} A_i^2 w_{\Im,i}, \quad w_{\Im,i} = \frac{8\omega_r^2(1 - \cos\left(2\tau\omega_i\right)}{A_r^2\tau^2\left(\omega_i^2 - \omega_r^2\right)^2}. \tag{2.29b}$$

From the above expressions, (2.29), it follows that the weights $w_{\Re,i}$ and $w_{\Im,i}$ are not equal and thus the assumption of a circular distributed error on the transfer function, implying equal variances for the real and imaginary part is in general not true. It can be shown that in the special case of a constant auto spectral density for $f \in [0, \infty)$, the variances of the real and imaginary part are equal. In figure 2.5 the weighting function is shown, as function of the angular frequency ω_i, normalized with the angular excitation frequency ω_r. In the left column, the function is plotted only for the points where $\cos\left(2\tau\omega_i\right)$ is zero to show the envelope of the function. In the limit of $\omega_i \to 0$, the weights for the variance of the real part are not a function of ω_i, whereas for the imaginary part, the weights are proportional to ω_i^{-4}. Therefore, if the background spectrum contains a single frequency component with a large amplitude at frequency below the excitation frequency, the variance of the real part will be larger than the variance of the imaginary part. The weighing functions both decay for frequencies larger than the excitation frequency but at a different slope. The real part of the variance is proportional ω_i^{-4} whereas the imaginary part of the variance is proportional to ω_i^{-2}, and thus if the noise spectrum a single frequency component with a larger amplitude

at a frequency higher than the excitation frequency, the variance of the imaginary part will be larger than that of the real part. For the experiments where the sine signal is present, the variance of the imaginary part is around 10 % smaller compared to the real part when the sine signal contributes to the variance and the integration time is in the order of 100ms.

In the right column of figure 2.5, a close up of the region $\omega_i/\omega_r \approx 1$ of the weighing functions is shown. The weighing functions show lobes and the zero points correspond to the frequencies where $\cos\left(2\tau\omega_i\right)$ is equal to zero. At these zeros, the unwanted signal does not contribute to the observed variance, which is the same phenomena as seen before where the sine part of the background signal did not contribute to the observed variance. The width of the lobes is proportional to the integration time, and the height of the lobes decreases with τ^2, except for the main lobe. For the main lobe, the height is given by the square of the limit expression given in equation (2.22) and is not a function of the integration time. With increasing integration time, this difference decreases as the weights decrease with increasing integration time, except at the integration time.

2.5 Conclusion

This chapter shows that the variance and kurtosis of transfer functions can be determined with the information of the noise signal.

With the synchronous demodulation technique, the deviation from the transfer function as function of the noise is derived in the time domain. Three models are used to model the noise in the frequency domain.

In the first model, the noise is modelled as a Fourier series, where both the Fourier coefficients are modelled as stochastic variables with a normal probability density function. The second model consisted of a Fourier series, for which the amplitude is a deterministic variable and the phase a random variable with a uniform distribution. In the third model, the amplitude and the phase are considered to be random, where the amplitude is modelled as a gamma distribution and the phase as a uniform distributed variable.

From the expressions of the deviation of the transfer functions in the time domain and the noise model, the variance and kurtosis are derived. The derived relations are validated against experiments, where the transfer function between a microphone and loudspeaker is measured. The background signal is provided by two loudspeakers, one emitting white noise and the other one a single tone.

A good correspondence between the predicted variance and the measured variance is shown for all the models. The kurtosis is only predicted by the random amplitude and random phase model and the random phase model. Both models show a good correspondence with the measured kurtosis. The random phase model is preferred as the model parameters

can be inferred from the auto spectral density, whereas for the random amplitude and the random phase model the variance on the auto spectral density has to be known to be able to determine the needed parameters.

Furthermore, using the derived expressions, the assumption that the real and imaginary parts are uncorrelated and have the same variance have been investigated. It is shown that the variance on the real and imaginary parts depend on the noise spectrum and the measurement time for a single sample.

CHAPTER 3 ■

Acoustic Theory

In this chapter, the basic acoustic theory will be repeated. The discussion starts by introducing the governing equations for motion of an isotropic viscous fluid. Thereafter, the existence of the acoustic boundary layer is shown by deriving the three coupled wave equations that govern small perturbations in a motionless fluid. The last part introduces the concept of acoustic modes and the scattering matrix is introduced. It concludes with the wave decomposition method.

3.1 Governing equations

In the following a short summary of the set of equations that model the motion of a viscous fluid are given. The interested reader is referred for a more in-depth discussion of the equations to [13–15]. The motion of a continuous medium can be described by the conservation of mass, momentum and energy in a fixed control volume. The mass conservation equation, also called the *continuity equation*, is given by

$$\frac{\partial \rho}{\partial t} + \operatorname{div} \rho \boldsymbol{v} = 0, \tag{3.1}$$

where t is the time, ρ is the density of the medium and $\boldsymbol{v}$ the velocity. The divergence operator is denoted by div. For a viscous isotropic fluid the conservation of momentum is given by the *Navier-Stokes equation*, relating the change of momentum of infinitesimal fluid element to the forces acting on that element.

The momentum equation is given by

$$\rho \frac{D\boldsymbol{v}}{Dt} = -\operatorname{grad} p + \operatorname{div} \boldsymbol{\tau} + \boldsymbol{g}, \tag{3.2}$$

where p is the pressure, τ the fluid stress tensor and g the body forces per unit volume acting on the fluid element. The gradient operator is denoted by grad and the material derivative given by,

$$\frac{D\square}{Dt} = \frac{\partial \square}{\partial t} + \boldsymbol{v} \cdot \text{grad}\,\square. \tag{3.3}$$

When the fluid is considered Newtonian, that is the stress tensor is linearly related to the rate of deformation of the fluid element and the fluid is considered isotropic, the fluid tensor τ is given by,

$$\tau = \mu \left[\text{grad}\,\boldsymbol{v} + \left(\text{grad}\,\boldsymbol{v} \right)^T - \frac{2}{3} \text{div}\,\boldsymbol{v}\boldsymbol{I} \right] + \zeta \,\text{div}\,\boldsymbol{v}\boldsymbol{I}. \tag{3.4}$$

Herein is μ the viscosity of the fluid, $\boldsymbol{I}$ the identity matrix and ζ the bulk viscosity of the fluid.

The third equation is given by the energy equation, relating the rate of change of energy of the element caused by the forces acting upon the element and the heat conduction to the element,

$$\rho \frac{D}{Dt} \left(e + v^2 \right) = -\,\text{div}\, p\boldsymbol{v} - \,\text{div}\,\boldsymbol{q} + \,\text{div}\,(\tau \cdot \boldsymbol{v}) + \boldsymbol{g}\boldsymbol{v}, \tag{3.5}$$

where e is the internal energy of the fluid, $v = |\boldsymbol{v}|$ the absolute value of the velocity vector and $\boldsymbol{q}$ the heat flux vector. The internal energy for an ideal and calorific perfect gas is proportional to the temperature T of the gas, $e = c_v T$, where c_v is the heat capacity at constant volume.

The heat flux $\boldsymbol{q}$ is modelled by *Fourier's law*, which states that the heat flux is proportional to the temperature gradient,

$$\boldsymbol{q} = -\kappa \,\text{grad}\, T. \tag{3.6}$$

The last equation that is needed is the equation of state. The equation of state of the gas is modelled using the *ideal gas law*,

$$p = \rho R T, \tag{3.7}$$

where R is the specific gas constant.

This set of five equations, (3.1), (3.2), (3.5), (3.6) and (3.7) describes the fluid motion of an isotropic viscous fluid and is also known as the *Navier-Stokes-Fourier model of a compressible fluid*

3.2 Wave equations in a stationary viscous medium

The pressure fluctuations of acoustic disturbances are in generally small compared to the mean pressure, and the equations governing the acoustic perturbations can be found by linearising the Navier-Stokes equations.

Assuming that the fluid is motionless, that it the steady mean value of the velocity is zero, $\bar{u} = 0$, the governing equations can be rewritten into three variables, all governed by a wave equation. These three fields are also often called the acoustic mode, the vorticity mode and the entropy mode [13]. In this section, the existence of the three fields will be shown and discussed using the (translated) derivation and discussion given by Fritsche [16], based on a theory by Thiesen [17].

The linearised equation of conservation of mass is given by,

$$\frac{\partial \rho}{\partial t} + \rho_0 \operatorname{div} \boldsymbol{v} = 0, \tag{3.8}$$

where $\boldsymbol{v}$ is the vector of the acoustic particle velocity, assumed to be infinitely small. The linearised equation of conservation of momentum equals to,

$$\rho_0 \frac{\partial \boldsymbol{v}}{\partial t} + \operatorname{grad} p = \mu_1 \Delta \boldsymbol{v} + \mu_1 \operatorname{grad} \operatorname{div} \boldsymbol{v}. \tag{3.9}$$

Herein, denotes $\mu_1 = \mu$ the viscosity and $\mu_2 = \frac{1}{3}\mu + \zeta$ denotes the linear combination of viscosity and the bulk viscosity. The Laplace operator is denoted by $\Delta = \operatorname{div} \operatorname{grad}$.

The linearised energy conservation equation, neglecting the energy generated by viscosity, is given by,

$$-p \operatorname{div} \boldsymbol{v} = \rho_0 c_v \frac{\partial T}{\partial t} + \operatorname{div} \boldsymbol{q}. \tag{3.10}$$

Decomposing the Navier-Stokes equation

Using the Helmholtz-decomposition, the acoustic velocity can be decomposed in an irrotational part and a divergence free part,

$$\boldsymbol{v} = \operatorname{grad} \phi + \operatorname{rot} \boldsymbol{a}. \tag{3.11}$$

It follows, by taking the divergence of the above equation, (3.11), that

$$\Delta \phi = \operatorname{div} \boldsymbol{v}, \tag{3.12}$$

where $\Delta = \operatorname{div} \operatorname{grad}$ is the Laplace operator. Introducing the Helmholtz-decomposition of the velocity in the momentum equation, it can be written as the gradient of a rotational free part and the rotation of a divergence free part,

$$\operatorname{grad} \Phi + \operatorname{rot} \boldsymbol{A} = 0, \tag{3.13}$$

where the rotational free and divergence free parts are given by,

$$\Phi = \frac{\partial \phi}{\partial t} - (v_1 + v_2)\Delta \phi + \frac{p}{\rho_0}, \tag{3.14a}$$

$$\boldsymbol{A} = \frac{\partial \boldsymbol{a}}{\partial t} - v_1 \Delta \boldsymbol{a}. \tag{3.14b}$$

Herein is $v_{1,2} = \mu_{1,2}/\rho$. Taking the divergence of $\boldsymbol{A}$, it follows that it has to be zero because $\boldsymbol{a}$ is divergence free.

Rewriting the energy equation

The energy equation is rewritten by introducing the variable,

$$\Theta = \frac{1}{\gamma - 1} \frac{T - T_0}{T_0}, \qquad T = (\gamma - 1)T_0\Theta + T_0, \tag{3.15}$$

where $\gamma = c_p/c_v$. Introducing this in the energy equation (3.10), leads to:

$$- p\Delta\boldsymbol{v} = \rho_0 c_v(\gamma - 1)T_0 \frac{\partial\Theta}{\partial t} - \lambda(\gamma - 1)T_0 \operatorname{grad}\Theta, \tag{3.16}$$

then rewriting $p = \rho(c_p - c_v)T = \rho c_p(\gamma - 1)T$ leads to,

$$\Delta\phi + \frac{\partial\Theta}{\partial t} - v_3\Delta\Theta = 0, \tag{3.17}$$

herein is $v_3 = \lambda/\rho_0 c_v$. The difference $p \operatorname{div} \boldsymbol{v} - p_0 \operatorname{div} \boldsymbol{v}$ has been neglected because of the assumption of infinitesimal acoustic disturbances.

Rewriting the constitutive equation

The constitutive equation in linear form is given by,

$$\frac{p - p_0}{p_0} = \frac{\rho - \rho_0}{\rho_0} + \frac{T - T_0}{T_0}. \tag{3.18}$$

Differentiating this with respect to time and replacing $\frac{\partial\rho}{\partial t}$ with the help of the mass equation yields the expression:

$$\frac{\partial}{\partial t} \frac{p}{\rho_0} = \frac{c^2}{\gamma}(\gamma - 1)\frac{\partial\Theta}{\partial t} - \frac{c^2}{\gamma}\Delta\phi, \quad \text{with } c^2 = \frac{p_0\gamma}{\rho_0}. \tag{3.19}$$

The new system of equations

By differentiating the irrotational part of the Navier-Stokes equation, (Φ), with respect to time and eliminating $\frac{\partial}{\partial t} \frac{p}{\rho_0}$ using equation (3.19), three coupled wave equations are obtained from the three conservation equations, Fourier's law and the constitutive equations.

Assuming a time dependence of $\exp[i\omega t]$ for the field variables,

$$(\Phi, \phi, \Theta) = (\Phi^*, \phi^*, \Theta^*)e^{i\omega t}, \tag{3.20}$$

the three coupled wave equations are given by (the superscript * will be omitted from here onwards),

$$0 = \Delta\Phi, \tag{3.21a}$$

$$0 = \Delta\phi + i\omega\Theta - \frac{\lambda}{\rho_0 c_v}\Delta\Theta, \tag{3.21b}$$

$$0 = i\omega\Phi + \omega^2\phi + \left[i\omega(\nu_1 + \nu_2) + \frac{c^2}{\gamma}\right]\Delta\phi - i\omega\frac{c^2}{\gamma}(\gamma - 1)\Theta. \tag{3.21c}$$

The set of equations can be solved by eliminating Φ and ϕ, to obtain a fourth order differential equation in Θ, which is the approach used by Kirchhoff.

Thiesen [17] takes another approach to solve the system. The scalar functions Φ, ϕ, Θ describe the movement and thermo-dynamic state of each elemental volume of gas. The phase between each of these states, which gives a measure of the reversibility of the state changes, should be constant throughout space if the gas is homogeneous.

This is only possible if surfaces of constant Φ and the corresponding ϕ and Θ for these surfaces congruent are with each other and that they move at the same speed. If the sound field is composed of n parts, which are independent of each other and expand with different speeds, then Φ, ϕ and Θ should also be composed of n independent parts. With this reasoning, Thiesen makes the following ansatz,

$$\phi = \sum_{l=0}^{n-1} H_l, \quad \Theta = \sum_{l=0}^{n-1} a_l H_l, \quad \Phi = \sum_{l=0}^{n-1} b_l H_l, \tag{3.22}$$

where a_l and b_l are complex constants. The solution for each part, H_l, is given by

$$\Delta H_l + k_l^2 H_l = 0. \tag{3.23}$$

This means that each wave equation, with a certain wave number k_l^2 should have a unique solution. With the above ansatz in the three coupled equations gives rise to the following relations,

$$0 = k_l^2 b_l, \tag{3.24a}$$

$$0 = -\nu_3 k_l^2 a_l - i\omega a_l + k_l^2, \tag{3.24b}$$

$$0 = \omega^2 - k_l^2\left[\frac{c^2}{\gamma} + i\omega(\nu_1 + \nu_2)\right] - \frac{c^2}{\gamma}(\gamma - 1)i\omega a_l + i\omega b_l. \tag{3.24c}$$

The first two solutions can be obtained by considering all solutions where $k_l \neq 0$. It follows from the first equation that $b_l = 0$ and from the other two equations, a dispersion relation can be obtained,

$$k_l^4\left(\frac{1}{\gamma k^2} + \frac{1}{k_v^2}\right)\frac{1}{k_w^2} - k_l^2\left(\frac{1}{k^2} + \frac{1}{k_v^2} + \frac{1}{k_w^2}\right) + 1 = 0, \tag{3.25}$$

where

$$k^2 = \frac{\omega^2}{c^2}, \quad k_w^2 = \frac{\omega^2}{c_w^2} \text{ with } c_w^2 = i\omega\nu_3 \quad \text{and} \quad k_v^2 = \frac{\omega_2}{i\omega(\nu_1 + \nu_2)}.$$

The both solutions for the dispersion relation (3.25), k_1^2 and k_2^2, are corresponding to the waves H_1 and H_2. The constant a_l for these two solution is found by the energy equation in the set of (3.24)

$$a_l = \frac{1}{-i\omega} \frac{k_l^2 k_w^2}{k_l^2 - k_w^2}, \quad l = 1, 2. \tag{3.26}$$

The third solution is obtained for the case where $k_l = 0$, corresponding to the H_0 wave. Introducing $k_l = 0$ into the equations (3.24), it follows that $b_0 = i\omega$. As there are no more unique solutions for k_l, the solution is given by,

$$\phi = H_0 + H_1 + H_2, \tag{3.27a}$$

$$\Theta = a_1 H_1 + a_2 H_2, \tag{3.27b}$$

$$\Phi = i\omega H_0. \tag{3.27c}$$

Representation of the acoustic velocity

The acoustic velocity field is represented as the superposition of a rotational and divergence free field (3.11),

$$\boldsymbol{v} = \text{grad}\,\phi + \text{rot}\,\boldsymbol{a}.$$

To obtain the still unknown $\boldsymbol{a}$ we use the notion that the Navier-Stokes equation is split up into a irrotational and solenoidal field. It then follows from equation (3.13) that $\text{div}\,\boldsymbol{A} = 0$ and that $-\text{rot}\,\boldsymbol{A} = \text{grad}\,\Phi$. Furthermore,

$$\Delta\boldsymbol{A} = \text{grad}\,\text{div}\,\boldsymbol{A} - \text{rot}\,\text{rot}\,\boldsymbol{A} = \text{rot}\,\text{grad}\,\Phi = 0. \tag{3.28}$$

Using the equation for the divergence free part, (3.14b) and introducing the ansatz of an harmonic time dependence of the field variables, it can be rewritten as

$$-\frac{\boldsymbol{A}}{\nu_1} = \Delta\boldsymbol{a} + k_3^2\boldsymbol{a}, \quad \text{with } k_3^2 = \frac{\omega^2}{i\omega\nu_1}. \tag{3.29}$$

A solution to this equation is given by $\boldsymbol{a} = \frac{\boldsymbol{A}}{i\omega}$, resulting in $\text{grad}\,\text{div}\,\boldsymbol{A}/i\omega = 0$. The solution is a particular solution of the inhomogeneous differential equation, and the homogeneous equation is given by,

$$\Delta\boldsymbol{a} + k_3^2\boldsymbol{a} = 0, \tag{3.30}$$

a wave equation, for which the solution is of the type H_l and given by $\boldsymbol{H}_3$. The complete solution to the differential equation is given by

$$a = \frac{A}{i\omega} + \boldsymbol{H}_3. \tag{3.31}$$

wherein,

$$\boldsymbol{H}_3 = H_3^{(1)}\boldsymbol{i} + H_3^{(2)}\boldsymbol{j} + H_3^{(3)}\boldsymbol{k}. \tag{3.32}$$

It shows that each of the components of $\boldsymbol{H}_3$ are separate solutions to the vector wave equation for k_3. As the solution $\boldsymbol{H}_3$ only consist of the divergence free parts, it represents the incompressible part of the solution. The velocity can then be written as

$$\boldsymbol{v} = \operatorname{grad}\left[H_1 + H_2\right] + \operatorname{rot}\left[\boldsymbol{H}_3\right]. \tag{3.33}$$

which together with equation (3.27b),

$$\Theta = a_1 H_1 + a_2 H_2,$$

and the wave equations (3.23)

$$\Delta H_l + k_l^2 H_l = 0, \quad l = 1, 2, 3.$$

represent the system of equations from which we started.

The wave numbers k_l^2

The two solutions for the dispersion relation (3.25), first order in respect to ω, are given by

$$\begin{aligned}
k_1^2 &= k^2 \left\{ 1 - i\frac{\omega}{c^2} \left[\nu_1 + \nu_2 + \left(1 - \frac{1}{\gamma}\nu_3\right)\right]\right\}, \\
k_2^2 &= \gamma k_w^2 \left\{ 1 + i\frac{\omega}{c^2}\gamma \left[\nu_1 + \nu_2 - \frac{1}{\gamma}\nu_3\right]\right\}.
\end{aligned} \tag{3.34}$$

For gases, the three terms in the square brackets are of similar magnitudes, because $\nu_3/\gamma = \nu_1(\lambda/\eta c_p) = \nu_1 \operatorname{Pr}$, where Pr the Prandtl number. For gases, the $\operatorname{Pr} = \mathcal{O}(1)$.

The size of the complete term in the square bracket can be approximated by $\omega/c^3\nu_3$. Introducing the wave length of the acoustic wave $\Lambda_{ac} = 1/k$ and the wave length of the isochoric heat conduction wave $\Lambda_h = 1/k_w$, the term is given by

$$\frac{\omega}{c^2}\nu_3 = \frac{1}{2}\left(\frac{\omega}{c}\right)^2\frac{2\nu_3}{\omega} = \frac{1}{2}\left(\frac{\Lambda_w}{\Lambda_{ac}}\right)^2. \tag{3.35}$$

At ambient pressure and a frequency of a 1000 Hz, the Λ_w is in the order of 10^{-2} cm, Λ_{ac} is at the same frequency in the order of 10 cm and thus $\left(\Lambda_w/\Lambda_{ac}\right)^2 << 1$. Under these conditions, one can approximate the equations (3.34) with,

$$k_1^2 \approx k^2, \quad \text{and } k_2^2 = \gamma k_w^2, \tag{3.36}$$

Furthermore, it follows that

$$|k_3^2|| \approx |k_2^2| >> |k_1^2|, \tag{3.37}$$

and the constants for the are we obtain

$$a_1 \approx \frac{-i}{\omega}k_1^2, \quad a_2 \approx \frac{i}{\omega}k_2^2\frac{1}{\gamma-1}, \tag{3.38}$$

and

$$\frac{a_1}{a_2} \approx -(\gamma-1)\frac{k_1^2}{k_2^2} \quad \text{and } |(\frac{a_1}{a_2}|) << 1. \tag{3.39}$$

Physical interpretations of the functions H_1, H_2 and H_3

When heat conduction and viscosity can be neglected, the wave number for H_1 reduces to,

$$k_1^2 = k^2, \tag{3.40}$$

and because $v_1 = v_2 = v_3 = 0$ it shows that $|k_2^2| = |k_2^2| = \infty$. This means that the waves H_2 and H_3 do not contribute to the sound propagation because of the vanishing small propagation speed of these waves. In this case, the system of equations reduces to

$$\boldsymbol{v} = \text{grad } H_1, \quad \Theta = \frac{-i\omega}{c^2}H_1, \quad \Delta H_1 + \frac{\omega^2}{c^2}H_1 = 0, \tag{3.41}$$

and H_1 represents the velocity potential of the adiabatic sound wave.

With finite viscosity and heat conduction, the propagation constant of the acoustic wave is slightly changed and secondary waves H_2 and H_3 arise. The H_2 is a wave where only the temperature diffusivity governs the wave speed and it is a pure heat conduction wave. Consider a plane heat conduction wave,

$$H_2 \propto e^{ik_2 x}. \tag{3.42}$$

The propagation constant is given by

$$k_2^2 = \frac{-i\omega\gamma}{v_3}, \quad k_2 = \frac{1-i}{\sqrt{2}}|k_2|, \tag{3.43}$$

showing that the heat conduction wave is highly damped. A measure of how far the heat conduction wave reaches is the thermal boundary layer thickness,

$$\Delta_h = \frac{2}{\omega} \sqrt{\frac{\omega \nu_1}{2}} \sqrt{\text{Pr}}. \tag{3.44}$$

For oscillating field at a 1 kHz at normal pressure in air, the thickness of the thermal boundary layer is around 60μm In an analogous way, the H_3 represent a viscosity wave where the propagation constant is solely determined by the viscosity. A measure for the propagation distance of this wave is given by the acoustic viscous boundary layer thickness,

$$\Delta_v = \frac{2}{\omega} \sqrt{\frac{\omega \nu_1}{2}}. \tag{3.45}$$

The proportionality constant between the boundary layer thickness is given by the Prandtl number and thus for gasses the thicknesses are of the same order of magnitude. The presence of the heat conduction and viscous waves are confined to the boundaries and discontinuities of the system because they decay rapidly in free space.

Connection between p and the waves H_1, H_2 and H_3

With the ansatz that the total pressure consists of superposition of the ambient pressure and the pressure disturbance of the acoustic wave, $p = p_0 + \tilde{p}$, it follows from equation(3.19) and equation (3.24c)

$$\tilde{p} = \frac{\rho_0 c^2}{\gamma k_w^2} \left(\Delta \Theta + \gamma k_w^2 \Theta \right), \tag{3.46}$$

and the pressure is a function of the acoustic and temperature wave.

However, when the condition $\left(\Lambda_w / \Lambda_{ac} \right)^2 \ll 1$ is fulfilled, then $\gamma k_w^2 = k_2^2$ holds. The equation (3.46) can then be rewritten, using $\Theta = a_1 H_1 + a_2 H_2$ and it follows that,

$$\tilde{p} = \rho_0 \frac{\omega^2}{k^2 \gamma k_w^2} \left[a_1 (\Delta H_1 + k_2^2 H_1 + a_2 \left(\Delta H_2 + k_2^2 H_2 \right) \right],$$
$$\text{with} \quad \Delta H_2 + k_2^2 H_2 = 0. \tag{3.47}$$

Therefore, when an acoustic wave hits a surface, it will be scattered and also excite the secondary waves. However when the wavelength of these secondary waves is much smaller then the acoustic wave length, they will not contribute to the pressure perturbations and the pressure perturbation at the surface will be solely caused by the acoustic wave.

3.3   Acoustic modes in ducts

In the previous section is it shown that the acoustic sound field in a viscous medium consists of a superposition of three parts, the acoustic mode, the vorticity mode and the entropy mode. In this section, the concept of acoustic modes will be introduced and the mode shapes and wave numbers for rectangular and circular waveguides for specific assumptions are briefly introduced. The interested reader is referred to [18] for more information on the fundamentals of duct acoustics.

Considering a non-viscous fluid and without thermal conductivity, it can be shown that the entropy is conserved and the pressure disturbances are linearly related to density disturbances, that is $p = c_0^2 \rho$. If furthermore an uniform mean flow is assumed, the mass and momentum equation can be linearised, where $\boldsymbol{u}_0 \neq 0$, and the convective wave equation,

$$\frac{D_0 p}{D_0 t} - c_0^2 \Delta p = 0. \tag{3.48}$$

If the acoustic field is assumed to have a time dependence of $\exp[i\omega t]$ and that the boundary conditions on the acoustic field are independent of the axial coordinate x, the ansatz $p \propto \exp[i\omega t - ikx]$ can be made and the convective wave equation reduces to,

$$\Delta p + \left[(\omega - ku_0)^2 - k^2 c_0^2 \right] p = 0. \tag{3.49}$$

where the Laplace operator Δ and the pressure p is no longer dependent on the axial coordinate x.

The solution to equation (3.49) is given,

$$p(x, y, z, \omega) = \sum_{l=0}^{\infty} p_l^+ \psi_l(M, y, z) e^{-ik_l(M,\omega)x} + p_l^- \psi_l(-M, y, z) e^{ik_l(-M,\omega)x}, \tag{3.50}$$

showing that the acoustic field can be represented as an infinite sum of modes. The modal amplitudes of mode l propagating in the positive and negative x-direction are given by p_l^+ and p_l^- respectively. The propagation direction does not have to coincide with the direction of the mean flow. The mean flow is characterized by the Mach-number M, which has no spatial dependency and is defined as the mean flow velocity normalized by the speed of sound, c_0, in the medium. The specific mode shape is given by ψ_l and its corresponding wave number by k_l. The various modes are ordered by their cut-on frequency [19] and the number of modes used to describe the sound field is truncated to the L modes that significantly contribute to the sound field far away from irregularities in the duct. The modes are propagating when the real part of the free-field wave number, given by $k_0 = \omega/c_0$, is larger than the real part of the cut-on wave number of the mode l, $\Re(k_0) > \Re(k_l^c)$. The

wave numbers k_l can be analytically or numerically determined [20–22] and in the next part the wave numbers and mode shapes for rectangular and circular ducts are given under simplifying assumptions.

Rectangular ducts

For waves in circular and rectangular ducts, neglecting losses in the fluid and at the wall and including the effect of uniform mean flow, the axial wave number for mode l is given by,

$$k_l = k_0 \frac{M \pm \sqrt{1 - (1 - M^2)k_l^{c2}/k_0^2}}{1 - M^2}, \tag{3.51}$$

with k_0 the free field wave number, given by ω/c_0 and k_l^c the cut-on wave number for the mode l. For rectangular ducts the cut-on wave numbers are given by,

$$k_l^c = \sqrt{\left(\frac{m_l \pi}{b}\right)^2 + \left(\frac{n_l \pi}{h}\right)^2}, \quad n_l, m_l \in \mathbb{N}, \tag{3.52}$$

where b is the width of the duct and h the height of the duct. The corresponding mode shapes are given by,

$$\psi_l(y, z) = \cos(\frac{m_l \pi}{b} y) \cos(\frac{n_l \pi}{h} z). \tag{3.53}$$

Circular ducts

For waves in circular ducts, the cut-on wave number,s k_l^c, are given by the solutions to the equation,

$$J'_{m_l}(k_l^c R) = 0, \quad m_l \in \mathbb{N}, \tag{3.54}$$

where J'_m is the derivative of the Bessel function of the first kind of order m, and R the radius of the duct. The corresponding mode shapes are given by

$$\psi_l(r, \theta) = \exp(im\theta)J_{m_l}(k_l r), \tag{3.55}$$

where r is the distance from the center of the duct and θ the polar angle in the cross sectional plane of the duct.

Attenuation in ducts

In the first section it was shown that the acoustic sound field in a viscous medium consists of a superposition of three parts, the acoustic mode, the vorticity mode and the entropy mode. When an acoustic wave propagates through a duct, the vorticity and entropy mode will be present close to the duct walls and will lead to a loss of acoustic energy of the acoustic mode.

The influence of the boundaries can be taken into the wave number, when the boundary conditions do not depend on the axial conditions.

When the duct walls are assumed to be rigid, that is the acoustic velocity at the wall is zero $\boldsymbol{u} = 0$, and the wall is isothermal, $T = 0$, the thickness of the acoustic boundary layer is much smaller than the cross sectional dimensions of the waveguide and no mean flow is present, $M = 0$, Kirchhoff derived the correction to the wave number for waves travelling in a circular duct [23]. For waves travelling in rectangular ducts, there are no exact solutions to the wave equation when taking the effect of viscosity and thermal conductivity into account [24].

However, in the first order approximation, the wave number for the plane wave mode is the same for waves propagating in rectangular and circular ducts and is, in first order with respect to ω, given by [13],

$$k = \frac{\omega}{c} + (1+i)\frac{1}{2\sqrt{2}}\sqrt{\frac{\omega\mu}{\rho c^2}}\left[1 + \frac{\gamma-1}{\sqrt{\mathrm{Pr}}}\right]\frac{L_p}{A}, \qquad (3.56)$$

where L_p is the perimeter of the duct cross section and A the duct cross sectional area. In the above equation, the absorption of the losses due to to the influence of thermal conduction and viscosity within the fluid element is assumed to much smaller than the absorption induced by the duct walls [13].

To take the effect of viscous thermal damping on the wave propagation when a mean flow is present, the effect of the acoustic boundary layer can be modelled as an equivalent impedance at the boundaries for the acoustic mode, as long as the acoustic boundary layer is much smaller than the cross sectional dimensions of the duct. The wave numbers for rectangular ducts are given in [22, 25] and for circular ducts they can be found in [21, 26, 27].

In the above models, a uniform mean flow is assumed which only takes into account the convective effects of the mean flow on the wave propagation. For ducted flows, the mean flow profile is not uniform over the cross section creating refraction of the acoustic wave. Furthermore, the presence of turbulence leads to acoustic absorption, which is most apparent when the acoustic boundary layer thickness is larger the turbulent boundary layer [28, 29]. These effects can be of importance under specific conditions.

3.4   Scattering matrix

The scattering matrix is a concept used in various branches of physics, such as electronics where it describes the relation between electrical quantities at different electric lines of an electric network [30, 31]. In an analogous way, the scattering matrix for acoustic networks

relates the acoustic fields at different physical ports to each other. In the scattering matrix representation, the sound fields are described by propagating waves and the scattering matrix relates the incident to the outgoing waves from each port. Now consider a device which has N number of physical ports. At each port, the sound field can be decomposed using equation (3.50) and the relation between the waves propagating to and away from the object is then given by the scattering matrix $\boldsymbol{S}$.

The scattering matrix, $\boldsymbol{S} \in \mathbb{C}^{\mathscr{L}^- \times \mathscr{L}^+}$, with $\mathscr{L}^+$ the number of incident modes and $\mathscr{L}^-$ the number of modes propagating away from the object, describes the relation between the fields propagating towards and away from the object.

The relation between the acoustic field propagating to and away from the object is given by,

$$\boldsymbol{p}^- = \boldsymbol{S}\boldsymbol{p}^+, \tag{3.57}$$

where the vectors $\boldsymbol{p}^+$ and $\boldsymbol{p}^-$ are a concatenation of modal amplitudes respectively travelling towards and away from the object from all the N ports.

To simplify the notation, from here onward the notation $\boldsymbol{p}^\pm$ will be used to indicate that the relation holds for both the waves traveling to, $\boldsymbol{p}^+$, and away, $\boldsymbol{p}^-$, from the object. The vectors $\boldsymbol{p}^\pm$ are given by,

$$\boldsymbol{p}^\pm = \begin{bmatrix} \boldsymbol{p}_1^\pm & \cdots & \boldsymbol{p}_n^\pm & \cdots & \boldsymbol{p}_N^\pm \end{bmatrix}^T \in \mathbb{C}^{1 \times \mathscr{L}^\pm}, \tag{3.58}$$

where $\boldsymbol{p}_n^\pm \in \mathbb{C}^{1 \times L^\pm}$, with $L^\pm$ the number of incident and scattered modes respectively, propagating in a specific duct n,

$$\boldsymbol{p}_n^\pm = \begin{bmatrix} p_1^\pm & \cdots & p_l^\pm & \cdots & p_L^\pm \end{bmatrix}^T. \tag{3.59}$$

The scattering matrix can be determined from experimental or numerical data by solving,

$$\boldsymbol{P}^- = \boldsymbol{S}\boldsymbol{P}^+, \tag{3.60}$$

where the matrices $\boldsymbol{P}^\pm$ are a concatenation of the $\mathscr{K}$ measured vectors $\boldsymbol{p}^\pm$

$$\boldsymbol{P}^\pm = \begin{bmatrix} \boldsymbol{p}_1^\pm \cdots \boldsymbol{p}_k^\pm \cdots \boldsymbol{p}_{\mathscr{K}}^\pm \end{bmatrix}, \boldsymbol{P}^\pm \in \mathbb{C}^{\mathscr{L}^\pm \times \mathscr{K}}. \tag{3.61}$$

To determine the scattering matrix using (3.60), at least $\mathscr{K} \geq \max(\mathscr{L}^+, \mathscr{L}^-)$ linearly independent incident and reflected sound fields have to be measured, such that both measured matrices are of full rank, $\mathrm{rank}\left(\boldsymbol{P}^\pm\right) = \mathscr{L}^\pm$.

Wave decomposition

The vectors $\boldsymbol{p}_n^\pm$ describing the waves that are present in each duct n can be determined with the so called wave-decomposition method. The pressure at different positions is measured,

and using the modal representation, equation (3.50), a linear system of equations can be constructed,

$$
\boldsymbol{\Psi}_n \begin{bmatrix} p_n^+ \\ p_n^- \end{bmatrix} = \begin{bmatrix} p_i \\ \vdots \\ p_I \end{bmatrix}, \tag{3.62}
$$

where p_i is the pressure measured at the position $\boldsymbol{x}_i = [x_i, y_i, z_i]$ in the duct. The matrix $\boldsymbol{\Psi}_n$ relates the pressures at a certain position in duct n with the modal amplitudes and is given by,

$$
\boldsymbol{\Psi}_n = \begin{bmatrix} \boldsymbol{\Psi}_1 & \dots \boldsymbol{\Psi}_i & \dots \boldsymbol{\Psi}_I \end{bmatrix}, \boldsymbol{\Psi}_n \in \mathbb{C}^{LxI}, \tag{3.63}
$$

where I is the number of microphone positions and $L = L^+ + L^-$ the number of modes present in the duct. The rows in $\boldsymbol{\Psi}_n$ are given by

$$
\boldsymbol{\Psi}_i = \begin{bmatrix} \psi_1(M, y_i, z_i)e^{-ik_1(M)x_i} \\ \vdots \\ \psi_l(M, y_i, z_i)e^{-ik_l(M)x_i} \\ \psi_1(-M, y_i, z_i)e^{ik_1(-M)x_i} \\ \vdots \\ \psi_l(-M, y_i, z_i)e^{ik_l(-M)x_i} \end{bmatrix}^T. \tag{3.64}
$$

To solve the system (3.62), the pressure should be measured at $I \geq L^+ + L^-$ different positions such that the matrix $\boldsymbol{\Psi}_n$ is of full rank $\mathrm{rank}\left(\boldsymbol{\Psi}_n\right) = L^+ + L^-$.

3.5   Summary

In this chapter an overview of the acoustic theory has been given. The presence of the acoustic boundary layer has been shown using the linearised Navier-Stokes Fourier model of a compressible fluid. Under the assumption that there is no mean flow, the equations have been rewritten and represented by three wave equations. The fields associated with the wave equations have been identified as the acoustic mode, the entropy mode and the vorticity mode. The latter two modes exist close to boundaries and create the acoustic boundary layer.

When acoustic waves are confined by waveguides, whose properties are not depend on the axial direction, the acoustic field in the waveguides can be decomposed in acoustic modes. With the modal representation of the acoustic fields in ducts, the amplitude and phase of the individual modes can be determined using the wave decomposition method. Using the acoustic modes, the concept of the scattering matrix has been introduced which relates the acoustic modes that are propagating towards an object to the modes that are travelling away from the object.

CHAPTER 4

Assessing the quality of acoustic scattering matrices

In this chapter, linear methods to determine the standard deviation of scattering matrix coefficients is investigated. The uncertainty in measured scattering matrices is assessed using a linear uncertainty analysis and the results are compared against Monte-Carlo simulations. It is shown that for plane waves, a linear uncertainty analysis, applied to the wave decomposition method, gives correct results when three conditions are satisfied. For higher order mode measurements, the number of conditions that have to be satisfied increases rapidly and the linear analysis becomes an unsuitable choice to determine the uncertainty on the scattering matrix coefficients. As the linear uncertainty analysis is most suitable for the plane wave range, an alternative linear method to assess the quality of the measurements is investigated. The method is based on matrix perturbation theory and the information is obtained in the form of partial condition numbers. This method gives only qualitative information, but the implementation is straightforward.

4.1 Introduction

The interest in measuring the scattering matrix for higher order modes in ducts with flow has increased recently and measurements have been made on rectangular and circular ducts [25, 32, 33]. One of the advantages of including higher order modes is the possibility to increase the frequency range in which measurements can be made. Recently, new models are proposed to describe the wave propagation constants for plane waves and higher order

modes in turbulent pipe flows [25, 34]. To verify these models, it is necessary to perform precise acoustic measurements where the uncertainty in the measurement data has been assessed.

For plane waves, the errors that can arise using the two-microphone methods are well known and are described qualitatively in [35–37], with generalized optimality conditions described in [35, 36]. Methods to reduce systematic errors are described in [38–41] and techniques to quantitatively assess the measurement uncertainty have been described in [5].

In comparison, investigations of the errors in measurements with higher order modes have not received the same attention. Efforts to reduce systematic errors and improve the accuracy of the measurement results for higher order modes have been recently published. For example, Sack et al. investigated the sensitivity of the modal decomposition results with respect to sensor and source positions [4]. Suzuki and Day investigated the use of different algorithms to decompose the sound field in the various wave components [42]. The lack of design guidelines can partially be explained by the fact that the number of free parameters are significantly increased compared to that of the two-microphone method for plane waves, making it difficult to create generalized optimality conditions, such as those derived by Bodén and Åbom [35, 36].

To compare model predictions and measurements with each other, the uncertainty in the measurements has to be known to make definitive statements on the agreement. Also, the uncertainty itself can be used to assess the quality of the measurements and determine the contribution of individual error sources, helpful when improving the measurements.

Two methods are often used to determine the uncertainty of measurements. The first is the multi-variate analysis [43], which is based on a linear approximation of the equation describing the relation between the measured variables, for example the transfer functions, and the quantity of interest, for example the scattering coefficients. The second method, the Monte-Carlo method [43], uses a numerical approach where the inputs are considered as random variables and a set of measurement samples are generated based on the statistical properties of the inputs. The quantity of interest is calculated for each set of input samples and the resulting statistical properties of the outputs can be calculated.

The benefit of the Monte-Carlo method is that it includes the effect of non-linear error propagation, however the drawback of the method is the computational time. On the other hand, the multi-variate analysis is based on an analytical approach and is significantly faster, however it can only take into account linear error propagation.

The purpose of this chapter is to investigate if a linear multi-variate approximation is sufficient to quantify the uncertainty of higher order modes measurements. A subject closely related to the linear uncertainty analysis is the theory of matrix perturbations. With meth-

ods from matrix perturbation theory, it is possible to determine the sensitivity of the wave decomposition method to input perturbation using analytical methods. Such an approach is beneficial in the process of designing of new setups as the solution is straightforward to implement and computationally fast, but it only gives qualitative information.

The linear uncertainty analysis will be investigated for higher order mode scattering matrices using the multi-microphone method [44] in a generalized way. Only solutions to the linear equation will be considered, without iterative refinement and the sound fields are assumed to be harmonic in time.

4.2 Linear uncertainty analysis

The elements of the scattering matrix S (introduced in section 3.4), also called scattering coefficients, are complex variables relating the amplitude and phase of in-going to out-going modes. When performing a measurement, there is always an uncertainty associated with the measured quantities, which will lead to an uncertainty in the obtained scattering coefficients.

Some measured quantities and the scattering coefficients are complex and to describe their uncertainty, they are decomposed in the real part u and the imaginary part v, $z = [u\ v]^T \in \mathbb{R}^2$. If the real and imaginary parts of z are normally distributed, the joint probability density function can be fully described by the variance of the real and imaginary part and the covariance between them [45, 46],

$$p(u, v) = \frac{1}{2\pi \det^{1/2} \boldsymbol{R}_{zz}} \exp\left(-\frac{1}{2}\boldsymbol{z}^T \boldsymbol{R}_{zz}^{-1} \boldsymbol{z}\right), \qquad (4.1)$$

where the covariance matrix is given by $\boldsymbol{R}_{zz}$,

$$\mathrm{cov}(z) = \boldsymbol{R}_{zz} = \mathrm{E}\left[(\boldsymbol{z} - \boldsymbol{\mu_z})(\boldsymbol{z} - \boldsymbol{\mu_z})^T\right], \qquad (4.2)$$

where $\mathrm{E}\left[\cdot\right]$ is the expectation operator and $\boldsymbol{\mu_z} = \mathrm{E}(\boldsymbol{z})$.

The purpose of an uncertainty analysis, is to determine the statistical properties of the parameters of interest, such as the elements of S as function of the statistical properties of the known parameters, such as the measured parameters p_i.

Consider a general function $\boldsymbol{y} = f(\boldsymbol{z})$ which represent the relationship between the parameters of interest $\boldsymbol{y}$ and the measured parameters $\boldsymbol{z}$. If this relationship can be considered linear in the neighbourhood of $\boldsymbol{z}$, for which the size is proportional to the size of covariances of $\boldsymbol{z}$, a linear multi-variate uncertainty analysis can be used to relate the covariance matrices of the known parameters $\boldsymbol{z}$ to the covariance matrices of the parameters of interest $\boldsymbol{y}$.

The linear multi-variate uncertainty analysis is based on a first order Taylor's expansion of the function f. It is possible to take into account higher order terms in the Taylor ex-

pansion and include higher order statistical moments into the analysis [47], however the computations quickly become cumbersome.

Considering only the first order Taylor expansion of $\boldsymbol{y} = f(\boldsymbol{x})$, the covariance matrix of the parameter of interest is related to the covariance matrix of the measured parameters by [43, 48],

$$\operatorname{cov} \hat{y}_k \approx \sum_{i}^{N} \sum_{j}^{N} \boldsymbol{J}_i^k(f) \operatorname{cov}(\boldsymbol{z}_i, \boldsymbol{z}_j) \boldsymbol{J}_j^k(f), \tag{4.3}$$

where $\operatorname{cov} \hat{y}_k \in \mathbb{R}^{2x2}$ represents the covariance matrix of a random complex element of the output vector $\boldsymbol{y}$ and $\boldsymbol{J}_i^k$ the complex Jacobian matrix of the kth output value w.r.t to i^{th} input variable evaluated at the position $z_i \in \mathbb{C}$,

$$\boldsymbol{J}_j^k = \left[\frac{\partial}{\partial u_k} \boldsymbol{z}_j \quad \frac{\partial}{\partial v_k} \boldsymbol{z}_j \right] \in \mathbb{R}^{2x2}. \tag{4.4}$$

The cross-covariance $\operatorname{cov}(z_i, z_j)$ is given by

$$\operatorname{cov}(z_i, z_j) = \operatorname{E} \left[(\boldsymbol{z}_i - \boldsymbol{\mu}_{z_i})(\boldsymbol{z}_j - \boldsymbol{\mu}_{z_j})^T \right]. \tag{4.5}$$

An advantage of the linear analysis is that the contribution from each error source to the overall uncertainty can be easily calculated which is beneficial in the design and improvement of experimental setups.

If the relationship $f(\boldsymbol{z})$ is not linear in the neighbourhood of $\boldsymbol{z}$, other methods, such as the Monte-Carlo method, have to be used to determine the statistical parameters of $\boldsymbol{y}$. The Monte-Carlo method simulates many samples from a measurement based on the statistical properties of the input variables. From the samples, the mean value and statistical parameters of the output values are calculated [43]. The method allows the calculation of the statistical properties for an arbitrary relation between the input and output parameters, but it is computationally heavy.

As the linear uncertainty analysis is a useful tool to express and analyze the uncertainty analysis fast, the question arises when the analysis is appropriate without performing a validation against a Monte-Carlo simulation. By analyzing the sources of non-linearity when determining the N-port scattering matrix, estimators can be derived to determine if a linear analysis gives correct results.

There are three sources of non-linearity when calculating the scattering matrix. Two are related by the matrix inversion needed to obtain the solution to equations (3.60) and (3.62). The third source of non-linearity are the relationships of the matrix elements in $\boldsymbol{\Psi}$ (defined in 3.4) with respect to their arguments.

The first source of non-linearity that we consider are perturbations of the elements of $\boldsymbol{\Psi}$. Consider the Taylor expansion of the matrix,

$$\boldsymbol{\Psi}(a + \epsilon) = \boldsymbol{\Psi} + \frac{\partial \boldsymbol{\Psi}}{\partial a} \epsilon + \frac{1}{2} \frac{\partial^2 \boldsymbol{\Psi}}{\partial a^2} \epsilon^2 + \mathcal{O}\left(\epsilon^3\right), \tag{4.6}$$

where a and ϵ represent any input parameter and its error, respectively. The condition to have linear error propagation is that all the second and higher order terms have to be much smaller than the first order terms,

$$\left\| \left[\epsilon \left(\frac{1}{2} \frac{\partial^2 \boldsymbol{\Psi}}{\partial a^2} \right) + \mathcal{O}\left(\epsilon^2\right) \right] \oslash \left(\frac{\partial \boldsymbol{\Psi}}{\partial a} \right) \right\|_\infty << 1, \tag{4.7}$$

where $\oslash$ represent element wise division. The above condition has to be satisfied for all uncertain input parameters to ensure linear error propagation.

The second source of non-linearity is the method used to solve the wave decomposition equation, (3.62). The solution is obtained by pre-multiplying the equations by a Moore-Penrose pseudo-inverse $\boldsymbol{\Psi}^\dagger$, for which small perturbations to $\boldsymbol{\Psi}$ could lead to non-linear perturbations on the inverse. In general, the pseudo-inverse of a perturbed matrix is non-continuous [49],

$$\lim_{\epsilon \to 0} (\boldsymbol{A} + \epsilon \boldsymbol{B})^\dagger \neq \boldsymbol{A}^\dagger. \tag{4.8}$$

However, in the special case that the perturbations on matrix $\boldsymbol{A}$ are acute [49], that is, the perturbations do not change the rank of $\boldsymbol{A}$, $\mathscr{R}(\boldsymbol{A}) = \mathscr{R}(\boldsymbol{A} + \epsilon \boldsymbol{B})$, the matrix inverse is continuous and can be approximated by a Taylor series [50].

Consider now the case for the matrix $\boldsymbol{\Psi}$. If the perturbations are small and acute, then the perturbation to the matrix can be written as $\epsilon \boldsymbol{E}$ by neglecting the second order terms in (4.6), with

$$\boldsymbol{E} = \frac{\partial \boldsymbol{\Psi}}{\partial a}, \tag{4.9}$$

and the pseudo-inverse can be approximated by,

$$(\boldsymbol{\Psi} + \epsilon \boldsymbol{E})^\dagger = \boldsymbol{\Psi}^\dagger + \sum_{k=1}^{\infty} (-1)^k \left(\boldsymbol{\Psi}^\dagger \boldsymbol{E} \right)^k \boldsymbol{\Psi}^\dagger \epsilon^k, \tag{4.10}$$

for $\| \epsilon \boldsymbol{\Psi}^\dagger \boldsymbol{E} \| < 1$, to have the series converge. Comparing the size of the second order term with the first order term of (4.10), with a suitable norm,

$$\| \epsilon \boldsymbol{\Psi}^\dagger \boldsymbol{E} \| << 1, \tag{4.11}$$

must be satisfied to ensure that the inversion process is linear. A more conservative but insightful bound is given by,

$$\frac{\| \epsilon \boldsymbol{E} \|_2}{\| \boldsymbol{\Psi} \|_2} \kappa(\boldsymbol{\Psi}) << 1, \tag{4.12}$$

which shows that when the relative perturbations on the matrix $\boldsymbol{\Psi}$ are small, measured with a suitable norm, they can lead to a non-linear contribution to the inverse of the matrix through a badly conditioned matrix $\boldsymbol{\Psi}$.

The third source of non-linearity that can be identified is the method used to solve for the scattering matrix, equation (3.60). It is also solved by pre-multiplying the equation with $\boldsymbol{P}^{+\dagger}$ and the above reasoning holds as well for this source. It becomes clear from equation (4.12), that the condition number of $\boldsymbol{P}^+$ has to be small to have a linear error propagation. Therefore, when measuring the scattering matrix, acoustic fields for which the columns of $\boldsymbol{P}^+$ are orthogonal to each other and have a similar magnitude should be used. One way to realize this is to excite only one mode at a particular port for each measurement in equation (3.61) and have non-reflective boundary conditions for all the other modes at the terminations of each port.

To apply the linear uncertainty analysis, both conditions, (4.7) and (4.11), should hold for any uncertain input parameter. When higher order modes are cut-on, the number of necessary conditions increases rapidly and it becomes cumbersome to keep track of all the conditions. Unfortunately no specific sets of conditions can be identified which are mutually exclusive and thus all the conditions have to be satisfied to have linear error propagation. Only when plane waves are present, some general statements can be made if a linear uncertainty analysis can be applied.

In the case of plane waves three parameters play a role in the wave decomposition, which are the axial position of the microphone, the Mach number and the free field speed of sound. With the help of (4.7), the linearity conditions for these three parameters can be derived.

The first condition is with respect to the error in the microphone distance,

$$\| \frac{\epsilon_x k_0}{2} \frac{M}{1 - M^2} \frac{1}{} \| << 1. \tag{4.13}$$

Herein ϵ_x is the error in the microphone distance. The second condition is with respect to the error in the Mach number ϵ_M and is given by,

$$\| \frac{\epsilon_M}{2} \left[\frac{i k_0 x}{(M \pm 1)^2} - \frac{2}{(M \pm 1)} \right] \| << 1. \tag{4.14}$$

The third condition is with respect to the error affecting the free field wave number, which is related to the speed of sound. The speed of sound can be estimated using $c_0 = \sqrt{\gamma R T}$, where γ is the ratio of specific heats, R the gas constant of the medium and T the temperature of the gas. Considering the uncertainty in the temperature ϵ_T the condition that has to be satisfied can be written as,

$$\| \frac{\epsilon_T}{2} \left[\frac{\pm i \omega x (1 + M)}{2T \sqrt{\gamma R T} (M^2 - 1)} - \frac{3}{2T} \right] \| << 1. \tag{4.15}$$

It can be seen that the ratios in (4.13), (4.14) and (4.15) increase with frequency and therefore, there will be an upper frequency limit where the linear uncertainty analysis will not be valid anymore. All these conditions have to be satisfied to ensure that the error in the wave decomposition process is linear. As the solution to the equation is a linear function of the measured pressures p, these errors will always propagate linearly to the amplitudes of the propagating waves.

4.3 Perturbation theory

The linear multi-variate analysis is an effective method to determine the uncertainty, but as argued in the previous sections, it becomes difficult to correctly determine the uncertainty using linear methods when higher order modes are present. In addition, even though the linear uncertainty analysis is computationally fast, the implementation can be cumbersome. On the other hand, when designing a setup, the use of Monte-Carlo methods to estimate the uncertainty could be too time consuming.

An alternative way to assess the quality of the measurements is with an analysis based on condition numbers, which can be computed relatively easy. Using condition numbers, the sensitivity of the measurement results to perturbations (errors) can be examined to obtain a qualitative understanding and can be of interest when designing or analysing a setup. In the field of computer science and scientific computing, the response of linear systems to perturbations is actively studied and the following section is a recapitulation of material that can be found in [49, 51–53]

The sensitivity of a solution of a system of equations is defined as a condition number of the system. Consider a map g, which maps an m-dimensional data space to a n dimensional solution space with $n \leq m$, $g \; : \; \mathbb{R}^m \rightarrow \mathbb{R}^n$. The condition number of the system gives a measure of the sensitivity of the map $g(\boldsymbol{y}_0)$ to perturbations in the data space $\boldsymbol{y}_0$.

The condition number of the system is defined by [52, 53],

$$K(\boldsymbol{y}_0) = \lim_{\delta \to 0} \sup_{0 < \|\boldsymbol{y}_0 - \boldsymbol{y}\|_{\mathscr{D}} \leq \delta} \frac{\|g(\boldsymbol{y}_0) - g(\boldsymbol{y})\|_{\mathscr{S}}}{\|\boldsymbol{y}_0 - \boldsymbol{y}\|_{\mathscr{D}}}, \tag{4.16}$$

where $\|.\|_{\mathscr{D}}$ is the norm used in the data space and $\|.\|_{\mathscr{S}}$ the norm used in the solution space to measure the size of a vector. The condition number of the system represents an asymptotic sensitivity to infinitesimal perturbations and is dependent on the choice of the norms for the data and solution space. The relative condition number is defined as,

$$K^{(rel)}(\boldsymbol{y}_0) = K(\boldsymbol{y}_0)\|\boldsymbol{y}_0\|_{\mathscr{D}}/\|g(\boldsymbol{y}_0)\|_{\mathscr{S}}. \tag{4.17}$$

In the current study, the map is given by the solution to an (over)-determined system of linear equations, (3.62) and (3.60). A condition number that is sometimes used to express

the sensitivity of a solution to linear equations $Ax = b$ is given by,

$$\kappa(A) \equiv \|A\|_2 \, \|A^{-1}\|_2, \tag{4.18}$$

where $\| \cdot \|_2$ is the two-norm. This condition number gives an upper bound for the sensitivity of the solution to perturbations to the system. Equation (4.18) is a special case of equation (4.17), when a determined set of equations is considered, only A is perturbed and the perturbations in the data space and solution space are measured by the two-norm [51, 54].

In general, equations (3.62) and (3.57) are over-determined systems, which are more prone to ill-conditioning as the sensitivity can scale with the square root of the condition number κ, as defined by (4.18) [54–56]. Therefore, equation (4.18) is not the best way to determine the sensitivity of these systems of equations. Further more, the above condition number only gives information on the size of the perturbations on the solution vector x and not a specific element x_i of the solution vector.

Arioli et al. [52] give methods to determine the condition numbers for over-determined systems of equations. These condition numbers can be determined for specific elements of the solution vector and for perturbations on A and b. The results are obtained for maps in the real domain $\mathbb{R}$, but in the following it is assumed that the results also hold for the complex domain $\mathbb{C}$ as the system of equations are continuous in the complex domain and the perturbations are assumed to be acute, implying that the complete system is continuous and thus Fréchet-differentiable.

The theorem by Arioli et al.[52, Theorem 1] allows deriving the exact condition number in the form of equation (4.16) under special conditions. Consider a map g of a linear least squares solution $\min_{x \in \mathbb{R}^n} \|Ax - b\|_2$, which is projected on to a k dimensional space $L^T x$, $L \in \mathbb{R}^{n \times k}$. The map is given by,

$$
\begin{aligned}
g \; : \; & \mathbb{C}^{m \times n} \mathrm{x} \mathbb{C}^m \to \mathbb{C}^k, \\
& A, b \mapsto g(A, b) = L^T x(A, b) = L^T (A^T A)^{-1} A^T b.
\end{aligned} \tag{4.19}
$$

The projection on the k dimensional space allows the determination of the condition number for a specific element of the solution vector x, by choosing L such that it is a column of the identity matrix.

Values, as opposed to bounds, of the condition number of the above system can be derived, when suitable norms for the solution and data space are taken. For the solution space the two-norm is used. For the data space, the following norm is used,

$$\|(A, b)\|_F = \sqrt{\alpha^2 \|A\|_F^2 + \beta^2 \|b\|_2^2}, \quad \alpha, \beta > 0 \in \mathbb{R}, \tag{4.20}$$

where $\| \cdot \|_F$ stands for the Frobenius norm and $\| \cdot \|_2$ for the two-norm. The Frobenius norm is given by,

$$\|A\|_F = \sqrt{\text{trace}\,[A^*A]}, \tag{4.21}$$

where A^* denotes the conjugate transpose of A. With the above norm, it is possible to estimate the effect of perturbations on A and b separately. For values of $\alpha \to \infty$ the condition number of the problem is obtained where mainly b is perturbed and for values of $\beta \to \infty$ the condition number of the problem is obtained where mainly A is perturbed [53].

The condition numbers as defined in (4.16) can then be computed with the theorem [52, Theorem 1], given by:

Theorem 1. *Let $A = U\Sigma V^T$ be the thin singular value decomposition of A, with $\Sigma = \text{diag}(\sigma_i)$ and $\sigma_1 \geq \sigma_2 \ldots \geq \sigma_n \geq 0$. The absolute condition number of $g(A, b) = L^T x(A, b)$, where the norm of the solution space is the Frobenius norm, is given by*

$$K(L^T x) = \|SV^T L\|_2, \tag{4.22}$$

where $S \in \mathbb{R}^{n \times n}$ is the diagonal matrix with diagonal elements,

$$S_{ii} = \sigma_i^{-1} \sqrt{\frac{\sigma_i^{-2}\|r\|_2^2 + \|x\|_2^2}{\alpha^2} + \frac{1}{\beta^2}}. \tag{4.23}$$

where r, the residual, is given by $r = Ax - b$.

The thin singular value decomposition is given by the singular value decomposition where only the column vectors of U and the row vectors of V^T are calculated that correspond to the non zero singular values σ_i. With the above condition number, (4.22), the sensitivity of solution to the wave decomposition step, equation (3.62) can be calculated for example. Letting $\alpha \to \infty$ in (4.23), the effect of perturbations, when only p is perturbed can be investigated. On the other hand when taking $\beta \to \infty$ the condition number reflects the sensitivity of the solution only to perturbations on Ψ. By taking L as a column of the identity matrix, component wise condition numbers can be obtained, relating the sensitivity of specific components of $\left[p^+\ p^-\right]^T$ to perturbations of the data space for a specific choice of α and β.

4.4   Results and discussion

In this section, results from the measurement of the reflection coefficient of a rigid wall will be presented. Two different experimental setups are used, one to determine the reflection coefficient using plane waves and the second where the reflection coefficients are determined for higher order modes. One advantage of using a rigid wall as the measurement

object is that the acoustic impedance of the wall is homogeneous and there is no scattering of energy between different modes [57, Chapter 9.3]. Therefore, only one acoustic field has to be measured to determine the reflection coefficient of each of the modes. This reduces the number of variables used in the computation significantly and it becomes easier to analyse the sources of the observed errors.

For the plane wave results, confidence intervals will be shown, obtained with the linear uncertainty analysis. The obtained covariance matrix from the linear uncertainty analysis will be compared against the covariance matrix obtained from a Monte-Carlo simulation. For the higher order modes, no bounds will be derived as it is shown that the linear uncertainty analysis is unsuitable to determine these bounds for the higher order mode reflection coefficients. The results from the higher order mode measurements show the presence of a random error in the obtained scattering coefficients and with the help of the perturbation theory, a plausible explanation is found for the observed scatter.

No detailed information about the setups will be given, as the focus of the chapter is on the use of methods to assess the measurement quality, but information can be found in the cited references and in chapter 5. The first setup is used to measure within the plane wave range and it consists of a circular duct where one loudspeaker is attached to the wall of the duct to excite the sound field. The field is sampled by four microphones flush mounted in the side wall of the duct [58]. The second setup is designed to measure higher order modes and the waveguide has a rectangular cross-section. A combination of four loudspeakers is used to excite the sound field, with each wall of the duct having one loudspeaker. The sound field is measured with 20 flush mounted microphones located at various positions in the duct walls [25, 59].

To calculate the uncertainty in the reflection coefficients, the uncertainties on the measured parameters have to be known. For the sake of argument, only errors in the temperature T, acoustic pressures p and microphone distances x_i are considered, as these errors are the most significant [58]. In table 4.1 the used uncertainties are given for two different cases. The uncertainties for the first case are based on experimental and technical information, see also chapter 5 and appendix A.3. For the first case, the uncertainty in the temperature is taken to be 0.1 °C Celsius, the uncertainty in the microphone position 0.1 mm and the uncertainty in the measured acoustic pressures to be normal circular distributed in the complex domain with a radius of 1% of the absolute value of the measured pressure. For the second case, the uncertainty of the microphone positions has been increased to 1 mm, to show non-linear error propagation. To assess the validity of the multi-variate analysis, the determinants of the covariance matrices obtained from the multi-variate analysis, det Σ_{MC}, is compared against the determinant obtained from the Monte-Carlo simulation, det Σ_{MVA},

$$\text{Covar ratio} \equiv \det \Sigma_{\mathrm{MC}} / \det \Sigma_{\mathrm{MVA}} - 1. \tag{4.24}$$

		Case 1	Case 2
Temperature	[°C]	0.1	0.1
Distance	[mm]	0.1	1
Pressure	[Pa]	$|p_i|10^{-3}\boldsymbol{I}$	$|p_i|10^{-3}\boldsymbol{I}$

Table 4.1: *Table of the standard deviation of the input variables for the two different cases*
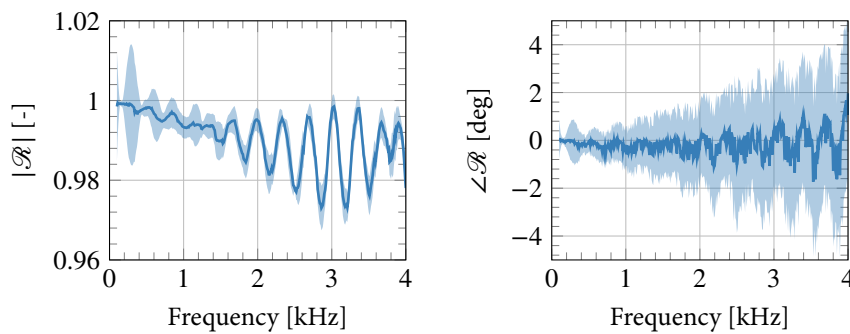
Figure 4.1: *The measured reflection coefficient of the rigid wall (———) and the 95% confidence interval (   ).*

This measure gives the relative difference in the size of the uncertainty region obtained from the two methods

First the results in the plane wave region will be discussed. In figure 4.1, the measured phase and magnitude of the reflection coefficient is shown together with the 95% confidence interval. It is customary to describe the scattering coefficients in polar form and the uncertainty can be expressed in a Cartesian reference frame, coinciding with the direction of the complex phasor defined by the reflection coefficient, by performing a transform on the covariance matrix [60]. When the uncertainties in the new Cartesian coordinate systems are small compared to the absolute value of the scattering coefficient, then the uncertainty can be expressed as uncertainties in phase and absolute value of the mean vector [60].

Due to the linear nature of the analysis, equation (4.3), the total variance on the measurement is a superposition of the variances created by the individual uncertain inputs and the total variance can be analyzed to determine the sources that contribute the most to the overall error. In figure 4.2 a breakdown of the variance is given for both the magnitude and the phase of the reflection coefficient. The errors contributing the most are different for the magnitude and phase. For the absolute value, the dominant factor is the uncertainty in the measured transfer functions. On the other hand, the uncertainty in the phase is dominated
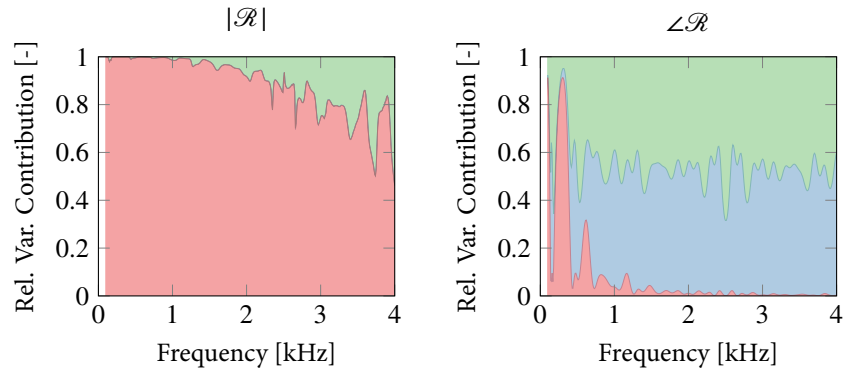
Figure 4.2: *The relative contribution of each error source, microphone pressures (▬), temperature (▬) and microphone positions (▬) to the variance of the error in the magnitude of the reflection coefficient (left) and the phase of the reflection coefficient (right).*
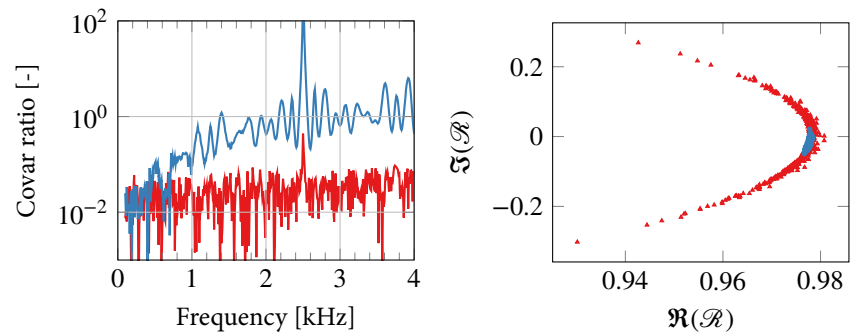

Figure 4.3: *(Left) Relative difference between the determinant of the covariance matrix determined using the Monte-Carlo method and the linear multi-variate analysis as function of frequency. (Right) Scatter plot of the reflection coefficient at 2500 Hz calculated with the Monte-Carlo method for the two different cases. The different colors,(——, ▲) and (——, ●) represent respectively Case 1 and Case 2 in table 4.1.*

by the error related to the microphone positions and speed of sound.

In figure 4.3, the ratio of the covariance matrices obtained for the reflection coefficient is shown for the two different sets of uncertainties given in table 4.1. For the first case, the ratio is below 10% for most frequencies, showing that the linear analysis accurately describes the covariance matrix. The covariance ratio slowly increases with frequency, as the ratio between the second order and first order term of the Taylor expansion of Ψ increases with frequency, (4.13,4.15). On the other hand, for the second case, the covariance ratio is much larger, indicating that the linear analysis can not be used to determined the covariance matrix for the set of uncertainties. This is surprising, as even for the second case the ratios, (4.13,4.15), are met.

The obtained covariance matrices of the amplitudes p_1^+ and p_1^- for both the Monte-Carlo simulation and the linear analysis compare well to each other, with a maximum relative covariance ratio of 10 %, for both sets of uncertainties as could be expected from the linearity conditions. The source of non-linearity is the determination of the reflection coefficient from the wave amplitudes. The largest discrepancy is seen at 2500Hz, and the obtained scatter plot of the Monte-Carlo simulation (Figure 4.3) shows the non-linear behavior. The reason for this non-linear error propagation can be explained by considering the Taylor expansion of the reflection coefficient with respect to the incident and reflected wave. The ratio between the second order terms to the first order terms is given by,

$$\frac{1}{2}\frac{\epsilon^+}{p^+}\frac{\epsilon^- + \mathscr{R}\epsilon^+}{\epsilon^- - \mathscr{R}\epsilon^+}. \tag{4.25}$$

If the errors on the incident and reflected pressure waves are almost equal, the linear terms, represented by the denominator in equation (4.25), cancel each other since $\mathscr{R} \approx 1$. When this happens, the error will propagate non-linearly even though that the overall error on the reflection coefficient can be small.

In the second part of this discussion, the focus is on the higher order modes. Because of the measurement object, there is no interaction between dissimilar modes and to calculate the scattering coefficients using equation (3.60), the information for each mode can be seen as a separate measurement. The matrix $\boldsymbol{P}^\pm$ can be written as a diagonal matrix, $\mathrm{diag}(p_1^\pm, \dots, p_l^\pm, \dots, p_L^\pm)$ and the computed scattering matrix, will reduce to a diagonal matrix with the reflection coefficients of each mode on the diagonal.

In figure 4.4 the reflection coefficient of the plane wave mode and the first higher order mode are shown for two different excitation configurations. For the first configuration, only one loudspeaker was used, situated on the top wall. For the second configuration, two loudspeakers mounted in the side walls and facing each other where used. Doak [61, 62] investigated the excitation of higher order modes in rectangular ducts and showed that the excitation strength of the specific modes is sensitive to both the spatial distribution of the
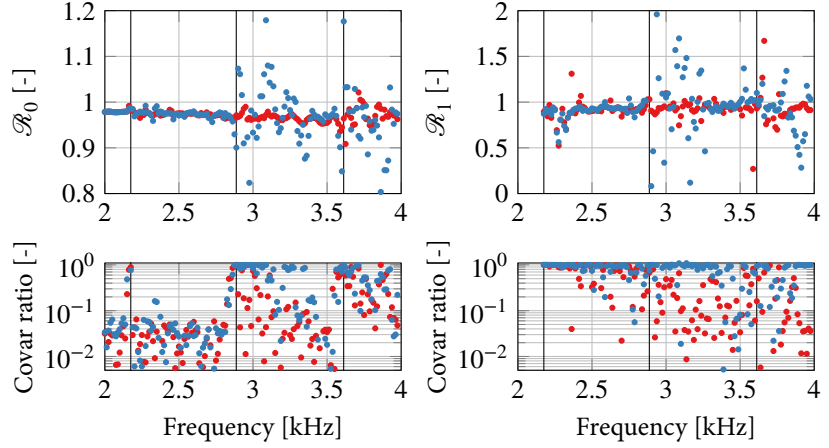
Figure 4.4: *Reflection coefficient for the plane wave mode (left) and the first higher order mode (right) as function of frequency for two different acoustic excitations, case 1 (●) and case 2 (●). The vertical lines denote the cut-on frequencies of the higher order modes*

excitation sources and the end conditions of the duct. Therefore, the two different configurations lead to different amplitudes of the ingoing waves. From the reflection coefficients it can be seen that after the cut-on of the second higher order mode, the plane wave and first higher order mode reflection coefficients for the second configuration show more scatter compared to the results from the first configuration.

In the bottom row of figure 4.4, the relative difference between the calculated covariance matrix for the reflection coefficient using the Monte-Carlo method and the multi-variate method is shown. The figure shows that after the second cut-on frequency, the covariance matrix for the plane waves is not correctly described by the linear analysis. The relative difference between the covariance matrices for the reflection coefficient for the first higher order mode is large for almost all frequencies, and the results obtained from the multi-variate method can not be used.

The results from the wave decomposition step, equation (3.62), show that the covariance matrices determined for the individual components with the two methods are still in good agreement with each before the third cut-on frequency except close to the cut-on frequencies. Here the covariance matrices obtained by the linear analysis and the Monte-Carl simulation show larger differences as the condition number of Ψ is large, due to small wave number k_l for the cut-on higher order mode, in agreement with the condition (4.12). The difference between the covariance matrices of the reflection coefficients obtained by the linear method and the Monte-Carlo simulations is a consequence of the difference in
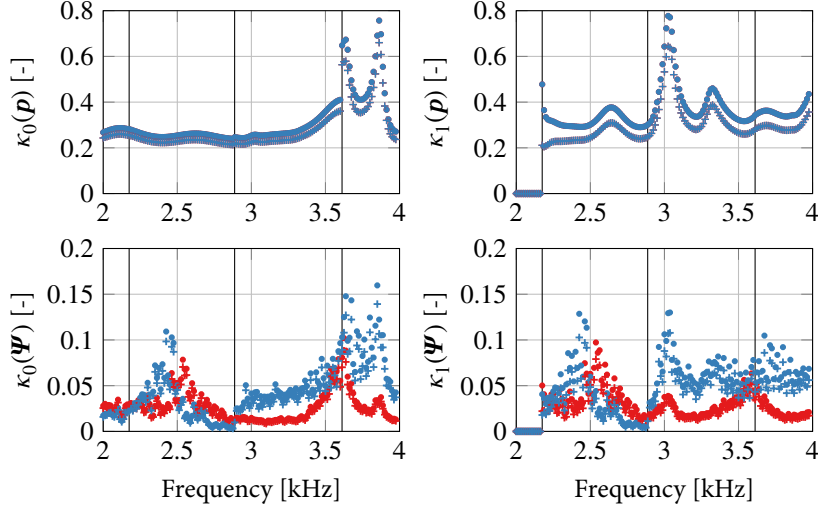
Figure 4.5: *Partial condition numbers for the wave amplitudes of the plane wave mode (left column) and the first higher order mode (right column) as function of frequency for two different acoustic excitations. The top row denotes the partial condition numbers based on perturbations of the measured pressures **p**, the bottom row shows the partial condition numbers based on perturbations of **Ψ**. The positive travelling waves are denoted by circles, (●, ●), and the negative travelling waves are denoted by pluses, (+, +), for case 1 (red) and case 2 (blue). The vertical lines denote the cut-on frequencies of the higher order modes.*

magnitude of the individual wave components, which will be shown below. The difference in magnitude of the individual components leads to that the small components have a large relative error, which leads to non-linear error propagation to the scattering matrix due to the inversion step, eq. (4.12), when determining the scattering matrix, eq. (3.60).

In figure 4.5, the condition number, based on perturbations of p for the individual wave components for the plane wave and first higher order mode are shown. For both the excitation cases these graphs are identical, since Ψ is identical for the two cases. As the absolute value of the measured pressures for the two different cases have similar magnitudes, the induced error on the wave amplitudes is of a similar magnitude. It can be seen that the components of the first higher order mode, the sensitivity to errors on the measured pressures shows a maximum at around 3000Hz and that the results of the plane wave components are most sensitive to perturbations after the third cut-on frequency.

In the same figure, the second row depicts the condition number, based on perturbations of Ψ. This condition number is similar for both cases, up to the cut-on of the second higher
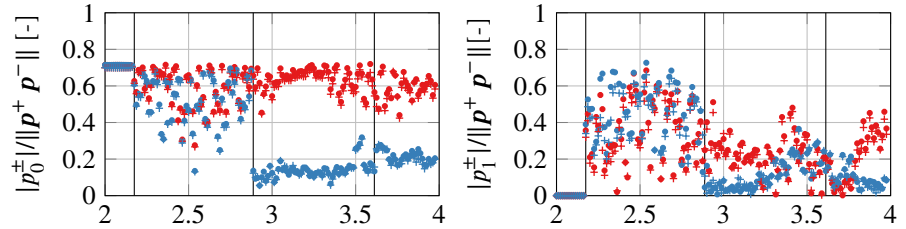
Figure 4.6: *Relative size of the wave amplitudes of the plane wave mode (left column) and the first higher order mode (right column) as function of frequency for two different acoustic excitations. Triangles denote the positive traveling waves and circles the negative traveling waves. The vertical lines denote the cut-on frequencies of the higher order modes The positive travelling waves are denoted by circles, (●, ●), and the negative travelling waves are denoted by triangles, (+, +), for case 1 (red) and case 2 (blue).*

order mode, after which the condition numbers of the first configuration are higher than those of the second configuration. The errors on $\mathbf{\Psi}$ are identical as they are not dependent on the excitation conditions and thus the results for the first configurations are more sensitive to errors than for the second configuration, which correlates with the scatter on the measured scattering coefficients.

The main reason why the second configuration is more sensitive can be appreciated by looking at the relative size of the wave amplitudes compared to the solution vector. The relative size is depicted in figure 4.6. It can be seen that for the second configuration, the relative amplitude of the plane wave and first higher order mode are lower than those of the first excitation case after the cut-on of the second higher order mode and it correlates with the increased scatter on the measured results.

It is shown by Chandrasekaran and Ipsen [56] that the partial condition number of the solution components is inversely related to the relative size of the solution component to the size of the solution vector,

$$K\left(p_l^{\pm}\right) \propto \frac{\|\mathbf{p^+ \, p^-}\|}{|p_l^{\pm}|}. \tag{4.26}$$

In this specific circumstance, the various modes do not interact with each other, because of the spatially uniform impedance that is being measured [57, Chapter 9.3]. Furthermore, the presence of the wall determine the ratio between the amplitude of the in- and out- going wave for a specific mode and the relative size of the amplitudes of each of the modes is solely determined by the excitation and end conditions at the excitation side. To obtain reliable and repeatable results, independent of the object to be measured, the amplitudes of the ingoing wave components have to be controlled. Another consequence of the large relative

errors, is that the resulting error on the reflection coefficient will depend non-linearly on the errors of the traveling wave amplitudes and a linear analysis can not be used to determine the uncertainty in the scattering coefficients.

4.5 Conclusion

The validity of the linear uncertainty analysis to determine the uncertainty in the scattering matrix coefficients for higher order modes has been investigated. It has been shown that a linear multi-variate analysis can only be used in specific circumstances and conditions have been derived when such an analysis gives valid information on the uncertainty bounds for the wave decomposition method.

For higher order modes, the amount of conditions increases significantly and no general conditions can be formulated for when a linear uncertainty analysis can be used. Therefore, to determine accurate uncertainty intervals, a Monte-Carlo method has to be used. If the use of a Monte-Carlo method on the complete determination is too time consuming, a two step approach could be considered where the uncertainty in the wave decomposition is assessed with a linear analysis and the uncertainty in the scattering matrix determined using a Monte-Carlo methods.

The experimental results for the higher order mode scattering matrices have been analyzed with the help of the partial condition numbers. The partial condition numbers are a computational inexpensive alternative to investigate the problem and give qualitative information on the measurement quality. Using the partial condition numbers, it has been shown that the difference in excitation levels for each of the mode is the main reason for the large variance in the measured reflection coefficients. To reduce these errors, measurements have to performed where the energy in the modes can be controlled.

Accuracy of impedance tube measurements

The impedance tube is an essential part in the determination of an acoustic scattering matrix and in this chapter various systematic errors that may be present in impedance tube measurements are discussed. Three sources of errors are discussed, pipe vibrations induced by the acoustic excitation, the effect of a slowly drifting ambient temperature and the finite dimensions of the microphones. By determining the reflection coefficient of a calibration standard, the rigid wall, the effect of the error sources are shown together with ways to reduce the systematic error.

5.1   Introduction

In the previous chapter, the experimental error in acoustic scattering matrices was assessed using uncertainty analyses.

In this chapter the accuracy of impedance tubes will be discussed. The accuracy describes the difference between the measured value and the true value of the quantity being measured. The impedance tube is an essential part of acoustic scattering matrix measurements. These tubes are used to determine the travelling waves towards and away from each of the ports of the object under study.

To determine the accuracy of measurements, a known value has to be measured. In the case of the impedance tube, a known impedance is that of a rigid wall. When not taking into account the effects of viscosity and thermal conductivity, the compliance of the wall is zero and an incident waves is completely reflected back. When the effects of viscosity

and thermal conductivity are taken into account, the acoustic wave excites also the so called entropy and vorticity wave (section 3.2). The presence of these waves is confined to the acoustic boundary layer close to the wall, but lead to a slight loss of acoustic energy in the reflected wave [13].

The systematic errors that are present in the setup have to be identified and taken into account. The only way to assess whether there is a systematic error is present, is the measurement of a calibration standard. To be able to reduce the systematic errors, the source of the error has to be removed from the measurements or included into the mathematical analyses.

An approach that can be used is the use of calibration impedances [39–41]. The calibration impedances consist of a rigid wall at different lengths and the systematic errors that are present can be taken into account using calibration factors obtained from measurements. Another approach is the optimization of the model parameters in the wave decomposition equation, such that the residual between the determined and measured pressures is minimized. In this way the presence of systematic errors in the model parameters can be minimized by creating the best fit with the measurements.

The drawback of the above approaches is that they rely on the fact that the model description of the wave propagation in the duct is correct. The model assumes that the measured pressure are only due to acoustic waves. However, if the walls of the duct are not completely rigid, structural waves can propagate which have different wave numbers and are not captured by the model and the use of calibration impedances will not yield the desired results.

In this chapter, the source of systematic errors that can arise in impedance tube measurements is discussed. The determination of the true origin of errors is in general not straightforward and in the first part of this chapter a comprehensive, but not exhaustive, overview of the origin and significance of systematic errors that can occur in impedance tubes will be given. As the list of errors is not exhaustive, there are still systematic errors which have not been accounted for. The subsequent chapter will discuss the remaining systematic errors.

5.2   Experimental setup

The measurement setup used to determine the presence of systematic errors consists of a waveguide which is terminated by the calibration standard, the rigid wall. A schematic overview of the measurement setup is given in figure 5.1. The waveguide is made of aluminium, is cylindrical and has an inner diameter of 50mm and wall thickness of 5mm. The rigid wall is made from steel and has a thickness of 3.5cm. The acoustic waveguide has
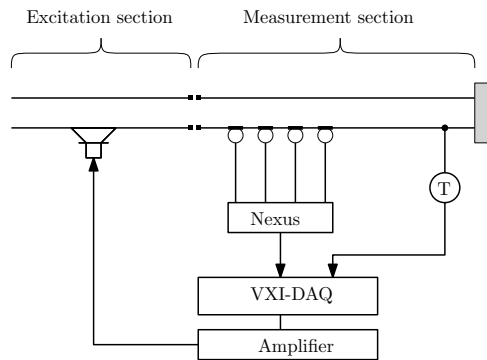
Figure 5.1: *Schematic of the experimental setup used to determine the reflection coefficient of a rigid wall.*

been disconnected between the excitation section and measurement section to reduce the influence of mechanically vibrations induced by the loudspeakers. The acoustic excitation was provided by a loudspeaker attached to the excitation section, far from the measurement section. A stepped sine excitation was used to obtain a high signal-to-noise ratio and the excitation order was randomized.

The pressure fluctuations were registered by four flush mounted Brüel and Kjær 1/4-inch condenser microphones of type 4938. The microphones were attached to a Brüel and Kjær NEXUS signal conditioner. The microphones have been calibrated relative to each other by exposing them to the same sound field [63].

The temperature of the measurement section has been continuously monitored by attaching a thermo-couple to the outside of the waveguide. The acquisition of the measurement signals and the excitation of the loudspeakers were controlled by a HP-VXI system.

5.3 Identified errors

Mechanical vibrations

A error source that is not taken into account in the model description of the acoustic pressures (3.62), are structural vibrations. The measurement setup consists of pipes which act as wave-guides and the microphones and the loudspeakers are attached to these pipes. The whole system is susceptible to mechanical vibrations, which may cause vibrations of the microphone membranes and create a bias error in the measurement results. As the vibrations are dependent on the measurement setup itself, and particularly the mechanical connection between the pipes and how the setup is fixed to the ground, it is difficult to model the
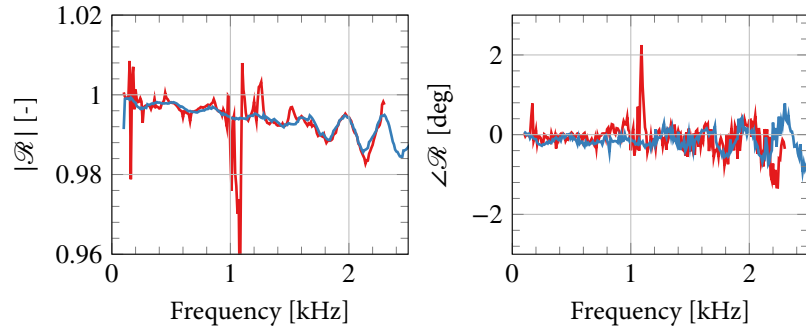
Figure 5.2: *Measured reflection coefficient of the rigid wall for the upstream side. Two cases are shown, the first where the excitation and speaker section are connected (━━) and the second where the two sections are disconnected (━━).*

effects. Therefore, only the relative importance on the measurement results will be shown and discussed but not quantified.

Under a single sine excitation the measured signal will be a superposition of the measured pressure signal and the vibration signal. As both excitations are of the same frequency, the resulting signal will also be a harmonic sine wave. Therefore, the extra linear pathway affecting the measurement results will not unveil itself in for example the coherence, even if the propagation speed is different.

The vibrations induced by the loudspeaker act on the natural resonances of the mechanical system and most often they will appear as sharp peaks in the measurement results. Measurements have been performed to show the effect if the measurement section is rigidly attached to the excitation section. Results of such measurements are shown in figure 5.2. The results show the measured reflection coefficient of the steel wall for the two cases where the measurement section and excitation are connected and disconnected. It can be seen that both phase and magnitude of the reflection coefficient are affected by the vibrations and the measurements are more smooth when the excitation section is disconnected from the measurement section. The influence if of vibrations depend on the actual measurement setup and it is good practice to verify whether there are significant vibrations present.

Temperature influence

To perform accurate measurements, especially for the phase, changes of temperature during the measurement should be taken into account. In the current setup, the temperature is continuously monitored and the average temperature at each excitation is recorded and used in the post processing to determine the speed of sound. As an example, the phase
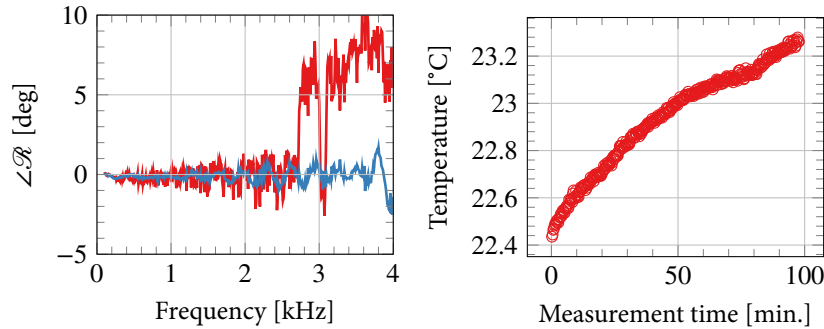
Figure 5.3: *Comparison of the phase of the determined reflection coefficient of the steel wall for the upstream pipe (left) using the averaged measured temperature (——) and the averaged temperature at each frequency (——). The temperature as function of measurement time is shown on the right.*

of the reflection coefficient of the rigid wall is shown in figure 5.3 for two cases, the first case is where the average temperature of the whole measurement is taken and the second case where the average temperature at each measurement frequency is used to perform the calculation.

In the same figure, the temperature as function of measurement time is shown, and it can be seen that during the 1.5 hour measurement, the temperature rises by 0.8 ^oC, which is larger than the uncertainty in the temperature measurement itself (Appendix A.3). The measured phase with the average temperature shows sudden jumps in the measured phase. The excitation frequency is chosen at random and thus the increased error in the phase due to the steadily increase in temperature will be distributed randomly to the frequencies, leading to the jumps in the measured data.

From the figure it can be seen that the phase calculated using the frequency dependent data is smoother and the deviation from 0 degree is smaller. This temperature increase is small, but readily noticeable in the phase of the reflection coefficient.

Finite dimensions of the microphones

In the measurement model, (3.62), the pressure is defined at a single point but the microphones measure a surface averaged pressure. This leads two sources of error, the first is that the microphone positions can only be measured geometrically up to a certain accuracy. The second source of error is that an averaged pressure is measured due to the finite membrane surface.

The first error can be reduced by acoustically determining the microphone positions,

with the help of theoretical models. By measuring the transfer function between two microphones and minimizing the difference between the transfer function obtained from a theoretical model, the microphone distances can be obtained. The method is similar to method used by Katz [64] except that it doesn't use an extra microphone in the rigid wall.

Consider a semi-infinite pipe closed rigidly at one end, $x = 0$, and a sound field in that pipe which consists only of plane waves. Then the pressure field can be decomposed in a wave travelling towards and away from the rigid end. The pressure field as function of the axial coordinate, equation (3.50) with only the contributions of the plane wave mode, can thus be written as,

$$p = p^+ \exp(-ikx) + p^- \exp(ikx), \tag{5.1}$$

where k is the wave number for plane waves in the duct. The ratio between the pressure at position x_i and x_j is given by:

$$\frac{p_i}{p_j} = \frac{\exp(-ikx_i) + \mathscr{R} \exp(ikx_i)}{\exp(-ikx_j) + \mathscr{R} \exp(ikx_j)}. \tag{5.2}$$

where the reflection coefficient is given by $\mathscr{R} = p^-/p^+$. This coefficient should satisfy the imposed boundary condition at $x = 0$ and for a perfect rigid ending $\mathscr{R} \approx 1$.

The microphone positions are found by minimizing the difference between the model of the transfer function, (5.2) and the calibrated measurement data. To obtain correct data, the wave number k is determined by taking into account the effect of viscous and thermal effects at the tube walls and the speed of sound is determined with the model for by Cramer [65]. For each microphone combination, 2 distances are obtained and after averaging these distances, the microphone separations and the distance to the rigid surface are obtained.

A typical result of this procedure is shown in figure 5.4. The figure shows both the magnitude and phase of the determined reflection coefficient with and without the calibration procedure. It can be seen that the optimization procedure affects the measured absolute value of the reflection coefficient slightly. The effect on the phase can be more clearly seen. The calibration minimizes the oscillatory behaviour of the phase caused by the error in microphone separation distance and removes the linear decaying trend due to the error in the distance between the rigid wall and the first microphone. The initial values and optimized values for the microphone distances are given in table 5.1. From the table it can be seen that the differences between the measured and optimized values are within the size of the microphone (6.35 mm in diameter), except for the last microphone. A possible reason for this discrepancy will be hypothesized in the next chapter 6.

One difficulty with the optimization procedure is that optimization variable x_n always appear together with the wave number k. As the wave number involves the speed of sound, it is critical that the speed of sound and the model of the wave numbers are accurately determined as any error in the speed of sound will be taken into account in the determined
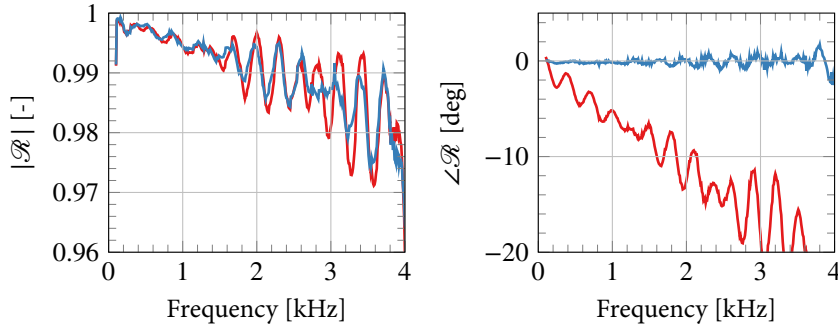
Figure 5.4: *Result of using the measured microphone positions (———) and performing the microphone position calibration (———) on the measured reflection coefficient of the rigid wall.*

Table 5.1: *Measured values, optimized values and uncertainties of the microphone positions.*

		x_1	x_2	x_3	x_4
Measured value	[m]	0.4800	0.5500	0.5850	0.6200
Optimized value	[m]	0.4816	0.5498	0.5847	0.6113
Uncertainty σ	[mm]	0.0862	0.0985	0.1046	0.1440

positions. As shown in the previous section, the measured phase is sensitive to temperature changes. Therefore, when determining the transfer functions the excitation frequency should be chosen at random, otherwise the slow change of the temperature will result in a biased phase and this bias error will affect the determination of the microphone positions.

The described optimization procedure yields the optimized microphone positions, but determine the uncertainty on measurements using an uncertainty analysis, the uncertainty of the optimization microphone positions have to be determined.

The transfer function expression has three variables which have an uncertainty, the wave number k, due to the uncertainty in the speed of sound, and the two microphone positions x_i, x_j which makes it difficult to say something about the uncertainty in the parameter x_i, x_j directly from the optimization procedure described above.

The main source of variance in the wave number is the speed of sound and the wave number can be normalized with respect to the speed of sound to obtain the propagation constant, Γ. The propagation constant can be obtained from the model equation (3.56) To assess the uncertainty in the microphone positions, instead of determining the microphone positions directly, the parameter K_n is determined, which is the microphone position di-

vided by the speed of sound, $K_n = x_n/c$. The equation (5.2) can then be rewritten as,

$$\frac{p_i}{p_j} = \frac{\exp(-i\omega K_i \Gamma) + \mathcal{R} \exp(i\omega K_i \Gamma)}{\exp(-i\omega K_j \Gamma) + \mathcal{R} \exp(i\omega K_j \Gamma)}, \tag{5.3}$$

The parameters K_n are determined using the Matlab optimization algorithm `nonlsq`, which also returns the covariance matrix of the estimated parameters. The microphone positions are given by the relation,

$$x_n = K_n c, \tag{5.4}$$

and the uncertainty on x_n can be determined, using a linear uncertainty analysis, as function of the variance on K_n, obtained from the optimization algorithm, and the variance of the speed of sound c. The variance of the speed of sound can be determined by applying an uncertainty analysis on the model used to determine the speed of sound, which is given by Cramer [65].

In table 5.1 the determined uncertainties are shown. It can be seen that the uncertainty is much smaller than the diameter of the microphones itself (6.35mm) and that the relative uncertainty is around 0.02%.

Microphone dimensions

The second source of error due to finite microphone dimensions is that the signal that is obtained from the microphone is proportional to a surface averaged pressured, introducing an estimation error.

Using a simplified model, the measured pressure by the microphone can be represented by a surface averaged weighted pressure,

$$p(\boldsymbol{x}_0) = \frac{1}{S} \iint_S w(\boldsymbol{x} + \boldsymbol{x}_0) p(\boldsymbol{x} + \boldsymbol{x}_0) dS, \tag{5.5}$$

in which $\boldsymbol{x} = [x, y, z]^T$ denotes the position vector and $\boldsymbol{x}_0$ the position of the center of the microphone in Cartesian coordinates, S the surface of the microphone, p the pressure field and w the sensitivity of each position of the microphone to a pressure acting on that position.

In chapter 3 it is shown that, the pressure contribution of each mode can be written as two waves travelling in the positive and negative axial direction, and the dependence on the

axial direction is given by $\exp\left[\pm i k_l x\right]$.

$$
\begin{aligned}
p_l(\boldsymbol{x}_0) = \quad & p_l^+ e^{-i k_l x_0} \underbrace{\iint_S w(\boldsymbol{x} + \boldsymbol{x}_0)\phi_l(y + y_0, z + z_0) e^{-i k_l x} dS}_{w_l^+} \\
& + p_l^- e^{+i k_l x_0} \underbrace{\iint_S w(\boldsymbol{x} + \boldsymbol{x}_0)\phi_l(y + y_0, z + z_0) e^{+i k_l x} dS}_{w_l^-}.
\end{aligned}
\tag{5.6}
$$

The finite microphone dimensions lead to a corrective factor, w_l^+ and w_l^- to the measured pressure and the actual pressure. These corrective factors are depend on the mode shapes and the wave numbers of the modes.

For plane waves propagating in a fluid without mean flow, the effect of the finite microphone dimensions will cancel itself out during the determination of the scattering matrices. When the microphone dimensions are small and also the imaginary part of the wave number, the acoustic amplitude of the wave can be approximated to be constant over the microphone. The complex exponential consists of a symmetric and anti-symmetric parts and as the microphone is assumed to be symmetric around the center, the anti-symmetric part cancels when performing the surface average and only contribution that is left is that of the symmetric part,

$$
\begin{aligned}
p_l(\boldsymbol{x}_0) = \quad & p_l^+ e^{-i k_1 x_0} \underbrace{\iint_S w(\boldsymbol{x} + \boldsymbol{x}_0)\cos(k_1 x) dS}_{w_1} \\
& + p_1^- e^{+i k_1 x_0} \underbrace{\iint_S w(\boldsymbol{x} + \boldsymbol{x}_0)\cos(k_1 x)\, dS}_{w_1}.
\end{aligned}
\tag{5.7}
$$

The correction factors are now equal for the positive and negative travelling way and when calculating the reflection coefficient, or the scattering matrix using equation (3.57), these correction factors cancel [37, 66].

For the higher order modes, the corrections depend also on the cross sectional dimensions and in general will not cancel, leading to a bias error. Using models of the response of condenser microphones [67, 68], it is possible to determine the weighting factors for each of the modes and account for the error.

5.4   Conclusion

In this chapter, various source of errors that can occur when experimentally determining an impedance using an impedance tube have been investigated. Four error sources have been treated, mechanical vibrations induced by the loudspeakers, the influence of a temperature drift and the finite size of the microphones.

The most prominent error source are vibrations induced by the actuator exciting the sound field, which can lead to large errors in the measured values and appear as sharp peaks in the determined reflection coefficients. These errors can easily be removed by mechanically disconnecting the waveguide where the excitation source is present with the waveguide where the measurement is performed.

The second source that is investigated is the presence of a temperature change during the measurements. This error source predominantly affects the measured phase of the reflection coefficient and can be taken into account by measuring the temperature continuously.

The third error source that is discussed are the finite dimensions of the microphones. Due to the finite size, the acoustic center can only be determined up to a certain accuracy geometrically. Therefore, the microphone positions are determined acoustically leading to improvements of the results especially with respect to the measured phase. Furthermore, due to the finite dimensions, the microphones also measure a surface averaged pressure. In the case of plane waves in a medium without mean flow, this influence leads to a corrective factor to the wave amplitudes, which cancel when calculating the reflection coefficients.

CHAPTER

Errors in impedance tube measurements

In the previous chapter various sources of systematic errors and way to reduce them have been shown. There are still systematic errors present in the measurement of reflection coefficients with an impedance tube and in this chapter the presence is shown using the previous introduced linear uncertainty analyses. The effect of the systematic error on the measured reflection coefficient can be summarized by two trends and in this chapter, various hypotheses of the source of these trends are investigated and the most plausible hypothesis presented.

6.1 Introduction

In the previous chapter, several systematic errors and their influence on the measurement results have been shown. To determine whether there are still systematic errors present in the measurements, an uncertainty analysis has to be performed on the measurement and the results compared with a known value. In chapter 4 the use of the linear uncertainty analysis to determine the stochastic uncertainty in the measurements has been explained. To determine whether there are systematic errors present, the measurement accuracy has to be assessed and the measurement results compared with a calibration standard. As explained in the previous chapter 5, a calibration standard is the reflection coefficient of a rigid wall.

In figure 6.1, the measured reflection coefficient and corresponding uncertainty intervals of the rigid wall are shown. The experimental setup used to obtain the data has been presented in section 5.2. The information on the variance of the measurands is given in table 6.1 and more information to determine the uncertainties can be found in appendix

Table 6.1: *Uncertainty table of the measurement.*

| Variable	Mean Value	Standard deviation	Source
Amb. humidity	25% [RH]	3.23% [RH]	Manufacturer
Amb. pressure	100 [kPa]	1.30 [hPa]	Manufacturer
Amb. temperature	25 [°C]	0.0675 [°C]	Measurement
Pipe diameter	50 [mm]	65.2 [μm]	Manufacturer
Transfer function	-	1% rel. error	Manufacturer
Microphone Position 1	0.4816 [m]	8.62e-2 [mm]	Measurement
Microphone Position 2	0.5498 [m]	0.98e-1 [mm]	Measurement
Microphone Position 3	0.5847 [m]	1.05e-1 [mm]	Measurement
Microphone Position 4	0.6113 [m]	1.44e-1 [mm]	Measurement
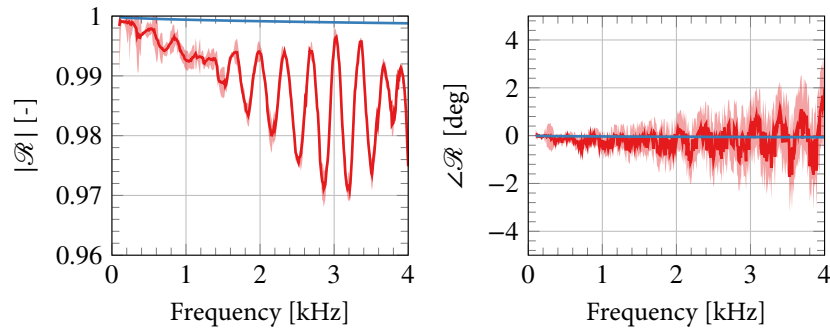
Figure 6.1: *Theoretical reflection coefficient (——), and the measured reflection coefficient (——) with the 95% confidence interval (▬) when taking into account the known systematic errors as function of frequency.*

A.3. In the same figure the theoretical amplitude and phase of the reflection coefficient as function of frequency is given in figure 6.1.

The results show that the distance between the theoretical and measured amplitude of the reflection coefficient is much larger than the range of the 95 % confidence interval and it is likely that there is a systematic component present. On the other hand, for the measured phase, the distance between the measured and theoretical phase is smaller than the uncertainty intervals and no statement can be made whether the observed difference between the model and result is due to a systematic or random error.

These kinds of observations are not unique. Measurements have been performed at the Acoustical Laboratory of the Université du Maine (LAUM) under the supervision of Yvés Auregan and at the German Aerospace center in the institute of Propulsion Technology under the supervision of Friedrich Bake. The observations made in these measurements
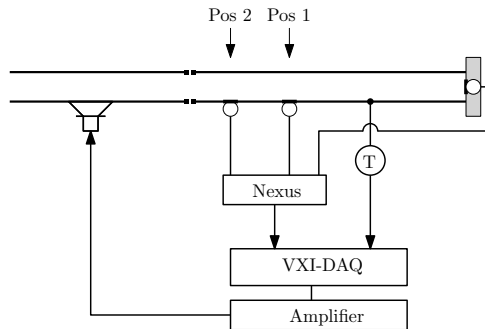
Figure 6.2: *Schematic of the experimental setup used to determine the origin of the oscillations.*

were similar as those presented in figure 6.1, and also in the literature similar results can be found [37, 69, 70].

Two trends can be distinguished from the measured magnitudes of the reflection coefficient, the first trend is a linear decay with increasing frequency, and the second is an oscillating behaviour around the trend line as function of frequency. In this section, these two trends will be discussed and possible explanations investigated.

6.2 Oscillations in the reflection coefficient

The first trend that be discussed is the oscillatory trend in the reflection coefficient. Measurements have been performed where the oscillatory trend on the results are not present, and the schematic of the setup is given in figure 6.2.

The setup is very similar to the one presented in the previous chapter (figure 5.1), however there is a microphone placed in the rigid end to acts as a reference.

Using this setup, it is possible to determine the reflection coefficient from the rigid wall with two independent measurements, by determining the transfer functions not with respect to the excitation signals, but with respect the acoustic signal measured at the rigid wall. In this case, no calibration is needed and the influence of multiple microphones in the duct can be determined. The influence of duct vibrations, excited by the sound field in the duct, is investigated by burying the measurement section in very fine gravel.

Three configurations were measured, and an overview of the measurement configurations is given in table 6.2. For configuration 1, the acoustic pressures are measured at two different positions in two separate measurements and the measurement section was buried. In this case, the cross-influence of the microphones will not be present and the extra loading of the duct by the sand will increase the stiffness of the duct and the damping of the

Table 6.2: *Overview of the different measurement configurations. The symbols $\odot$ and $\oplus$ indicate the two different microphones that are used.*

Configuration	Microphone position		Boundary condition
	Pos 1	Pos 2	
1a	$\odot$		Buried
1b		$\odot$	Buried
2a	$\odot$		Suspended
2b		$\odot$	Suspended
3a	$\odot$	$\oplus$	Suspended
3b	$\oplus$	$\odot$	Suspended

wall vibrations. In configuration 2, the duct is suspended by rubbers. In this case, the mechanical boundary conditions of the measurement section can be considered to be free-free and the damping of the structural waves is only due to the internal losses of the aluminium and sound radiated from the measurement section to the environment. In configuration 3, the duct is also suspended by rubbers, but the acoustic pressure is measured simultaneously at two different positions. The measurement is repeated by switching the microphones. Comparing the measurements results from this configuration, with those obtained from configuration 2, the cross-influence of the presence of the microphones can be assessed.

The microphone positions have been determined using the method as explained in the previous chapter 5.3, but only for the first configuration. For the other configurations, the same calibrated microphone positions are used to be able to exclude errors in the optimization procedure during the comparison of the measurement results.

The measurement results are shown in figure 6.3. The figure shows the measured reflection coefficient as function of frequency for the three cases. For the configuration where the measurement section is buried in sand gives the most smooth measurements, and the effect of the oscillations is almost not present. Comparing this to the measurement results from the second configuration, we see that the absolute value is slightly lower than that of case 1 and the amplitude of the oscillations have increased slightly. For the phase, the oscillations have clearly increased. For the third configuration, the presence of the oscillations can clearly be seen for both the magnitude and the phase. From these observations it can be concluded that the effect of the presence of the microphones and the non-rigidity of the wall pay a role in the observed systematic error.

Comparing the amplitude of the oscillations and the slope of the decay of the absolute value for the measurements presented in this figure (figure 6.3) and those obtained from measurements with multiple microphones (figure 6.1), we see that for the current measure-
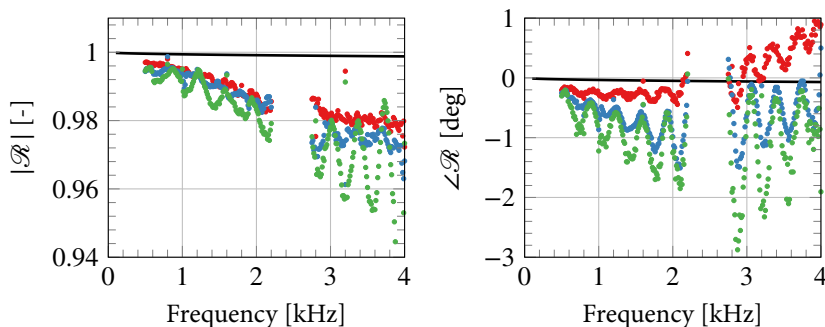
Figure 6.3: *Measured reflection coefficient for the various measurement configurations as shown in table 6.2. Configuration 1, (●); Configuration 2, (●); Configuration 3, (●) and the analytical model (——).*

ments the oscillations are larger and the slope steeper. The increase of the errors can be appreciated by the fact that the presence of the microphone in the rigid wall will lead that the wall becomes more compliant and thus a lowered amplitude of the reflection coefficient. Also, the results from figure 6.1 are obtained using a linear least squares estimate from four microphones, and the effect of the bias error will be distributed.

As shown in the previous chapter, the optimization procedure for the microphone positions obtained values for the last microphone which are larger than the microphone diameter. This behaviour can be appreciated by the effect of the microphones on the measurements, the transfer function between the microphones are derived for the ideal case and the influence of the microphones is not taken into account, leading to a bias error in the estimated acoustic centers.

The influence of the microphones on the sound field will also affect the calibration data. Currently, the microphones are calibrated with respect to each other by placing them flush mounted in a duct, in the same cross sectional plane close to a rigid wall. For frequencies smaller than the first cut-on frequency of the duct, the microphones should measure only the plane wave mode and in theory, they will measure the same frequency. However, as the impedance of the duct wall is not uniform in the circumferential direction, higher order modes will be excited and the measured pressures will also have contribution due to these modes, which may be different for each of the microphones introducing a bias error in the determined calibration factors.

Measurements, similar to that of configuration 2 and configuration 3 have been performed in the setup at the DLR, however in these circumstances the differences in the measurements are negligible. In that case, the influence of the microphone impedances seems
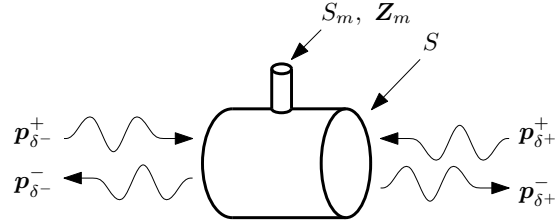
Figure 6.4: *Schematic drawing of the microphone as a three port model.*

implausible and the resulting error is most probably due to the compliance of the waveguide.

For the measurements performed in Le Mans, there were also oscillations present on the measurement data. That setup is made of thick walled steel (1cm) and has a smaller radius of the duct (15mm). The mass of the setup is much larger and it is stiffer, compared to the setup at the KTH and the influence of the pipe vibrations will be comparatively smaller. Therefore, the observed error is most probably only induced by the presence of the microphones.

In conclusion, it is plausible that the oscillations on the measurements are caused by the influence of the microphones on the measurements and the compliance of the waveguides. These effects are highly dependent on the actual measurement configuration and the way how the microphones are mounted in the duct.

Microphone impedance

It is shown that the presence of the microphones introduces a bias error which introduce oscillations in the measured reflection coefficients. The influence on the wave propagation can be modelled using a lumped parameter model. The wavelengths of the acoustic waves are much longer than the diameters of the microphones and thus the pressure difference across the microphone can be regarded as negligible. Therefore, the microphone mounting can be seen as a continuous pressure junction where the microphone can be seen as a side junction with a certain impedance Z_m. In figure 6.4, a schematic of the idea is given.

Two equations describe the junction, the first is that the pressure at each junction should be the same following from the continuity of pressure and the second is that the acoustic volume flux is constant:

$$p_{\delta-} = p_{\delta+} = p_m, \tag{6.1}$$

where $p_{\delta-}$ is the pressure just before the junction, $p_{\delta+}$ the pressure just behind the junction and p_m the pressure at the microphone. The volume flux is given by

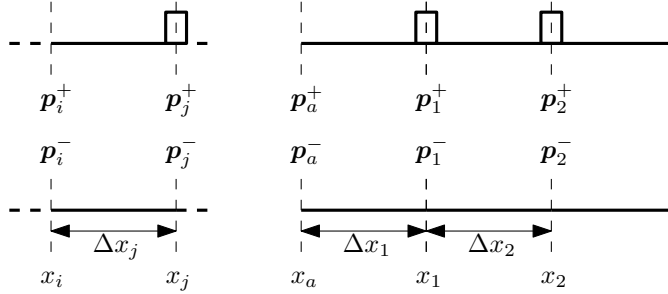$$Su_{\delta-} + Su_{\delta+} + S_m u_m = 0. \tag{6.2}$$

Figure 6.5: *Schematic of the microphone scattering matrix model and the combination of two elements.*

where $u_{\delta-}$ is the acoustic particle velocity just before the junction, $u_{\delta+}$ the acoustic particle velocity just behind the junction, u_m the velocity of the microphone membrane, S the cross sectional area of the waveguide and S_m the cross sectional area of the microphones. The relation between p_m and u_m is given by the microphone impedance $Z_m = p_m/u_m$. To estimate the influence of the microphone on the measurement, the scattering transfer matrix T_s is determined. The scattering transfer matrix relates the two travelling wave components at each side of the junction in comparison with the scattering matrix which relates the waves travelling to the junction with the waves travelling away from the junction. The pressure p and velocity u can be decomposed in the travelling wave components by

$$p = p^+ + p^-, \tag{6.3}$$

and

$$u = \frac{1}{\rho c} \left(p^+ - p^- \right), \tag{6.4}$$

where ρ is the density and c the speed of sound. Using the microphone impedance, the scattering transfer matrix of the microphone section can then be determined,

$$\begin{bmatrix} p_{\delta-}^+ \\ p_{\delta-}^- \end{bmatrix} = \begin{bmatrix} -\frac{1}{2}\frac{\rho c_0 S_m}{S^2 Z_m} & 1 - \frac{1}{2}\frac{\rho c_0 S_m}{S^2 Z_m} \\ 1 + \frac{1}{2}\frac{\rho c_0 S_m}{S^2 Z_m} & \frac{1}{2}\frac{\rho c_0 S_m}{S^2 Z_m} \end{bmatrix} \begin{bmatrix} p_{\delta+}^+ \\ p_{\delta+}^- \end{bmatrix}. \tag{6.5}$$

From the equation it can be seen that the influence of the microphone itself scales with S^{-2} and thus the effect becomes more noticeable for smaller pipes (assuming that the microphone cross section remains constant).

The second step is to relate the travelling wave components at a certain distance Δx_j from the microphone and those at the microphone. A schematic of the situation is given in

figure 6.5. It is found by matrix multiplication and is given by,

$$
\begin{bmatrix}
\left[1 - \frac{1}{2}\frac{\rho c_0 S_m}{S^2 Z_m}\right] e^{ik\Delta x_j} & -\frac{1}{2}\frac{\rho c_0 S_m}{S^2 Z_m} e^{-ik\Delta x_j} \\
\frac{1}{2}\frac{\rho c_0 S_m}{S^2 Z_m} e^{ik\Delta x_j} & \left[1 + \frac{1}{2}\frac{\rho c_0 S_m}{S^2 Z_m}\right] e^{-ik\Delta x_j}
\end{bmatrix}
\begin{bmatrix} p_i^+ \\ p_i^- \end{bmatrix}
=
\begin{bmatrix} p_j^+ \\ p_j^- \end{bmatrix}.
\tag{6.6}
$$

The pressure at the microphone position is given by $p_j^+ + p_j^-$ and the pressure at the microphone is only a function of the impedance at a distance Δx_j because the pressure at side 1 and 2 of the junction should be equal.

The pressure at a second microphone can be related to the impedance at the measuring cross section x_a, by multiplying two scattering transfer matrix elements (Fig. 6.5). As the relation between the travelling wave components is known at each microphone as function of the impedance, the wave decomposition method can be performed with the inclusion of the microphone impedance. For the two microphone case, the pressure at two microphones is then given as:

$$
\begin{aligned}
p_1 = p_1^+ + p_1^- &= \left[A_1^{11} + A_1^{21}\right] p_a^+ + \left[A_1^{12} + A_1^{22}\right] p_a^-, \\
p_2 = p_1^+ + p_1^- &= \left[B_1^{11} + B_1^{21}\right] p_a^+ + \left[B_1^{12} + B_1^{22}\right] p_a^-,
\end{aligned}
\tag{6.7}
$$

in which A is the matrix relating the pressures at x_a to the pressures at x_1 and matrix B the result of the multiplication of two scattering transfer matrix elements and relates the pressures at x_a and x_2. The superscripts ^{ij} denote the specific element of that matrix.

The expressions for p_1 and p_2 are given by:

$$
\begin{aligned}
p_1 =\, & p_a^+ e^{ik\Delta x_1} + \\
& p_a^- e^{-ik\Delta x_1}, \\
p_2 =\, & p_a^+ \left[e^{ik\Delta x_1 + ik\Delta x_2} + \frac{1}{2}\frac{\rho c_0 S_1}{S^2 Z_1} e^{-ik\Delta x_1}\left(e^{-ik\Delta x_1} - e^{ik\Delta x_2}\right)\right] + \\
& p_a^- \left[e^{-ik\Delta x_1 - ik\Delta x_2} + \frac{1}{2}\frac{\rho c_0 S_1}{S^2 Z_1} e^{-ik\Delta x_1}\left(e^{-ik\Delta x_1} - e^{ik\Delta x_2}\right)\right].
\end{aligned}
\tag{6.8}
$$

Also in the two microphone case, the pressure at the second microphone is only dependent on the influence of the first microphone, the distance to the first microphone and the distance between the first microphone and the measuring cross section.

Under special circumstances, the extra terms related to the microphone impedance can become zero. Rearranging the second equation gives rise to,

$$
\begin{aligned}
p_2 =\, & p_a^+ \left[e^{ik\Delta x_1 + ik\Delta x_2} + \frac{1}{2}\frac{\rho c_0 S_1}{S^2 Z_1} e^{-ik\Delta x_1}\left(e^{-ik\Delta x_1} - e^{ik\Delta x_2}\right)\right] + \\
& p_a^- \left[e^{-ik\Delta x_1 - ik\Delta x_2} + \frac{1}{2}\frac{\rho c_0 S_1}{S^2 Z_1} e^{-ik\Delta x_1}\left(e^{-ik\Delta x_1} - e^{ik\Delta x_2}\right)\right].
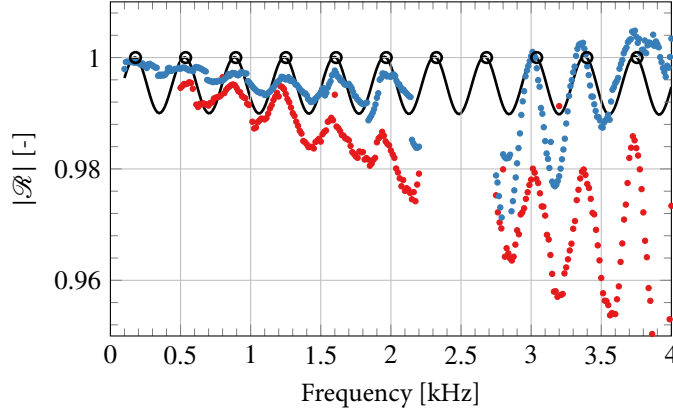\end{aligned}
\tag{6.9}
$$

Figure 6.6: *Comparison between the analytical model of the microphone impedance (——) and the measurement results from two setups: setup 1, (●, figure 5.1), setup 2, (●, figure 6.2). The (○) denote the frequencies where there is no influence of the microphone impedance on the measurements, e.g. ($\cos(k\Delta x_1) = 0$. The used microphone impedance for the model has been set to $\rho c_0 S_m/2S^2 Z_m = 5 \cdot 10^{-3}(1 + 5i)$.*

It shows that when $\sin(kx_2) = n\pi$, $n \subset 0, 1, 2, ...$ the extra terms related to the microphone impedance vanish. Unfortunately this is also the moment at which the two rows in the wave decomposition become dependent and there is no solution to wave decomposition method (3.62). However, there is another special circumstance, which arises when measuring a surface whose reflection coefficient is equal to 1, i.e. $p_a^+ = p_a^-$, then the above relation can be rewritten as,

$$p_2 = p_a^+ \left[\; e^{ik\Delta x_1 + ik\Delta x_2} + e^{-ik\Delta x_1 - ik\Delta x_2} + \right.$$
$$\left. \frac{1}{2} \frac{\rho c_0 S_1}{S^2 Z_1} \left(e^{-ik\Delta x_1} + e^{ik\Delta x_1} \right) \left(e^{-ik\Delta x_2} - e^{ik\Delta x_2} \right) \right], \tag{6.10}$$

showing that the influence of the microphone vanishes when $\sin(k\Delta x_2) = n\pi$, $n \subset 0, 1, 2, ...$ and $\cos(k\Delta x_1) = \frac{1}{2}n\pi$, $n \subset 0, 1, 2, ...$

In figure 6.6 the results of the measurements of the rigid wall on the upstream side are shown. The data is the same as from the figure of 6.1, however now only the first two microphones have been used to calculate the reflection coefficient of the wall. Also, the measurement results obtained from the experimental setup depicted in figure 6.2 with the third configuration are shown. In the figure, the analytical model, for which the microphone impedance is modelled as a complex constant, is plotted. Furthermore, the positions where $\cos(k\Delta x_1) = 0$ are denoted by circles.

It can be seen that the oscillatory behaviour present in the measurements is reproduced by the analytical model and that the peaks of the analytical model coincide with those from the measurements. It should be noted that the exact positions of the peaks have a dependence on the imaginary part of the microphone impedance, and that the positions of the peaks do not exactly coincide with the positions where $\cos(k\Delta x_1) = 0$. The amplitude of the oscillation in the analytical model is governed by the real part of the microphone impedance which shows the amount of acoustic energy dissipated by the microphone. The imaginary part has a strong influence of the phase of the reflection coefficient (not shown in the figure).

Efforts have been made to directly determine the microphone impedance from measurements in the setup at the KTH. It proved impossible to obtain reliable and convincing data for the microphone impedance itself. There are several possible explanations for the difficulties in determining the microphone impedance. For the lower frequencies, the magnitude of the induced error is similar to the error induced by the second systematic error, the apparent absorption (discussed in the next section). When measuring the impedance of the reflection coefficient using two microphones, they have to be calibrated relative to each other, however with the current method to calibrate the microphones, the calibration itself is affected by the influence of the microphones on the measurement. On the other hand, with the setup as shown in figure 6.2, the reflection coefficient of the rigid wall is no longer equal to the theoretical results and the extra compliance induced by the microphone placed in the rigid wall introduces an error which is similar in magnitude as the error induced by the presence of the microphones in the waveguide.

6.3 Apparent absorption

The second trend that will be discussed is the linear decay of the measured reflection coefficient with increasing frequency, leading to an apparent absorption. It is interesting to note that in the first half of the previous century, there was a large controversy whether the wall losses that were predicted by the model by Kirchhoff [23] were correct. Many workers measured a 10-15% larger increase of the absorption than predicted by the model [66, 71–73]. Kirchhoff has derived the results in 1868 [23] and it has been thoroughly scrutinized to find an explanation to the extra absorption[74, 75]. It has been shown that the assumptions made in the model should all be correct and the large measured difference cannot be explained by a violation of the assumptions made in the model. Three decades later, researchers reported experimental results that the losses, induced by the walls and predicted by Kirchhoff, are in agreement with the model [16, 76, 77].

First the presence of the apparent absorption will be shown using the measurement data

that has been obtained from several setups. The setup used to perform the measurements at the KTH has been described in 5.2. The second setup is an experimental setup present in the LAUM. It consists of circular ducts made of steel with an inner radius of 15mm and a wall thickness of 5mm and is similar to the setup used in [78] The third setup is found in the DLR Berlin. The wave guide is rectangular with an inner dimension of 60x80mm, made from aluminium and has a wall thickness of 10mm. More information can be found in [25, 59].

To be able to determine the magnitude of the apparent absorption, it is assumed that the reflection coefficient of the rigid wall can be correctly described with the analytical models. The fluid is considered to have a finite viscosity and thermal conductivity, and an acoustic wave incident on the rigid wall will also excite the entropy and vorticity mode (section 3.2). Assuming that the temperature perturbations, induced by the acoustic wave, of the rigid wall are zero and that the velocity of the rigid wall is zero, the reflection coefficient can be derived. The impedance of the rigid wall is given by [13],

$$\frac{1}{Z} = \frac{e^{-i\pi/4}}{\rho c} \left(\frac{\omega \mu}{\rho c^2} \right)^{\frac{1}{2}} \frac{\gamma - 1}{\sqrt{\mathrm{Pr}}}, \tag{6.11}$$

where ρ is the density of the air, μ the dynamic viscosity, γ the heat capacity ratio, Pr the Prandtl number, c the speed of sound and ω the angular frequency. Consequently, the reflection coefficient at the wall can be calculated using,

$$\mathscr{R} = \frac{Z - \rho c}{Z + \rho c}. \tag{6.12}$$

The apparent absorption coefficient can be calculated by measuring the acoustic reflection coefficient at the position of the first microphone ($x_1 = 0$ in equation (3.62)). The ratio between the reflection coefficient at the rigid wall and the measured reflection coefficient at the first position is given by,

$$\frac{\mathscr{R}(x_1)}{\mathscr{R}(x_w)} = e^{2ik(x_1 - x_w)}. \tag{6.13}$$

The wave number k consists of a real and imaginary part and the imaginary part, $\alpha = \mathfrak{I}(k)$ is the absorption coefficient per unit length. The imaginary part of the wave number is the absorption per unit length and can then be determined with,

$$\alpha = \frac{1}{2(x_1 - x_w)} \ln\left| \frac{\mathscr{R}(x_1)}{\mathscr{R}(x_w)} \right|. \tag{6.14}$$

To put the experimentally determined absorption in perspective, it is compared against the first order wall losses obtained by Kirchhoff, equation (3.56).
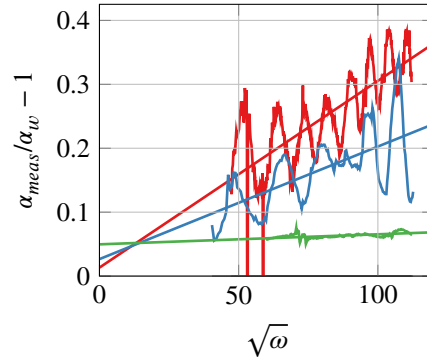
Figure 6.7: *Measured absorption coefficient α_{meas} relative to the theoretical wall losses α_w as function of frequency for the measurement setup at the KTH (——), LAUM (——) and the DLR (——). Also, the linear regression is shown.*

In figure 6.7, the measured absorption coefficient per unit length relative to the theoretical wall losses are shown as function of the square root of the angular frequency for the three different setups. For all the measurements, it can be seen that the effective absorption is higher and it depends on the setup and frequency how large the deviation is. The deviation itself is in the order of 5-30 % of the wall losses. By plotting the effective absorption as function of the square root of the frequency, a linear trend can be seen which comes close to the origin when the frequency goes to zero. As the wall losses are also proportional to the square root of the frequency, the deviation seems to be a factor that is linearly proportional to the frequency, which also has been observed by Fay [66].

The next part of the section is the discussion of several possible explanations of the observed apparent losses. The first explanation that will be discussed are the volumetric losses, caused by inter-molecular relaxation effects. The second hypothesis is based on the Konstantinov effect, which is present when an acoustic wave interacts is scattered at a fluid-fluid boundary. The third effect that will be discussed is the cross sectional dependency of the acoustic field close to the rigid wall. These hypotheses do not give a satisfactory answer to the observed absorption and the last part is dedicated to a literature survey to determine whether there is any correlation between the measured absorption and the used experimental setups.

Volumetric losses

The first error that comes to mind is the exclusion of the volumetric losses. The volumetric losses are induced by the bulk viscosity (chapter 3) and the moleculare relaxation effects.

The relaxation effects are induced by the finite time for a volume of gas to adjust to changes. If the induced changes are too fast compared to the relaxation times of the intermolecular interactions, the volume of gas does not reach a state of equilibrium and lead to losses. These effects can be taken into account in the complex wave number [13, 79] and the constants in the model are derived from experimental data [80–83].

In figure 6.8, the contour plot of the ratio of the volumetric losses to the wall losses is given as function of the Helmholtz number and shear wave number. The Helmholtz number in this figure is defined as,

$$\text{He} = \frac{\omega}{c_0} \frac{1}{2} D_h, \tag{6.15}$$

where the characteristic dimensions is given by half of the hydraulic diameter D_h which for a circular duct reduces to the radius and the shear wave number is defined by,

$$\text{Sh} = \frac{1}{2} D_h \sqrt{\frac{\rho_0 \omega}{\mu}}, \tag{6.16}$$

The shear wave number gives the relative importance of the wall losses versus the volumetric losses. For larger ducts, the volumetric losses will be more important and for smaller ducts, the wall losses will dominate the total losses.

The parameter area that is covered with the measurements at the KTH, DLR and LAUM are indicated with squares in the figure. Comparing the relative contribution of the volumetric losses to the wall losses with the deviation from the wall losses in figure 6.7, it can be seen that the contribution of the volumetric losses are much smaller than the apparent deviation. This contradicts the hypothesis of a significant contribution of the volumetric losses to the observed apparent absorption.

Konstantinov effect

Legusha proposed an explanation based on the Konstantinov effect [84, 85]. The Konstantinov effect is the influence of the acoustic boundary layers on the acoustic fields, when a plane harmonic wave impinges on the boundary between two materials [86].

Legusha derives the relationships between the acoustic fields in a viscous fluid at a gas-gas interface and the acoustic reflection and transmission coefficients are obtained as function of ratios of the physical parameters of the gasses. As the relations are dependent on the ratios of the fluid parameters, Legusha argues that by taking appropriate limits, the gas-gas boundary can be modelled as a gas-solid boundary.

The obtained absorption coefficient for a wave incident on the surface is not a monotonic increasing function of frequency, but shows a distinct maximum. Legusha argues that the presence of this maximum is the reason of the observed extra absorption in literature,
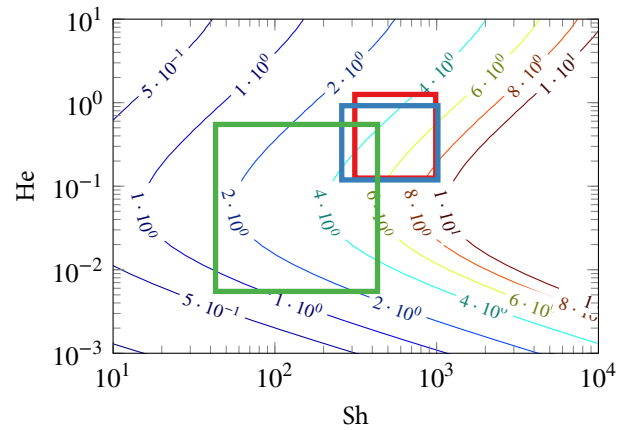
Figure 6.8: *Contour plot of the ratio of the volumetric losses [%] and the wall losses as function of Helmholtz number and shear wave number. The rectangle indicates the parameter area that is covered with the measurements performed at the KTH (━━), LAUM (━━) and DLR (━━).*

as the value of the absorption coefficient at this maximum is around 10% larger than the absorption coefficient predicted by Kirchhoff.

Analytical efforts have been made to reproduce these findings, by assuming a gas-solid interface where the heat conduction in the solid is governed by a Fourier's law and the solid assumed to be motionless. The results show that the influence of the thermal boundary layer in the solid can be neglected when the product of the thermal capacity and the thermal conductivity of the wall is much larger than that of the gas, in accordance with other findings [13, Chapter 10.3].

A possible explanation of the different results, is the derivation of the results. Legusha assumes a gas-gas boundary and consequently a constitutive relation for a gas has to be used, creating a relation between the pressure and temperature for both gasses. By deriving the relations between the impinging, reflected and transmitted waves and taking the appropriate limits of these relations to resemble a gas-solid boundary, the obtained relationships incorrectly describe a relation between the pressure and temperature for the solid.

Edge effect

An effect that is not taken into account when determining the impedance of the wall is the three dimensional nature of the acoustic field close to the rigid wall. The acoustic pressure fields are assumed independent of the axial direction in the impedance tube, however at the
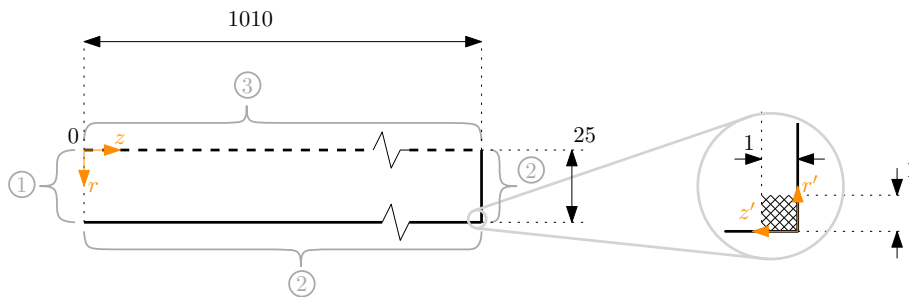
Figure 6.9: *Schematic of the numerical model. The dimensions are in mm, and the hashed surface indicates a refined mesh compared to the overall mesh. The boundary conditions (in grey) are given by: 1. Prescribed velocity, 2. Iso-thermal wall and no-slip, 3. Periodic boundary.*

rigid wall this is no longer true as in the region where the acoustic wave guide connects to the rigid wall, the acoustic boundary layers of the waveguide and rigid wall merge. This region is not taken into account when determining the reflection coefficient and could influence the measured reflection coefficient. This influence of the region is investigated by simulating the impedance tube with a finite element method and taking into account the presence of the acoustic boundary layer. Both a 1-D model and a 2-D model have been simulated and the results are compared with the analytical expressions for the reflection coefficient of a rigid wall [13]. For the 1-D model, there is no influence of the boundary layers at the side walls and the results can be verified against the analytical models.

In figure 6.9 the numerical domain is shown. The waveguide is modelled as axisymmetric duct with an inner radius of 25mm and a length of 1010mm, similar to the acoustic waveguide used in the experiments of chapter 5. The walls of the ducts are modelled to be rigid and isothermal.

The linearised Navier-Stokes equations in the frequency domain are used to model the acoustic wave propagation in the duct. For the velocity and temperature, second order elements were used and for the pressure linear elements for the pressure where used. The numerical model was solved with a direct linear solver.

Close to the boundaries, the mesh is refined to be able to resolve the acoustic boundary layers accurately. The thickness of these layers is in the order of 100 μm, as shown in section 3.2. Far away from the rigid wall, it was ensured that the acoustic boundary layer was discretized by at least 20 points in the radial direction and the axial spacing was such that a wavelength was discretized by at least 10 points. The region were the boundary layers meet, the mesh was refined even more both in the axial and radial direction close to the rigid wall. The region was within a distance of 1mm of both side walls, as shown in figure 6.9.
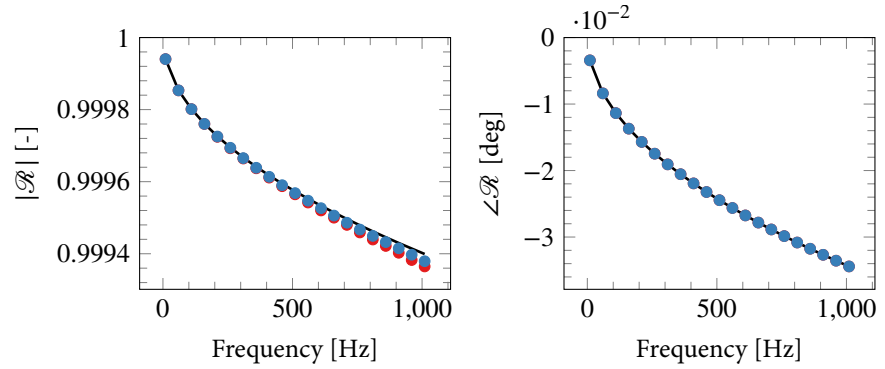
Figure 6.10: *Comparison between the analytical model for the reflection coefficient of a rigid wall (——) and results from the one dimensional numerical solution for two different mesh sizes, with an axial spacing of 0.1mm (●) and a spacing of 0.01mm (●).*

As the wave is propagating in a viscous medium and the wave propagation is not adiabatic, the dispersion relation is not equal to $k = \omega/c$. For the 1-D simulations, there is no influence of the walls and the dispersion relation can be obtained using the linearised mass conservation equation (3.8), linearised Navier-Stokes equation (3.9) and the linearised Fourier-Kirchhoff energy equation (3.10).

For the two dimensional case, the influence of the boundary layers at the pipe wall affect the wave propagation and the dispersion relation obtained by Bruneau [87] is used to determine the wave numbers. The reflection coefficient of the rigid wall from the numerical simulations has been determined with the wave decomposition method (3.62) and two pressures sampled at the positions $x_1 = 0.51$m and $x_1 = 0.56$m.

In figure 6.10 the results are shown from the 1-D simulations for two numerical models with different mesh-sizes, one with an axial spacing of 0.1mm and 0.01mm in the complete domain, except for the boundary layers at the wall and in the area where the mesh is refined. The same figure also shows both the absolute value and the phase of the reflection coefficient from the analytical model (6.11). It can be seen that there is a good agreement between the analytical model and the numerical models. The relative difference in absolute value is in the order of 0.001% and the difference in phase is in the order of 10^{-6} degree. The difference between the two simulations do not differ much, indicating that the results will not significantly change when reducing the mesh size even more.

In figure 6.11 the results of the determined reflection coefficient of the wall for the 2D simulations are shown together with the analytically model for the one dimensional model. Again two different mesh sizes have been used for the axial spacing, the first with a spacing
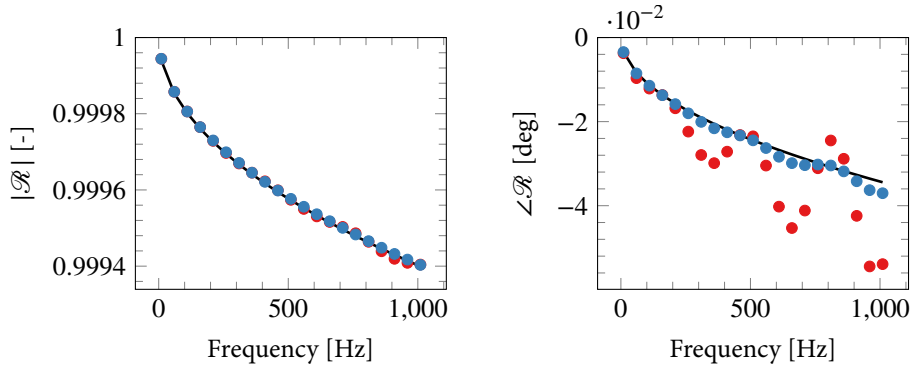
Figure 6.11: *Comparison between the analytical model for the wall impedance of a rigid wall (——) and results from the numerical calculation for the two dimensional case for two different mesh sizes, an axial spacing of 1mm (●) and 0.1mm (●).*
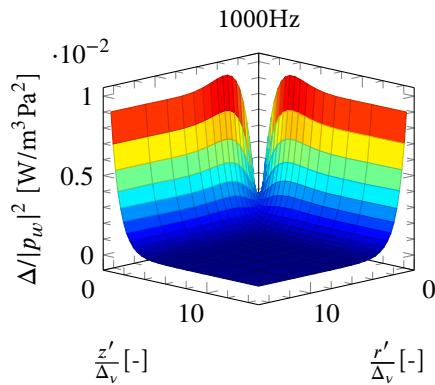

Figure 6.12: *Normalized total acoustic power dissipation in the region close to the rigid wall at a 1000Hz, using the alternative coordinate system $[r', z']$ as shown in figure 6.9. Plotted for $r'/\Delta_\nu \in [0, 15]$ and $z'/\Delta_\nu \in [0, 15]$.*

of 1mm and the second with a spacing of 0.1mm and the difference between the two results is small. The two calculations give similar results for the absolute values, however the phase shows a larger spread in the values for the coarse mesh. This spread is caused by numerically dispersion. Simulations with an increased element order and the same axial spacing didn't show the oscillatory behaviour. The good correspondence between the one dimensional analytical model and the 2D calculations shows that the edge effect does not significantly change the measured reflection coefficient.

Even though that the results for the 2D agree well with the 1D theory, it is interesting to see what the effect is of the edge effect. To investigate the effect, the acoustic power dissipation due to viscous and thermal effects have been plotted in the region close the rigid wall. The total acoustic power dissipation, normalized with the square of the wall pressure, is shown in figure 6.12 for a frequency of 1000 Hz. The data is shown using the alternative coordinate system $[r', z']$ as indicated in figure 6.9 and the coordinates have been normalized with the acoustic boundary layer thickness Δ_v, (3.45).

In the area relative far away from the edge, but on the wall or side wall, the determined acoustic dissipation is equal to that induced by the boundary layers, without any extra effects. When moving closer the corner, from both directions $[z \rightarrow 0\text{mm}, r = 25\text{mm}]$ and $[r \rightarrow 25\text{mm}, z = 0\text{mm}]$ the dissipation increases slightly and decreases to zero in the corner where the side wall and wall meet. The small increase in dissipation is counteracted by the decrease in absorption in the corner and in the corner where the pipe wall and the rigid wall meet, the acoustic dissipation vanishes.

As the absorption at the side wall goes to zero at the corner, the losses are slightly less and the true reflection coefficient will be higher. Also, when decomposing the sound field, the wall losses at the pipe walls are assumed to be constant up to the side walls, and the losses are slightly overestimated. Therefore, the measured reflection coefficient will slightly higher than what it truly is. These both effects make that the influence of the edge effect create an increase of the measured reflection coefficient, compared to the value obtained from the analytical model.

In conclusion, there is an effect of the edge of the wall on the acoustic power dissipation, however the influence on the measured reflection coefficient is very small and can be safely neglected.

Literature survey

In the previous sections, possible hypotheses of the observed increased acoustic absorption have been discussed and it was shown that they could not explain the phenomena. The extra absorption has been reported by other researchers and in this section a literature survey of the experimental results will be given to possibly identify parameters that are correlated with the observed apparent absorption. The next part will discuss the literature, the used gas in the cited literatures is always air at normal temperature and pressure, 20°, and absolute pressure of 1 atmosphere, unless otherwise noted.

Fay measured the acoustic absorption of ducts using a setup similar to a Kundt's tube [66]. In the setup, a microphone is fixed in the side wall of the duct and a second microphone is used to terminate the tube. By moving the second microphone and measuring the resulting sound field at the first microphone, the damping of the duct is determined. He de-

Table 6.3: *Overview of the literature. For the blank table entries, the information is not available.*

Reference	Year	Error [%]	Frequency [kHz]	Radius [mm]	Material	Sh	He
Mason	1928	1.5-15	0.20-4.00 0.20-4.00 0.20-4.00 0.20-4.00	8.51 6.87 5.25 3.70	Brass Brass Brass Brass	34-347	0.01-0.62
Waetzmann	1939	10-15	0.17-2.05 0.17-2.05 0.15-2.30	3.00 5.50 9.50	Brass Brass Steel	25-293	0.01-0.40
Fay	1939	7-16	0.90-4.90	9.52		184-429	0.16-0.85
Beranek	1940	15	0.40-1.20 0.40-2.00	38.10 15.88	Steel Steel	204-850	0.12-0.84
Weston	1953	3	10.07 10.07 19.57 19.57 19.57	0.20 1.00 1.00 0.40 1.00	Glass Glass Glass Monel Monel	13-90	0.04-0.36
Fritsche	1960	2.4	1-1000	45	Brass		
Roesler	1966	1	1-1000	34.96			
Ahrens	1971		0.3-2	27.5-63		300-700	0.15-2.3
Yazaki	2007			0.6-2	Copper	0.1-15	
KTH	2016	5-20	0.2 - 4	25	Aluminium	250-1000	0.12-12
LAUM	2016	5	0.02-2	15	Steel	40-430	0.005 - 0.55
DLR	2016	15-35	0.2-2		Aluminium	300-980[1]	0.11 - 1.83 [1]

[1] Calculated using equation (6.15) and (6.16).

termined the damping for a brass tube with a radius of 9.51mm, and the tube was packed in sand to prevent vibrations of the tube wall. Fay shows that the measured damping consists of two parts,

$$\alpha = A\sqrt{f} + Bf \quad A = 2.92 \cdot 10^{-5}\,[\text{Hz}^{-1/2}\text{cm}^{-1}] \quad B = 6.75 \cdot 10^{-5}\,[\text{Hz}^{-1}\text{cm}^{-1}], \quad (6.17)$$

the first part proportional to the square root of the frequency and identified as the damping predicted by Kirchhoff. The measured value, A, is 0.6% off from the value predicted by Kirchhoff's theory. The size of systematic error, due to the linear part can be estimated to be 7%-16%

Fay also performed the analysis on measurement data obtained by Mason a decade earlier. Mason determined the attenuation of four different straight brass tubes straight tubes by determining the acoustic resistances of the tubes with an acoustic impedance bridge [71]. The tubes had radii of 0.851cm, 0.687cm, 0.525cm and 0.370cm, with corresponding lengths of 6.22m, 4.885m, 4.26m and 7.634m. Mason observes that the measured attenuations are in good agreement with the Helmholtz-Kirchhoff law, within the experimental error of 5% but does not quantify the measurement error. Fay determines from the experimental data by Mason the constants of equation (6.17) and concludes that the contribution of the linear part is in the range of 1.5%-15% of the measured absorption coefficient.

Waetzmann and Wenke investigated the acoustic absorption of ducts made of various materials, such as brass, steel, cardboard and wood [72]. The sound field in the ducts was created using a thermophone and one end and the resulting pressure at the other end was measured. The absorption was measured by determining two resonance lengths of the pipes and quotient of the corresponding pressures at the ends. Waetzmann and Wenke determined the absorption coefficient for brass and steel pipes. The pipes had an inside diameter of 6mm, 11mm and 19mm. They found that the absorption coefficient as around 10-15% higher than that predicted by Kirchhoff's theory. Measurements were also performed on glass tubes, which showed a larger absorption compared to the metal tubes and they investigated in a simplified manner the influence of wall roughness, by creating a glue layer of 2mm thick in a metal waveguide. After drying, the glue formed cracks and the measured absorption coefficient increased three-fold.

Beranek investigates a new method to determine the acoustic impedances using a resonance tube [73]. The resonance tube is made from steel, has a wall thickness of 6.35mm and a radius of 38.1mm. He determines the absorption coefficient of the resonance tube itself and measures an absorption coefficient that is 15% higher than the losses predicted by Kirchhoff. He hypothesized that the difference is due the radiation from the side walls to the environment and the acoustic dissipation in the pores of the tube walls.

Weston discusses the attenuation in "wide ducts [75] and uses an acoustic interferometer to determine the acoustic absorption [76]. The used tubes where made of Veridia with a

precision bore, with a radius precise up to 5μm. The absorption was measured at 10kHz and 20kHz and are in good agreement with Kirchhoff's formulae. The measured absorption for air is within 3% of the theoretical model. Weston mentions that large deviations between the theoretical and experimental results could be traced back to tube imperfections. Weston also mentions the tube walls as a source of error, "*an imperfect wall surface is a frequent cause of experimental disagreement with Kirchhoff's formulae*" [75] and "*it is possible in most previous experimental work to ascribe any real excess tube effect to one or more factors in the list, in particular wall roughness*" [76].

Fritsche uses a cylindrical resonator to determine the acoustic absorption [88] of various pure gasses. He derives correction factors for the resonator to take into account the effect of the acoustic driver on the measurement [16] The brass resonator has an internal radius of 45.000mm and a height of 94.97mm and the surfaces have been honed, however no quantitative measure of the surface roughness has been given. With the resonator, the absorption for a variety of gasses is measured between 1kHz and 1MHz and the measured coefficients agree with the theoretical values within the conservative experimental accuracy of 2.4%.

The work of Fritsche has been extended by Roesler [77], where the absorption of gasses at elevated pressures have been measured. The cylindrical acoustic resonator has an inner radius of 34.96mm and a height of 297.888mm, the inner side walls have been honed and have a surface roughness of ± 2 μm. Roesler observes excellent agreement between the theory and experiments and the deviations are under 1%.

Ahrens and Ronneberger investigated the influence of wall roughness on the acoustic damping due to turbulence [28]. The measured the acoustic damping of a circular waveguide with radii of 27.5mm, 37.5mm and 63mm. The damping is determining by measuring the acoustic sound pressure along the axial direction of the ducts using a traversing microphone in a frequency range of 300-2000Hz.

Several wall roughnesses were created by glueing sandpaper of different grains to the inner walls of the duct. Ahrens and Ronneberger show that the measured damping coefficient for the untreated ducts is larger than those predicted by Kirchhoff theory, and also observe that this extra absorption seems to be independent of the mean flow speed. The measurements for the treated ducts without flow (with an average grain size of 242 μm), show an increase of the acoustic damping by around 50% compared to the untreated duct. No statements are made on the accuracy of the measurement data.

Yazaki et al. determined the acoustic wave numbers for a wide range of conditions using a travelling wave method [89]. An acoustic pulse was created and led through a thick walled copper tube. Several tubes, with radii of 0.6mm, 1.0mm and 2.0mm where used to cover a large range of shear wave numbers. The tubes where long enough (40m-55m) such that

the travelling pulse is completely attenuated before it reaches the other side of the duct. The pulse has been measured by transducers mounted in the side walls of the duct, with a spacing of 1.51m. The authors mention that the presence of the periodic array of microphones, undesirable Bloch wave-type dispersion was presented and it was removed by filling the dead volumes of the microphones with viscous silicon oil. Good agreement for a wide range of shear wave numbers is obtained, verifying the theory by Zwikker and Kosten [90, 91] which encompasses the asymptotic theory by Kirchhoff. There is no mention of the accuracy of the results.

An overview of the published experimental results is shown in table 6.3. The table shows the reported systematic error in the results, the frequency range of the measurements, the radius of the used waveguides and the material of the wave guide, the shear wave numbers and Helmholtz numbers covered in the experiments. The shear wave number is given by,

$$\mathrm{Sh} = R\sqrt{\frac{\omega\rho}{\mu}}, \tag{6.18}$$

where R is the radius. For the table entries where the shear wave entries are calculated, the used gas is air and the density ρ and viscosity μ are taken from [92]. The second parameter is the Helmholtz number, also based on the duct radius,

$$\mathrm{He} = \frac{\omega}{c} R. \tag{6.19}$$

The table shows that there is a wide spread in all the parameters and no clear correlation with the accuracy of the measurements and the listed parameters can be seen. On the other hand, for the measurements where a high accuracy is seen, information on the wall roughness is present.

Significant effects of the wall roughness on the measured absorption coefficient can be seen from the results reported by Waetzmann [72] and Ahrens [28], this together with the notions made by Weston, that the discrepancy between measurements and modelling are most probably due to imperfect walls, indicates that the imperfect wall condition can be the source of error. The increase of the apparent absorption with increasing frequency supports the hypothesis, as the boundary layer thickness decreases with increasing frequency and thus the effect of roughness will increase. From the measurements results presented in figure 6.7, the only setup of which the wall roughness is known is that of the LAUM. The waveguides in this setup have been honed to have surface accuracy of 0.1 μm [78]. The results have the smallest difference and the slope of the linear regression is the lowest for these measurements, supporting the hypothesis.

6.4   Conclusion

In this chapter, the remaining systematic error in impedance tubes has been discussed. Two trends have identified and the first trend is oscillations in the measured reflection coefficient and the second a decay of the measured reflection coefficient with increasing frequency, leading to apparent loss of acoustic energy. With the help of a simplified setup, the plausible sources of the oscillations are identified, which are the influence of the microphones on the sound field and the presence of wall vibrations. A simplified analytical model to explain the effect of a finite microphone impedance agrees qualitatively well with the measured data. Unfortunately, no quantitative data of the microphone impedances could be obtained from the measurements, because the effect due to the microphones has a similar magnitude as that of the apparent absorption.

For the apparent absorption, several hypotheses have been discussed. These hypotheses included the effect of volumetric losses, the Konstantinov effect and the acoustic field in corners where the walls of the waveguide meet the rigid wall. These hypotheses can not explain the observed apparent absorption and after a literature survey, the most plausible source of error, the imperfect walls of the waveguides, is identified.

Flow acoustic interaction at the area expansion

In this chapter, the area-acoustic interaction at an area expansion is measured. Using the techniques presented in the previous chapters, the uncertainty in the measurements are determined and the accuracy improved. The results are compared against modelling results and show a slight deviation between the measured scattering coefficients and those obtained from the models. The acoustic absorption for waves incident from the upstream side of the area expansion is measured to be less than that predicted by the models.

7.1 Introduction

The simple configuration of a sudden area change of a waveguide has found the interest of many scholars [93, 94] and the acoustic properties of the area expansion without flow are well known [57, 95]. In most industrial applications, the main purpose of ducts is to facilitate a fluid flow and the presence of sudden area expansions or other duct irregularities can lead to flow separation. The flow separation opens a pathway for acoustic energy to be converted in hydrodynamic energy, and the relation between the acoustic fields up and downstream of the area expansion become dependent on the flow conditions.

In the beginning of the last century, simplified models were proposed to predict the flow acoustic interaction and it's influence of the acoustic behaviour of sudden area expansions. Quasi-steady state models were investigated where the flow profile was expanded behind the area expansion [96] and models where the flow kept the jet-shape [97]. It was concluded that the main influence of the flow on the acoustics was the presence of the unstable shear

layer and the flow should be modelled as a jet. The presence of entropy fluctuations at the area expansions was regarded to be of minor importance [98]. During the last decade, more sophisticated models where reported, both numerical [99–102] and analytical [103], which take into account the presence of non-uniform flow profiles.

Unfortunately experimental data to validate the models is not widely available. Dupére et al. [104, 105] investigated the absorption of acoustic energy at the area expansion in a setup with fixed acoustic boundary conditions. Lambert has experimentally investigated the upstream reflection coefficient for a fairly large expansion ratio of 0.25 [106]. The expansion ratio η is defined as the ratio of the cross sectional area of the upstream waveguide, S_a, to the cross sectional area of the downstream waveguide, S_b. The most complete results are reported by Ronneberger, first he experimentally investigated the reflection coefficient of the area expansion for waves incident upstream of the area expansion for various expansion ratios [96]. Later, he published results for the scattering matrix for a single area expansion ratio, $\eta = 0.346$. The scattering coefficients were measured for a wide range of flow speeds with the upstream Mach-number between 0 and 0.5, at five distinct frequencies [107].

The goal of this chapter is to present new experimental data accurate enough to compare it against recent modelling efforts. Experimental data in the plane wave range will be presented for 5 different flow speeds in the incompressible regime and with a high frequency resolution. First the scattering matrix of the area-expansion without a mean flow will be determined using a multi-microphone method and the uncertainty of the measurements is assessed using a linear uncertainty analysis. Comparing the confidence intervals against established models gives confidence in the precision of the experimental results. Thereafter, scattering matrices are presented for different mean flow speeds and the results compared with model predictions.

7.2   Acoustic sound interaction

The nature of the flow acoustic interaction is determined by the ratio of two time scales, the convective time scale of the flow and time scale of the perturbations.

The convective time scale is governed by the time needed for the pressure in the pressure recovery zone, downstream of the area-expansion, to settle to its new value when the flow is suddenly perturbed. This time is related to the time it takes for a fluid particle to travel through the pressure recovery zone and the size of the recovery zone is largely independent of flow velocity. Therefore, the convective time scale is inversely proportional to the flow velocity [96].

The time scale of the perturbations is inversely proportional to the frequency, and the

flow acoustic interaction can be characterized by the Strouhal number,

$$\text{St} = \frac{\omega R_a}{U},\tag{7.1}$$

where ω is the angular frequency of the perturbations, R_a the radius of the smaller duct and U the mean flow velocity, averaged over the duct cross section, of the smaller duct.

At high Strouhal numbers, the convective processes can not adjust to the fast acoustic oscillations and the main alteration to the acoustic wave propagation are convective effects. Therefore, the nature of the flow profile and the specific edge condition do not have a significant influence on the scattering coefficients [102, 108]. On the other hand, at low Strouhal numbers, the acoustic time scale is slow enough such that the hydrodynamic field can adjust itself to the perturbations. For these Strouhal numbers, acoustics have an effect to the vortex shedding and the resulting acoustic field is sensitive to the flow profile and edge conditions at the area expansion.

The mathematical models that are used to determine the acoustic sound interaction are often derived in the frequency domain. For a duct with a uniform flow, the solution of the acoustic wave equation is given by modes for which the axial wavenumber is proportional to the ratio of the angular frequency to the sound speed, the so called acoustic modes. For ducts where the flow is stratified with layers of different flow velocities, the solution to the equations consists of the acoustic modes and a set of extra modes, called the hydrodynamic modes.

For these hydrodynamic modes, the solution to the wavenumber is proportional to the ratio of the angular frequency and the flow speed ω/U. The velocity perturbations and the gradient of the vortex sheet of the solution will tend to infinity near the edge of the area expansion for both types of modes and to have a solution that it is finite, an extra condition has to be imposed, the so called Kutta condition [109].

The Kutta condition is not a universal boundary condition and there are multiple possibilities, which all lead to a finite solution of the acoustic scattering problem [109, 110]. In the following, the Kutta condition is a referred to as the boundary condition for which the vortex sheet at the trailing edge of the area expansion has zero gradient in the axial direction.

The Kutta condition is essential to have flow-acoustic interaction. For an open pipe Cargill [110] has shown that causal solutions can exist that do not satisfy the Kutta condition. However, in such situations, no acoustic power is transferred from the acoustic field to the hydrodynamic field and he concluded that the imposition of a Kutta condition is necessary to transfer power from the acoustic to the hydrodynamic field [110]. Cargill showed also that in the low frequency limit, the absorption of power is independent of the frequency. Howe showed that the exact modelling of the flow does not significantly affect the coupling
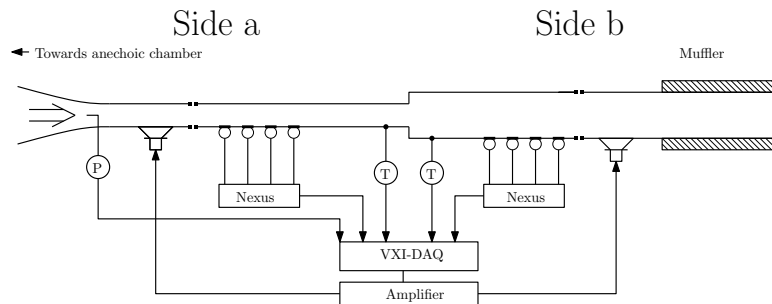
Figure 7.1: *Schematic overview of the experimental setup.*

between the hydrodynamic and acoustic field, but that the assumption of an infinitely thin shear layer overestimates the conversion from acoustic to hydrodynamic energy [111].

An open question is whether the Kutta condition can always be used or if the edge-condition should be dependent on the Strouhal number. Ronneberger hypothesized that the difference between his model predictions and measurements could be due to the frequency dependent separation position of the flow. He hypothesized that at higher frequencies, the acoustic boundary layer thickness becomes smaller than the hydrodynamic boundary layer. Under these conditions, the separation point of the flow will not be stationary but oscillate, leading to a modulation of the jet cross sectional area at higher frequencies. A simplified model indicated that this hypothesis agrees with the measurement data [107].

Michalke [112] has shown that the shear layer is only unstable for small Strouhal-numbers. To include the effect of a stable shear layer, Boij et al. [108] changed the Kutta condition in their model at the edgeto a relaxed Kutta conditions, such that size of the amplitude of the hydrodynamic could be controlled. At high Strouhal numbers, the effect of the hydro-dynamic modes is reduced and the results with the normal Kutta condition and relaxed Kutta condition seemed to converge. At low Strouhal numbers, the effect of hydrodynamic modes are important and the normal Kutta condition agrees better with the experimental results compared with the relaxed Kutta condition. For Strouhal numbers close to the criti-cal Strouhal numbers for the stability of the shear layer, the relaxed Kutta condition showed an improvement in the correspondence between theory and experiment.

7.3   Experimental setup and methods

A schematic of the experimental setup is given in figure 7.1. It consists of two circular ducts connected to each other to create a sudden area expansion. The edge at the area expansion has been carefully machined to be as sharp as possible with conventional methods, leading

to a well defined separation point of the flow. Upstream of the area expansion, the duct diameter is $D_a = 50$mm and downstream the duct diameter is $D_b = 90$mm, resulting in an area expansion ratio of $\eta = 0.309$.

The acoustic excitation is provided by loudspeakers attached to the upstream and downstream duct far from the area discontinuity. The acoustic reflections at the two ends of the duct have been reduced by connecting the upstream duct to anechoic chamber with a horn shaped duct and the downstream duct to a muffler. If there are strong reflections, partial standing waves are created which reduce the signal to noise ratio at the microphones. Furthermore, it can lead to dependent sound fields when determining the scattering matrix increasing the sensitivity to errors (see chapter 4). Both effects will be taken into account by the uncertainty analysis and will result in enlarged confidence intervals in the results.

The pressure fluctuations are registered by eight flush mounted microphones, placed in the upstream and downstream duct. The microphones are Brüel and Kjær 1/4 inch condenser microphones of type 4938, attached to a NEXUS signal conditioner. The distance between the microphones and the loudspeakers and the microphones and the area expansion is large enough to ensure that only propagating waves are measured. The microphones have been calibrated in gain and phase relative to each other by exposing all the microphones to the same sound field in a calibrator [63].

The flow through the sudden area expansion is created by pressurizing an anechoic chamber. The mean flow is determined by assuming a fully turbulent flow profile and measuring the centreline velocity of the upstream duct using a Prantl-tube. The exact flow profile at the area expansion has been measured to characterize the bias error in the determination of the mean flow speed. Results of the measurements will be shown in the next section. The temperature of the flow is monitored via two thermocouples, both attached to the outside of the aluminium waveguides upstream and downstream of the area expansion. Five different flow speeds have been measured and correspond to a cross sectional averaged Mach number of the smaller upstream duct, M_a, equal to 0.05, 0.10, 0.15, 0.20 and 0.25. These flow speeds result in a range of Reynolds numbers (based on the hydraulic diameter of the upstream duct) of $5.2 \cdot 10^4 < \mathrm{Re} < 2.7 \cdot 10^5$.

The acquisition of the measurement signals and the excitation of the loudspeakers are controlled by a HP-VXI system. The signal to noise ratio is increased by driving the loudspeakers by a single tone and to reduce the measurement time, the loudspeakers up- and down-stream of the area expansion are simultaneously driven. The upstream speakers are excited at a different frequency than the downstream speakers. These frequencies are chosen randomly and ensured that the frequencies of the up- and down-stream speakers are not a multiple of each other. The transfer functions between the excitation signal and the measured acoustic pressure are obtained using a synchronous demodulation technique [11].
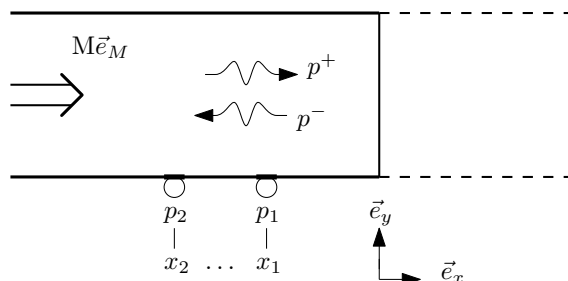
Figure 7.2: *Schematic overview of the used wave definitions.*

More information can be found in chapter 2. Before acquiring data, the sound field in the duct has been decomposed in incoming and reflected acoustic plane waves and the amplitude of the reference signal towards the loudspeaker has been automatically regulated to have the same incident wave amplitude for each frequency.

Methods

The measurement frequencies are below the first cut-on frequencies of the higher order modes and only plane waves are able to propagate in the duct.

The wave propagation equation (3.62) for each side of the area expansion is reduced in this case to:

$$
\begin{bmatrix}
\exp(-ik(\vec{e}_M \cdot \vec{e}_x M)x_1) & \exp(+ik(\vec{e}_M \cdot \vec{e}_x M)x_1) \\
\vdots & \vdots \\
\exp(-ik(\vec{e}_M \cdot \vec{e}_x M)x_n) & \exp(+ik(\vec{e}_M \cdot \vec{e}_x M)x_n)
\end{bmatrix}
\begin{bmatrix} p^+ \\ p^- \end{bmatrix}
=
\begin{bmatrix} p_1 \\ \vdots \\ p_n \end{bmatrix}.
\tag{7.2}
$$

Herein is x_n the axial position of the n-th microphone, k the wavenumber in the duct, which is a function of the cross sectional averaged Mach number M and the flow direction $\vec{e}_M \cdot \vec{e}_x$ within the duct and p_n the measured complex pressure at position x_n. A schematic representation of the wave definition is given in figure 7.2.

An estimation of the wave numbers upstream and downstream of the area expansion is obtained using a model by Weng et al. [21]. The model takes into account the presence of the convective effects and the thermo-viscous damping. The effects of turbulent interaction and refraction effects are not taken into account. The turbulent interaction becomes important when the acoustic boundary layer thickness is larger than the turbulent boundary layer [113] [34] and in the current experiments, the frequencies used are sufficiently high such that the turbulent interaction can be neglected. The speed of sound, used to calculate the wavenumbers, is determined with the model by Cramer [65] which takes into account the

effect of temperature, humidity and barometric pressure. The physical transport properties of the fluid in the duct, air, are calculated using the model by Tsilingiris [92], which takes into account the effects of humidity.

The scattering matrix, relating the upstream and downstream propagating wave is obtained by measuring two linearly independent sound fields, (3.60), which are created by exciting the sound fields using the upstream and downstream loudspeakers. In this case, the plane wave scattering matrix S is given by,

$$S = \begin{bmatrix} \mathscr{R}_a & \mathscr{T}_{b \to a} \\ \mathscr{T}_{a \to b} & \mathscr{R}_b \end{bmatrix}. \tag{7.3}$$

The scattering matrix consists of four coefficients, which are the upstream reflection coefficient $\mathscr{R}_a$, the transmission coefficient from the upstream to downstream side $\mathscr{T}_{a \to b}$, the reflection coefficient on the downstream side $\mathscr{R}_b$ and the transmission coefficient from the downstream to the upstream side $\mathscr{T}_{b \to a}$.

From the above coefficients, other quantities can be derived, such as the end correction l. The end correction is a measure of the linear dependency of the phase of the reflection coefficient on the frequency. The dimensionless end correction, $\delta = l/R_a$, based on the upstream duct radius is related to the phase angle of the reflection coefficient as [114] [93],

$$\mathscr{R}_a = -|\mathscr{R}_a| \exp\left(2ik\delta R_a\right), \tag{7.4}$$

where i is the imaginary unit. This quantity is derived for fluids which are quiescent, and to extend it to flowing fluids, the convective effect on the wave propagation has to be taken into account [103],

$$\mathscr{R}_a = -|\mathscr{R}_a| \exp\left(\frac{2ikR_a}{1 - M_a^2}\delta\right), \tag{7.5}$$

where M_a is the cross sectional averaged Mach number of the upstream duct a.

Another derived quantity is the acoustic absorption coefficient, which gives a measure of the absorption or production of acoustic energy per unit time and is dependent on the acoustic boundary conditions. In the presence of mean flow and viscous and thermal damping, the determination of acoustic intensity becomes problematic because of the non-uniformity of the flow and acoustic velocity profiles and therefore some simplifying assumptions have to be made. Therefore, the calculation of the energy flows is based on the assumption of a uniform flow and excluding the effects of the acoustic boundary layer [115].

Under this assumption, the acoustic power scattering matrix is related to the acoustic scattering matrix [116] through,

$$S_{\mathscr{P}} = T^- S \left(T^+\right)^{-1}, \tag{7.6}$$

where $T^{\pm}$ is a diagonal matrix,

$$
T^{\pm} = \begin{bmatrix} \pm(1 + \vec{e}_M \cdot \vec{e}_x M_a)\sqrt{Y_a} & 0 \\ 0 & \pm(1 + \vec{e}_M \cdot \vec{e}_x M_b)\sqrt{Y_b} \end{bmatrix}. \tag{7.7}
$$

with on the diagonal $\pm(1 + \vec{e}_M \cdot \vec{e}_x M_i)\sqrt{Y_i}$. The variable $Y_{a,b}$ is given by $\rho_0 S_{a,b}/c_0$, where ρ_0 is the density of the acoustic medium, $S_{a,b}$ the cross sectional area of respectively the upstream and downstream duct and c_0 the speed of sound in the specific duct.

With the acoustic power scattering matrix, the acoustic absorption/generation coefficients for waves incident from the upstream duct and a reflection free termination at the downstream duct α_a, or vice versa α_b can be calculated using,

$$
\alpha_a = \sum_{j=1}^{2} |S_{\mathscr{P}}[1,j]|^2 - 1, \text{ and,} \tag{7.8}
$$

$$
\alpha_b = \sum_{j=1}^{2} |S_{\mathscr{P}}[2,j]|^2 - 1. \tag{7.9}
$$

Experimental precision and accuracy

In order to obtain accurate measurement results, several techniques have been applied to reduce the bias errors in the measurement.

The acoustic centers of the microphones are acoustically determined by measuring the impedance of a rigid wall and optimizing the microphone positions, such that the discrepancy between theoretical and measured pressures are minimized (see section 5.3).

The duct where the loudspeaker are positioned and the measurement duct where the microphones are situated are physically detached to reduce the influence of mechanical vibrations caused by the loudspeakers. The gap between the two sections is made as small as possible ($\sim$0.1mm) and the sections are connected using duct-tape to have no leakage. With this arrangement, the bias errors caused by mechanical vibrations from the loudspeakers are significantly reduced (see section. 5.3).

The travelling wave components have been estimated with the widely linear minimum variance unbiased estimator of the solution to equation (7.2) (see also appendix B.3), which takes into account the statistical information from the measurements. The statistical information on the measured transfer functions is obtained using a methodology based upon synchronous demodulation (appendix B.2). With the estimator, the error introduced by the flow noise, which is the dominant error at lower frequencies (<200Hz), is reduced.

The flow profiles of the jet at the area expansion have been measured to determine if the fluid flow is fully developed. In figure 7.3 the measured flow profile at the expansion is
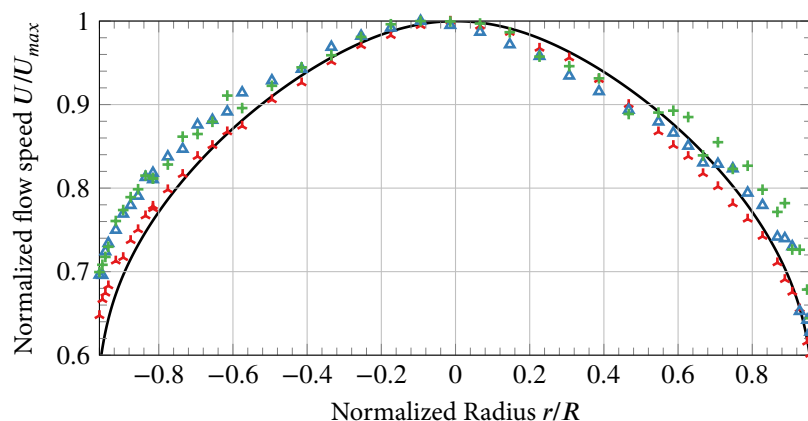
Figure 7.3: *Measured flow profile at the area expansion for three flow speeds:(▴) U_{max} = 10.67 m/s, (△) U_{max} = 57.93 m/s,(+) U_{max} = 105.0 m/s, (——) fully developed profile from DNS modelling (Re = 24 000) [117].*

shown for three flow speeds corresponding to upstream Mach numbers of M ≈ 0.03, 0.15 and 0.3. The flow profile on the upstream side shows a good agreement with that of a fully developed turbulent profile obtained from DNS simulations [117] for all measured speeds. The slight asymmetry that is present in the flow is caused by the loudspeakers attached to the pipe. At the loudspeaker position, a pattern of holes has been drilled to be able to excite the sound field, which also influence the hydrodynamic boundary layer and the velocity profile does not fully develop itself before it reaches the area expansion.

Even though the flow profiles agree well with theoretical profiles, the differences lead to an over-determination of the average wave convection flow speed of around 5% for the highest flow speeds [58]. Furthermore, due to the turbulent boundary layer at the duct walls, momentum is converted in heat. If the duct walls are adiabatic, the wall temperature will be higher than that of the bulk flow [118]. This effect is larger than the measurement uncertainty in the temperature, but is not well defined because the thermal boundary conditions of the duct walls are not regulated. To reduce the bias errors caused by an incorrect wave convection flow speed and temperature of the bulk flow, the wave convection flow speed and the temperature are optimized by minimizing the frequency averaged residual of equation (7.2) [119],[120].

The influence of compressibility has been addressed using the compressible relations for a one-dimensional flow with friction [15]. The friction factor has been estimated [121] to be equal to $f = 0.0035$ and the Mach number just at the outlet of the are expansion taken to be 0.3. The velocity between the area expansion and the last microphone in the upstream

Table 7.1: *Standard deviation of the measurement parameters (see appendix A.3)*

Quantity	No flow	flow
Microphone Positions	0.1mm	0.1mm
Temperature	0.0625 ^{o}C	0.5^o C
Humidity	5 %	5 %
Ambient Pressure	0.1 hPa	0.1 hPa
Mean velocity	N.A.	2% Full scale
Microphone pressures	From measurements	From measurements

section differs at most 1.6%. As the wave numbers are proportional to $(1 \pm M)^{-1}$, the resulting error is at most 0.7%. In light of the error made in the determination of the flow velocity this effect is small. Therefore, the compressibility effects, such as a wave number that depends on the position along the duct [107], are not taken into account.

7.4   Results

In this section, the results from the measurements are shown and compared to model results. First the results of the quiescent area expansion, obtained to validate the measurement procedure, are discussed. Thereafter, the scattering coefficients for the case where there is a mean flow will be shown and compared against models results available in literature.

To show the effect of frequency dependency, the absolute values of the scattering coefficients will be normalized against the quasi-steady state response. The quasi-steady state response is determined by assuming a uniform mean flow in both ducts and applying the conservation of mass, momentum and energy [96, 107].

A linear multi-variate analysis has been used to determine the uncertainty in the measurements as explained in chapter 4. The covariance matrix has been scaled and rotated to determine the uncertainty with respect to the amplitude and phase of the scattering coefficients [60]. The uncertainty is presented using two Bonferonni intervals [45],the first interval is the 65% confidence interval and the second the 95% confidence interval. The uncertainties used to calculate the intervals are given in table 7.1, and are based on technical documentation and measurements (see appendix A.3).

Quiescent area expansion

The results of the quiescent area expansion will be compared against two models. The first model is a model by Kergomard [95], where approximate relations are given based on the exact solution to the problem. The second model is that of Aurégan [122], which is a simpli-
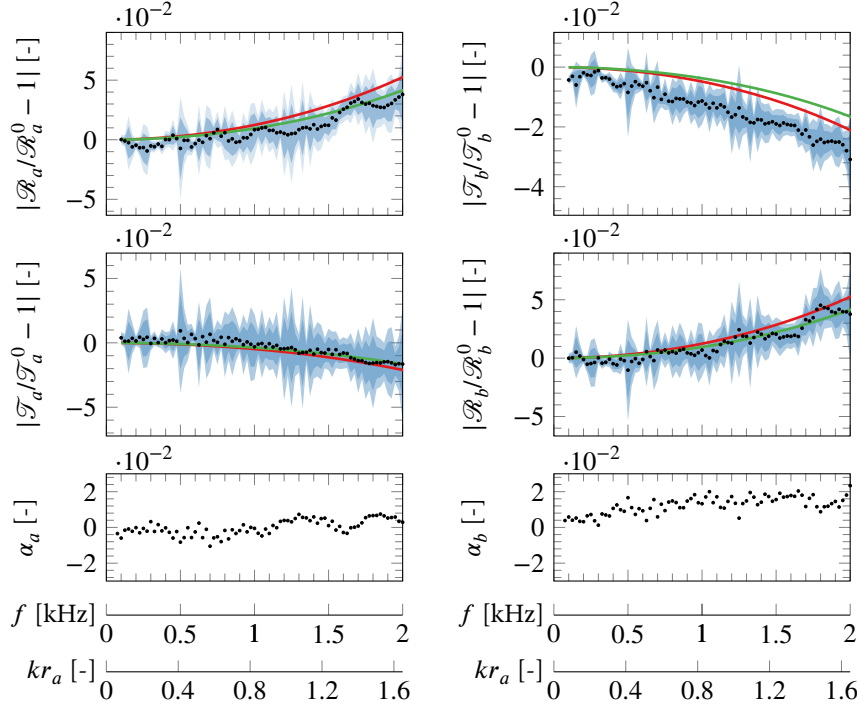
Figure 7.4: *Measured absolute values (·) of the scattering and absorption coefficients as function of the frequency and Helmholtz number together with the 95% and 65% confidence intervals (, respectively). Model results by Aurégan (——) and Kergomard (——).*

fied solution to the problem, obtained by integrating the governing equations. The influence of viscous thermal effects at the edge of the area expansion can be neglected, because the acoustic boundary layer is much smaller than the duct radii for the investigated frequency range [57].

In the first two rows of figure 7.4 the amplitudes of the measured scattering coefficients are shown together with the 65% and 95 % confidence intervals. In the bottom row of the figure, the calculated sound absorption coefficient for sound incident from the upstream respectively downstream side of the area expansion. Figure 7.5 shows the measured phase of the scattering coefficients. The scattering coefficients are relative to the quasi-steady response and for reference these values are given by,

$$S^0 = \begin{bmatrix} -0.528 & 1.528 \\ 0.472 & 0.528 \end{bmatrix}. \tag{7.10}$$

In the same figures, the model results from the models of Kergomard [95] and Aurégan

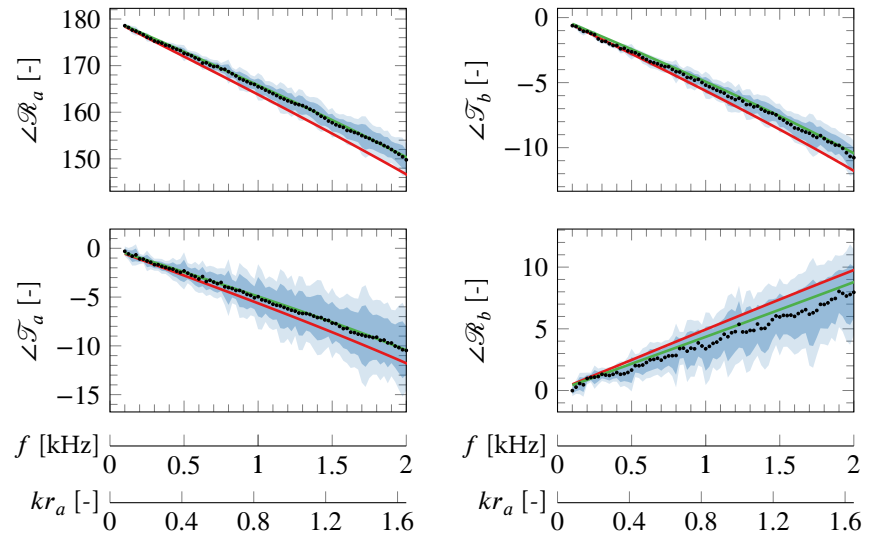**Figure 7.5:** *Measured phase (·) of the scattering coefficients as function of the frequency and Helmholtz number together with the 95% and 65% confidence intervals(▪ , ▪ respectively). Model results by Aurégan (——) and Kergomard (——).*

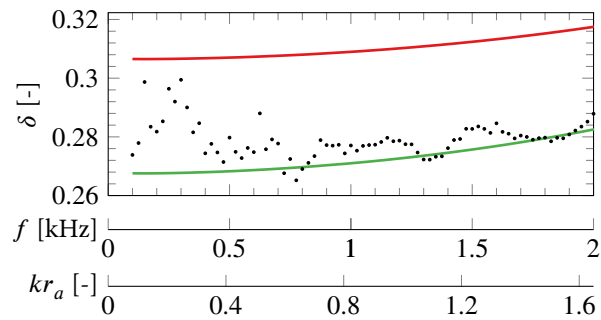**Figure 7.6:** *Dimensionless end correction as function of frequency. The measurements are given by (·). The model results of Aurégan (——) and Kergomard (——).*

[122] are shown.

The quasi-steady state response of the area expansion is governed by the continuity of mass and momentum. However, higher order modes are excited when an acoustic wave is incident and these higher order modes represent a reactive acoustic load which is dependent on the frequency. The influence of this reactive load on the absolute value of the acoustic scattering coefficients is small for the current configuration, the absolute values differ at most 5% from the quasi-steady state value over the measured frequency range. The influence is more noticeable in the phase of the scattering coefficients, which are linear proportional to the frequency and the largest phase shift with respect to the steady state value is 30 degrees at 2000 Hz for the upstream reflection coefficient $\mathcal{R}_a$.

A good agreement between the models and measurements is seen for the upstream reflection coefficient, $\mathcal{R}_a$, and transmission coefficient from the upstream to the downstream side, $\mathcal{T}_{b \to a}$. The relative difference between the absolute values of the model predictions and the measured results is in the order of 1% over the complete range of the investigated Helmholtz number $kr_a = [0 - 1.6]$.

The influence of thermo-viscous losses at the edge of the area expansion can be neglected [57], and thus the absorption coefficient for waves incident from the upstream and downstream side should both equal to zero. The scattering coefficients for waves incident from the upstream side show good agreement with the model results, and consequently the absorption coefficient for waves incident on the upstream side is adequately represented, as the deviation between the theoretical case, $\alpha_a = 0$, and the measurements are within 1%.

For the downstream reflection coefficient $\mathcal{R}_b$, there is a deviation seen between the model and measurement results, which is slightly larger than the 95 % confidence interval and the difference is around 2%. On the other hand, the transmission coefficient from the downstream to the upstream side $\mathcal{T}_{b \to a}$, is within the 95% confidence interval bounds from the measurement results. As the measured reflection coefficient is lower than that predicted by the model, the measured absorption coefficient is larger than zero, indicating that acoustic energy is lost.

The phase of all the scattering coefficients is in a good agreement with the models and the model of Kergomard shows the best agreement. The measured phase deviates at most 1° from the measured value and the model results are within the 95 % confidence intervals. In figure 7.6, the non-dimensional end correction is shown as function of frequency. For the higher frequency, the end correction agrees with the end correction predicted by the model of Kergomard. For the lower frequencies, the phase difference induced by the reactive load becomes smaller and approaches the precision of the measurement setup, resulting in an increase of the scatter.

The origin of the systematic deviation between the measurements and the downstream

Approximate Mach number	0.05	0.10	0.15	0.20	0.25
Measured Mach number	0.0469	0.0960	0.1435	0.1936	0.2433

Table 7.2: *Measured Mach numbers*

reflection coefficient is not known, but most probably it is related to the observed systematic error in the impedance tube (see chapter 6). Unfortunately it is difficult to assess how this systematic error affect the measurements when flow is present, and care should be taken when interpreting the confidence intervals. Nevertheless, the observed error is deemed small as it leads to a maximum relative error of 1% in the absolute values of the scattering coefficients and a maximum error of 2% in the absorption coefficient.

Area expansion with flow

The scattering matrix has been measured for five different flow speeds such that averaged mass flow would correspond to that of uniform mean flow of a Mach number of approximately 0.05, 0.10, 0.15, 0.20 and 0.25. In table 7.2 the measured upstream Mach number, obtained from the optimization procedure is shown. Hereafter, for ease of reading the results will be referred by using the approximate numbers indicated in the table. The measurement results with mean flow will be compared with three models using the coefficients of the individual scattering coefficients, the reflection free absorption coefficients and the end correction.

The first model that will be considered is a model by Kooijman et al. [102, 123]. The model discretizes the linearised equations of an isentropic fluid with an arbitrary mean flow profile in both ducts and uses a mode-matching technique to obtain the scattering matrix. In the calculations, a 7th power law model has been used to estimate the velocity profile in the upstream duct. This velocity profile has no axial velocity at the wall, and therefore the Kutta-condition does not have to be specified in the model.

The second model that will be considered is a model by Boij and Nilsson. The used geometry is a rectangular duct, where one half has a uniform flow profile and in the other half there is no mean flow. The two parts are divided by a semi-infinite wall and the problem is solved with the Wiener-Hopf technique [108, 124]. As the results are obtained for a rectangular configuration, a scaling proposed by Boij and Nilsson is used to scale the data to circular geometries [124]. The scaling is determined by the normalized Helmholtz number, He*, where the Helmholtz number is scaled by the cut-on frequency of the first higher order

mode in the downstream duct. The scaling is given by,

$$\text{He}^* = \frac{1}{\eta} \frac{(kh)_{rec}}{\pi} = \frac{1}{\sqrt{\eta}} \frac{(kr_a)_{cyl}}{\kappa_0}, \tag{7.11}$$

where h is the height of the upstream rectangular duct and κ_0 is the first zero crossing of the derivative of zero-th order Bessel function. The numerical value is given by $\kappa_0 \approx 3.832$.

Kooijman compared the obtained results from the circular and rectangular geometry, using the proposed scaling by Boij and Nilsson. He calculated the scattering coefficients as function of Mach number at a distinct Helmholtz number, based upon the upstream duct radius, for two expansions ratios $\eta = 0.33$ with $kr_a = 0.2113$ and $\eta = 0.5$ with $kr_a = 0.1725$. For the rectangular case, there is a distinct increase of the absolute value for the upstream reflection coefficient $\mathcal{R}_a$ and the transmission coefficient from the downstream to the upstream side $\mathcal{T}_{b \leftarrow a}$ at a Strouhal number of 1. Kooijman showed that the largest relative deviation of the absolute value of the scattering coefficients is obtained for the area expansion ratio of $\eta = 0.33$. Of the four coefficients, the absolute value of the upstream reflection coefficients $|\mathcal{R}_a|$ showed the largest difference between the rectangular and circular geometry at a Strouhal number of 1. The relative deviation is in the order of 3%.

The third model that will be considered is a simplified model by Aurégan [116]. The model determines the dispersion relation for a channel where there are two zones, a jet core with uniform flow and annulus around the core with no flow. The dispersion relation is found integrating the governing equations over the different zones and match the equations at the interface. It gives rise to three travelling waves, the plane acoustic wave, a higher order acoustic mode and an exponential growing hydrodynamic mode. Using the boundary conditions at the area expansion, the relation between waves at the upstream and downstream acoustic waves can be found. This model is similar to models proposed by Cummings [97, 98] and Ronneberger [107].

The absolute values of the measured scattering coefficients for three mean flow speeds, $M_a \approx 0.05$, $M_a \approx 0.15$ and $M_a \approx 0.25$ are shown respectively shown in figure 7.7, 7.9 and 7.11 as function of frequency and Strouhal number. The measured angles are shown in figure 7.8, 7.10 and 7.12. For the model by Boij, the frequencies have been scaled according to (7.11). The Strouhal number is based on the cylindrical Helmholtz number. The absolute values are shown relative to the quasi-steady state response, given by,

$$M_a \approx 0.05 \quad \mathbf{S}^0 = \begin{bmatrix} -0.5524 & 1.5517 \\ 0.4789 & 0.5213 \end{bmatrix}, \tag{7.12}$$

Figure 7.7: *Measured absolute values (·) of the scattering coefficients for an upstream Mach number of $M_a \approx 0.05$. Shown as function of the frequency and Strouhal number together with the 95% and 65% confidence intervals (, respectively). Model results by Aurégan ( ), Kooijman ( ) and Boij ( ).*

Figure 7.8: *Measured phase (·) of the scattering coefficients for an upstream Mach number of $M_a \approx 0.05$. Shown as function of the frequency and Strouhal number together with the 95% and 65% confidence intervals(, respectively). Model results by Aurégan ( ), Kooijman ( ) and Boij ( ).*
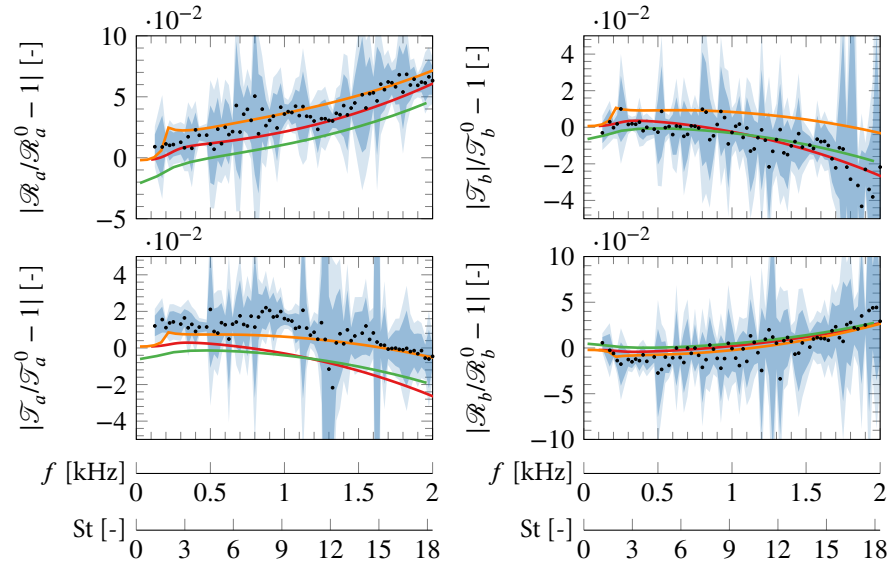
Figure 7.9: *Measured absolute values (·) of the scattering coefficients for an upstream Mach number of $M_a \approx 0.15$. Shown as function of the frequency and Strouhal number together with the 95% and 65% confidence intervals (, respectively). Experimental results by Ronneberger (+). Model results by Aurégan ( ), Kooijman ( ) and Boij ( ).*
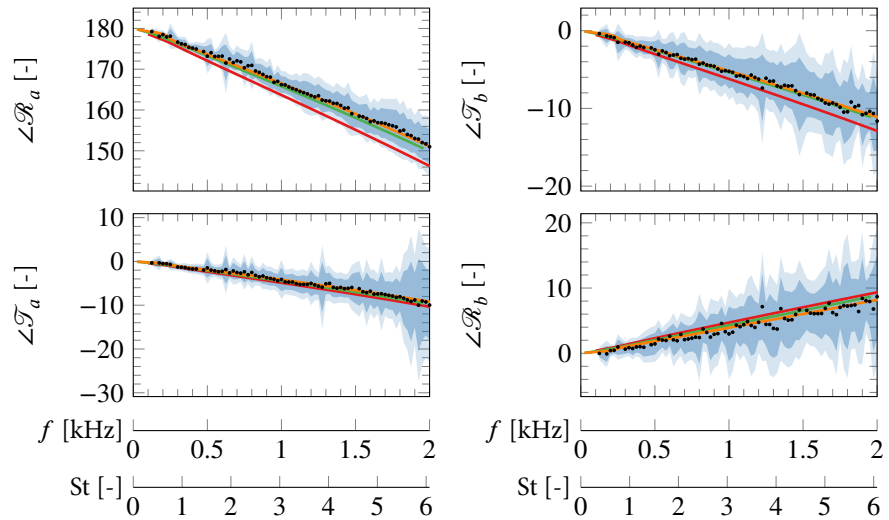

Figure 7.10: *Measured phase (·) of the scattering coefficients for an upstream Mach number of $M_a \approx 0.15$. Shown as function of the frequency and Strouhal number together with the 95% and 65% confidence intervals(, respectively). Experimental results by Ronneberger (+). Model results by Aurégan ( ), Kooijman ( ) and Boij ( ).*
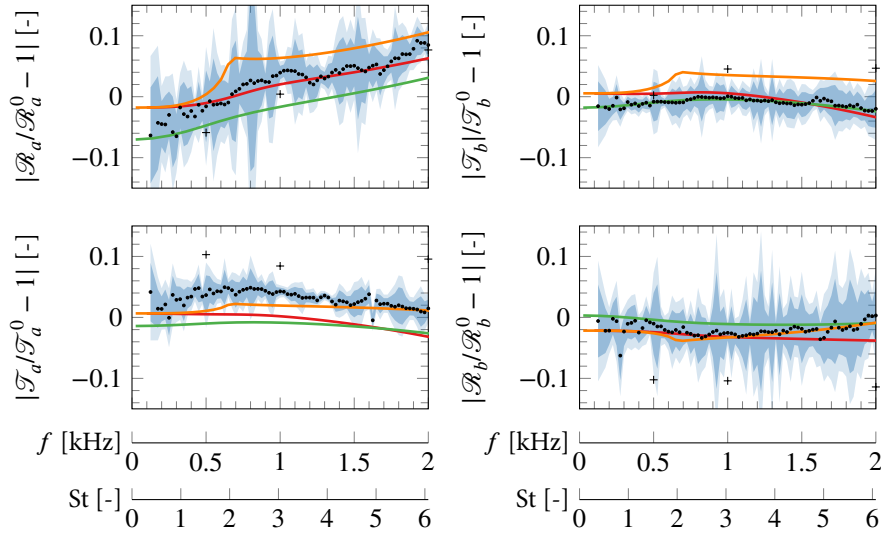
Figure 7.11: *Measured absolute values (·) of the scattering coefficients for an upstream Mach number of $M_a \approx 0.25$. Shown as function of the frequency and Strouhal number together with the 95% and 65% confidence intervals (, respectively). Model results by Aurégan ( ), Kooijman ( ) and Boij ( ).*
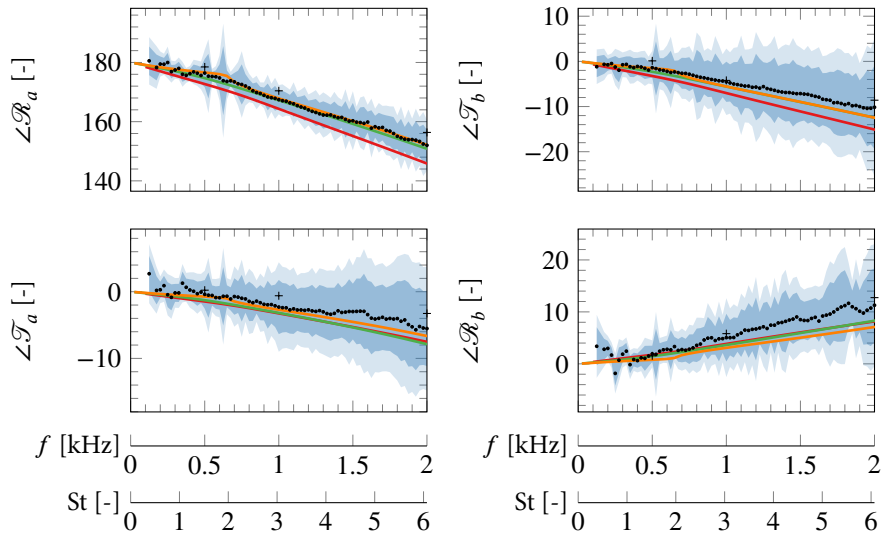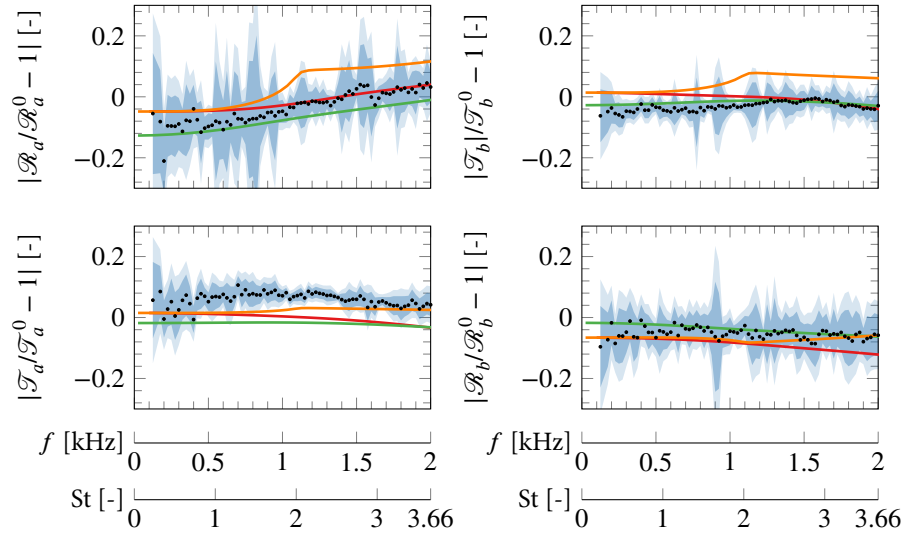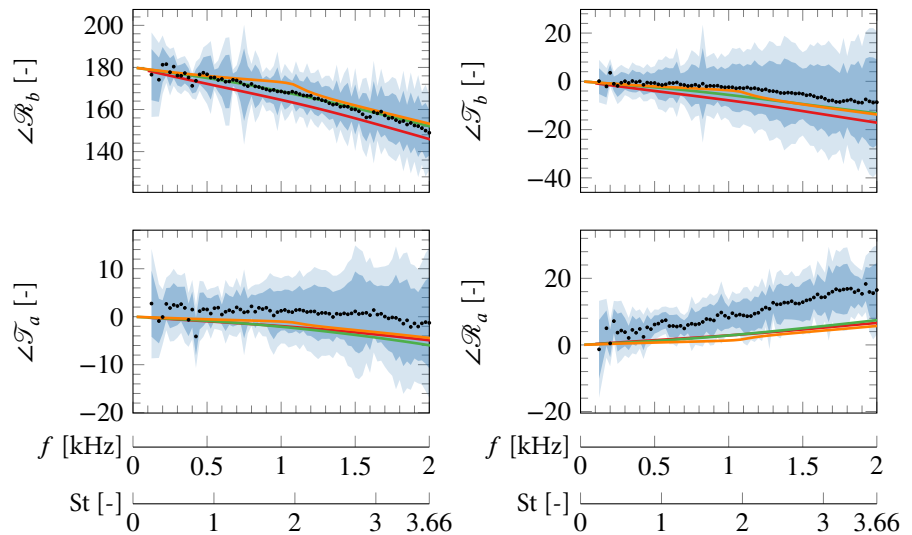

Figure 7.12: *Measured phase (·) of the scattering coefficients for an upstream Mach number of $M_a \approx 0.25$. Shown as function of the frequency and Strouhal number together with the 95% and 65% confidence intervals(, respectively). Model results by Aurégan ( ), Kooijman ( ) and Boij ( ).*

$$M_a \approx 0.15 \quad \boldsymbol{S}^0 = \begin{bmatrix} -0.6068 & 1.5993 \\ 0.4934 & 0.5083 \end{bmatrix}, \tag{7.13}$$

$$M_a \approx 0.25 \quad \boldsymbol{S}^0 = \begin{bmatrix} -0.6703 & 1.6471 \\ 0.5079 & 0.4966 \end{bmatrix}. \tag{7.14}$$

The measurement results by Ronneberger [107], obtained for an area expansion ratio of $\eta = 0.346$ and at 3 frequencies, 500, 1000 and 2000 Hz, are also shown for a qualitative comparison in figure 7.9 and 7.10. The results are shown relative to the response given in equation (7.13).

From the results it can be seen that the relative change of the absolute values over the investigated frequency range is small, the changes for the upstream reflection coefficient $\mathscr{R}_a$ is the largest, which is on the order of 10% whereas the changes of the other coefficients are in the order of 5%. The changes of the phase of the coefficients is similar to those obtained for the area expansion without flow and are at most 30°.

The model by Kooijman is consistently lower than the measured absolute value of the upstream reflection coefficient $\mathscr{R}_a$ for all measured flow speeds. The model by Aurégan shows a fair agreement and the model by Boij over predicts the results, at large Strouhal numbers. In the low frequency limit, both the model by Aurégan and Boij predict the same absolute value of the reflection coefficient and are close to the quasi-steady state values by Ronneberger [107] whereas the model by Kooijman does not reach the same value.

For the absolute values of the transmission coefficient from the upstream to downstream side $\mathscr{T}_{a \to b}$ all the models are below the measured values. The deviations, compared to the uncertainty intervals are larger than those obtained for the upstream reflection coefficient. The measurement results tend to the quasi-steady state results, but it is difficult to asses due to the comparatively large scatter at the lower frequencies.

The model by Boij over predicts the absolute values of the downstream reflection coefficient $\mathscr{R}_b$, especially at higher Strouhal numbers, but both models by Kooijman and Aurégan show fair agreement. For the downstream to upstream transmission coefficient $\mathscr{T}_{b \to a}$, all the model results are in fair agreement and the deviations are all in the order of the size of the confidence intervals.

For the phase of the scattering coefficient, the model predictions by Boij and Kooijman are very similar and agree well with the measured phase of the coefficients. The model predictions by Aurégan show slightly larger deviation. For the phase of the transmission coefficient of the upstream to the downstream side, it is seen that the deviation between the models and the measured values increase with increasing Mach number, and at the highest Mach number, $M \approx 0.25$ the deviation is larger than the 95% confidence interval.
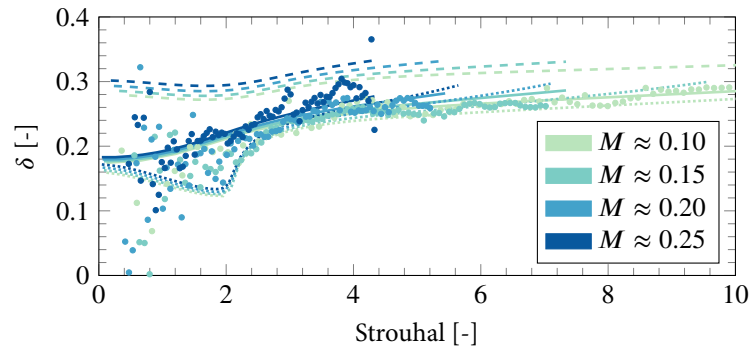
Figure 7.13: *End correction as function of Strouhal number. The measurements are given by (●). The model results by Aurégan (- - -), Kooijman (——) and Boij (·········).*

In figure 7.13 the non-dimensional end correction as function of Strouhal number is shown. The results at low Strouhal number, St < 2, show large scatter, which can be accounted to two effects. The first effect is that the phase shift is linearly dependent on the frequency and thus the relative influence of noise on the phase shift becomes stronger at lower frequencies. Furthermore, the flow noise has a pink noise characteristic and the signal to noise ratio decreases with lower frequencies.

In the same figures, the model results of the models are also shown. The results by the model of Boij are scaled such that they correspond to the Strouhal number with respect to the cylindrical Helmholtz number. The non-dimensional end correction is based on the upstream duct radius. The model by Aurégan over predicts the end correction for all the measured Strouhal numbers, but the trend is captured reasonably well. The model predictions by Kooijman are in good agreement with the measured results, especially for the higher Strouhal numbers, Strouhal > 2.

Boij and Nilson predicted a minimum in the end correction for Strouhal numbers around 1 [103]. The results show a decaying trend for Strouhal numbers smaller than 2, however due to the scatter it is impossible to determine whether a minimum is achieved. The difference between the end corrections of Kooijman and Boij in figure 7.13 at a Strouhal number of 2 between Kooijman and Boij, corresponds to a difference in phase shift of 3° at a Mach number of $M \approx 0.25$. This induced phase shift is fairly small and it is difficult to determine these shift accurately with the current setup.

In figures 7.14 and 7.15 the acoustic absorption coefficient is shown for waves incident upstream from the area expansion, α_a, and waves incident downstream from the area expansion, α_b. The results show that for flow speeds higher than $M > 0.05$ and Strouhal numbers lower than 2, the absorption coefficient for waves incident from the upstream side, α_a, in-

Figure 7.14: *Absorption coeffiecient as function of Strouhal number for two different Mach numbers $M \approx 0.05$ and $M \approx 0.10$. The measurements are given by (●). The model results by Aurégan (——), Kooijman (- - -), and Boij (·········). The arrows in the side margins of the plot denote the absorption predicted by the quasi-steady state model.*

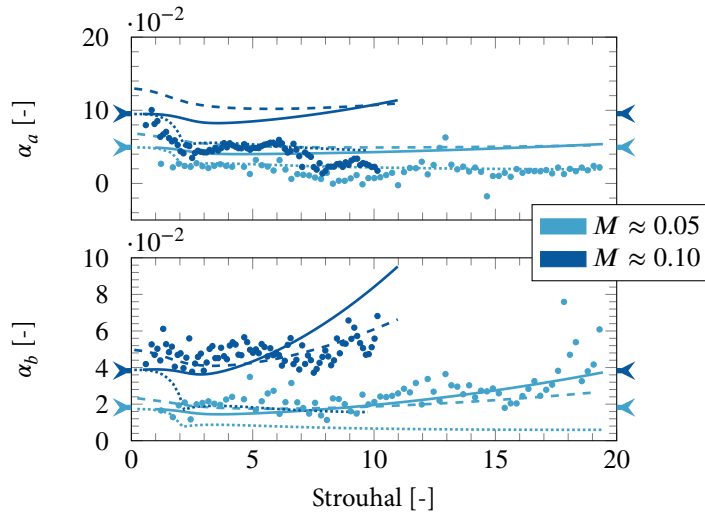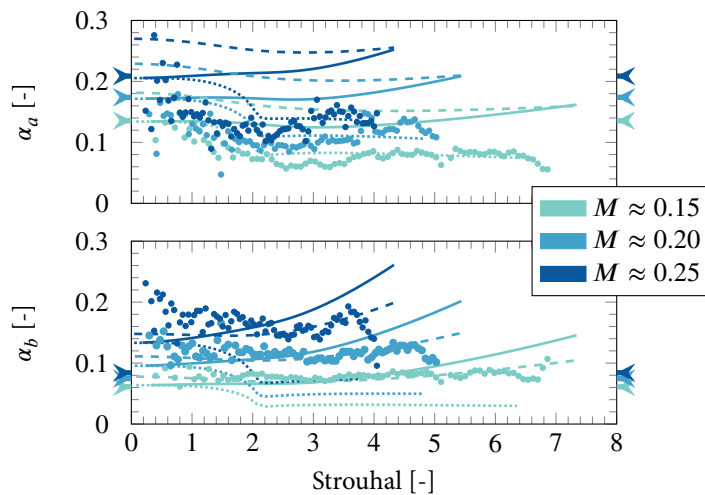**Figure 7.15:** *Absorption coeffiecient as function of Strouhal number for three different Mach numbers $M \approx 0.15$, $M \approx 0.20$ and $M \approx 0.25$. The measurements are given by (●). The model results by Aurégan (——), Kooijman (- - -), and Boij (·········). The arrows in the side margins of the plot denote the absorption predicted by the quasi-steady state model.*

creases with lowering Strouhal number, and comes close to the quasi-steady state values. For higher Strouhal numbers, the absorption remains approximately constant or slightly increases when the flow speed is large.

For the absorption coefficient of waves incident of the downstream side, α_b, the absorption does not depend strongly on the Strouhal number and slowly increases with increasing flow speed. For the lowest flow speeds $M \approx 0.05$ and $M \approx 0.10$, the measurements are close to the quasi-steady state values, but this deviation increases at higher Mach numbers.

In the same figures, the model predictions are also shown. The model predictions by Boij and Aurégan have the same absorption for low frequencies, in concordance with the results obtained from the scattering matrices. For the upstream absorption coefficient, the low frequency limit coincides with the absorption predicted by the quasi-steady state model, but for the downstream absorption coefficient, the limit and the quasi-steady state predictions do not coincide for the highest flow speeds. The model by Kooijman predicts an absorption coefficient that is too high for both absorption coefficients, but the deviations is the largest for the upstream absorption coefficient α_a.

For the absorption coefficient when waves are incident from the downstream side, α_b, both the models from Aurégan and Kooijman agree reasonably well and show the same trends as the observed measurements. The model predictions by Boij under predict the absorption coefficient and show a distinct behaviour at a Strouhal number of 2 which is not seen in the measurements.

On the other hand, for the upstream absorption coefficient, α_a, the model predictions by Aurégan and Kooijman are not in agreement with the measured quantities. The low frequency limit absorption predicted by the model by Aurégan corresponds to the quasi-steady state model, but it predicts an increasing trend of the absorption with increasing Strouhal numbers. The model by Kooijman predicts a quasi-steady state absorption that is too high compared with the models by Boij and Aurégan, but the trend is modelled correctly and the absorption decreases with increasing Strouhal number. The decrease of absorption coefficient with increasing Strouhal number is smaller than the experimentally observed difference. The model predictions by Boij, are qualitatively more in agreement with the observations. The values of the absorption coincide with the values obtained at higher Strouhal numbers. The sudden increase of absorption at Strouhal numbers of around 2 is not clearly seen in the measurement results, but they show a distinct increase in the absorption for the lower Strouhal numbers.

The results from the upstream absorption coefficient hint at the existence of the flow-acoustic interaction. At low Strouhal numbers, the fluid flow can adjust to the acoustic perturbations and the acoustic field loses energy to the hydrodynamic field. On the other hand, at high Strouhal number the hydrodynamic field can not adjust to the fast oscillating

acoustic field. The interaction reduces and less acoustic energy is absorbed and only the convective effects on the sound propagation dominate. Unfortunately the interaction does not lead to large changes in the absorption coefficient and with the current setup it is difficult to reach low Strouhal numbers, leading to results that show quite a bit of scatter for the lower Strouhal numbers.

The difference in the quasi-steady state results of the upstream absorption coefficients between the models of Kooijman and the models by Boij and Aurégan could be the modelling of the mean flow profile. For the model by Kooijman, the model with a fully developed flow profile has been used and the models by Boij and Aurégan both use uniform mean flow profiles.

Apart from the difference in the quasi-steady state, it is interesting to note that the model by Kooijman predicts a dependency of the absorption on the Strouhal number that is less than observed in the measurement data. One explanation of this discrepancy could be the modelling of the shear layer. In the models used by Boij, the shear layer is assumed to be infinitely thin. In the case of the model by Kooijman, the shear layer has finite thickness and Howe [111] has shown that incorporating a finite thickness of the shear layer leads to a lowered effectiveness of the acoustic sound absorption. Another explanation could be the difference in geometry, as the largest difference between the rectangular and circular geometry are seen at the Strouhal numbers corresponding to the transition region between the low and high Strouhal regimes.

It is interesting to see that the observed absorption for waves incident from the downstream side agree well with the models by Kooijman and Aurégan and the difference between the measurements and the model predictions by Boij are large, which could indicate a difference caused by the geometry.

7.5 Conclusion

In this chapter the aero-acoustic interaction at the area expansion has been experimentally determined. The purpose of the investigation is to obtain new experimental data that is accurate enough to validate models. Measurements on an area expansion without flow have been performed to asses the precision and the measurement results are within 1% of the analytical models. The scattering matrices have been determined of an area expansion with an expansion ratio of $\eta = 0.309$ for 5 upstream mean Mach number in the range of 0.05-0.25. The measurement results have been compared with three models from literature with the individual scattering coefficients, the end correction and the absorption coefficients.

The models agree well compared to the experimental accuracy, except for the transmission coefficient from the upstream to the downstream side, where the measurements are

consistently larger than the predicted measurement data. For the absorption coefficients, hints of the existence of flow-acoustic is shown, but the accuracy of the measurement data and the relatively small changes induced by the flow-acoustic interaction inhibits to make definite statements. Each of the models predict different trends for the acoustic absorption coefficients and partially agree with the observations.

For the end-correction, the more intricate models agree well with the measured end correction at high Strouhal numbers. For lower Strouhal numbers, where the flow-acoustic interaction alters the end correction, the measurement scatter is too high to discern these effects clearly.

8

Conclusions and recommendations

The goal of this thesis was to obtain reliable data of the flow-acoustic interaction in the form of scattering matrices, and to achieve that goal the influence of measurement errors on the results had to be assessed. In the introduction, the steps taken to reach that goal have been summarized in four questions and the main conclusions of this thesis are formulated using the research questions.

How can the stochastic error on transfer functions measured with stepped sine excitation be determined?

In chapter two, the stochastic error on measured transfer function is determined with the help of the measured signal that is not associated to the excitation signal. With the synchronous demodulation technique, the deviation from the transfer function as function of the noise is derived in the time domain.

Three models are used to model the noise in the frequency domain and using the models, estimates of the variance and kurtosis are obtained as function of the auto spectral density of the noise. The derived relations are validated against experiments and a good correspondence between the predicted variance and the measured variance is shown for all the models. The kurtosis is only predicted by two models and show a good correspondence with the measured kurtosis.

Furthermore, using the derived expressions, the assumption that the real and imaginary parts are uncorrelated and have the same variance have been investigated. It is shown that the variance on the real and imaginary parts depend on the noise spectrum and the measurement time for a single sample.

Are linear uncertainty analyses appropriate to quantify the stochastic errors on measured scattering matrices?

The validity of the linear uncertainty analysis to determine the uncertainty in the scattering matrix coefficients has been investigated by analyzing the source of non-linearities in the uncertainty analysis. It has been shown that a linear multi-variate analysis can only be used when plane waves are measured and conditions have been derived when such an analysis gives valid information on the uncertainty bounds for the wave decomposition method. For higher order modes, the amount of conditions increases significantly and no general conditions can be formulated when a linear uncertainty analysis can be used. Therefore, to determine accurate uncertainty intervals, a Monte-Carlo method should be used.

The use of an alternative linear method, based on matrix perturbation theory is also investigated. With the method partial condition numbers are obtained for the problem. These partial condition numbers are a computational inexpensive alternative to obtain qualitative information on the measurement quality.

The findings are tested on experimental data of higher order mode measurements. The results show a large variance in the measured reflection coefficients for different excitation conditions. Using the partial condition numbers, it is shown that these difference are caused by the changes in distribution of the modal amplitudes.

Which systematic errors are present in acoustic impedance tubes?

The systematic errors occurring in impedance tubes have been investigated by measuring a calibration standard, defined by a rigid wall. Four error sources have been treated, mechanical vibrations induced by the loudspeakers, the influence of a temperature drift and the finite size of the microphones. The most prominent error source are vibrations induced by the actuator exciting the sound field, which lead to large errors in the measured values and sharp peaks in the determined reflection coefficients. The presence of a temperature drift predominantly affects the phase of the measured reflection coefficient. It has been shown that the determination of the exact acoustic center of the microphone leads to improvements of the results, especially with respect to the measured phase.

After accounting for the identified errors, the measurement results have been analyzed using a linear uncertainty analysis. The observed deviation between the measured amplitude of the reflection coefficient and the calibration standard are significantly larger than

the 95% confidence intervals for the absolute values of the reflection coefficient, indicating that there are still systematic errors present.

The systematic error creates two distinct trends on the measured results. The first trend are oscillations in the measured reflection coefficient and the second trend is a decay of the measured reflection coefficient with increasing frequency, leading to apparent loss of acoustic energy. With the help of a simplified setup, the plausible sources of the oscillations are identified, which are the influence of the microphones on the sound field and the presence of wall vibrations, excited by the sound field in the impedance tube. A simplified analytical model to explain the effect of a finite microphone impedance agrees qualitatively well with the measured data.

For the apparent absorption, several hypotheses have been discussed, including the effect of volumetric losses, the Konstantinov effect and the influence of the acoustic field in the corners where the walls of the waveguide and the rigid wall meet. These hypothesis did not give a convincing explanation and after a literature survey, the most plausible source of error, the imperfect walls of the waveguides is identified.

Do measurements agree with recent predictions of the area-acoustic interaction at an area expansion?

In the last chapter, the aero-acoustic interaction at the area expansion has been experimentally determined. Results have been obtained without flow to asses the precision and the absolute values of the measurement results are within 2% of the absolute value and within 2° of phase angle of the predictions by analytical models. The scattering matrices have been determined of an area expansion with an expansion ratio of $\eta = 0.309$ for 5 upstream mean Mach number in the range of 0.05-0.25. The measurement results have been compared with three models from literature with the individual scattering coefficients, the end correction and the absorption coefficients.

The models agree well compared to the experimental accuracy, except for the transmission coefficient from the upstream to the downstream side, where the measurements are consistently larger than the predicted measurement data. For the absorption coefficients, hints of the existence of flow-acoustic is shown, but the relatively small changes induced by the flow-acoustic interaction and the limited accuracy of the measurement setups inhibits it to make definite statements. Different trends are predicted by the models and they partially agree with the observations.

For the end-correction, the more intricate models agree well with the measured end correction at high Strouhal numbers. For lower Strouhal numbers, where the flow-acoustic interaction alters the end correction, the measurement scatter is too high to discern these effects clearly.

8.1 Recommendations

As always, there is room for improvement and there are many ways to continue the present work. It has been shown for the impedance tube that the measurement precision is much better than the measurement accuracy and in order to significantly improve the measurement results, the systematic errors have to be taken into account into the analysis.

The use of optimization routines to improve the results based on the canonical expressions for acoustic waves in hard walled ducts will only improve the results to a certain extent, as sources of systematic errors that are not captured by the expressions are not taken into account.

In chapter 6 the sources of the systematic errors have been identified, but no satisfactorily model given to take the effect into the measurement routine. One of those systematic errors is the microphone impedance. The influence of the microphone impedance should be taken into account, as it even affects the calibration procedure of the measurement. Furthermore, the measurements of higher order modes are gaining interest, for which a large amount of microphones are used to be able to perform the wave decomposition, which may affect the obtained results. The proposed model is far from complete, as the effect of the excitation of higher order modes are not taken into account and may lead to a substantial influence when the microphone spacing is small.

Another issue is the presence acoustic-structure interaction. This effect is noticeable but not the major error source in the current measurements, however when measuring higher order modes, the used waveguides tend to be larger with similar wall thicknesses and thus less stiff. As the acoustic vibrational pattern changes with the modes and their wave numbers are dispersive, they may coincide with the vibrational pattern of the structural motion of the waveguide, leading to a strong coupling.

CHAPTER 9

Acknowledgements

APPENDIX A ■

Measurement setup

*In this chapter, additional information on the measurement setup used to deter-
mine the aero-acoustic properties of the area-expansion is given. Detailed dimen-
sions are shown, together with the estimation of the uncertainty in the measure-
ments and the measured flow profiles in the setup are shown.*

A.1   Measurement geometry

A schematic of the dimensions of the complete setup is shown in figure A.1, all the measures
are in meters and relative to the positions of the area expansion, denoted with the red arrow,
unless otherwise denoted. The measurement setup is made of aluminium and the pipes have
a wall thickness of 5mm.

A.2   Flow profiles

The flow profiles in the measurement setup have been measured to see whether the assump-
tion of a fully developed flow is justified and how large the error in the determined volumet-
ric flow rate is when using this assumption. In the measurements the Reynolds numbers are
in the order of $\mathrm{Re} = \mathcal{O}(10^4)$, resulting in a turbulent flow.

To determine the profiles, a manually operated traversing mechanism has been attached
to the pipes. It has the possibility to rotate around the axis of the tube to measure at differ-
ent different angles across the pipe cross section. A (static)-pitot tube is attached to the
traversing mechanism to determine the flow velocity at various radii. The measurement
plane lied just outside the exit of the pipes $\mathcal{O}(0.1\mathrm{mm})$ (Fig. A.2). Both the flow profiles at
the downstream pipe and at the upstream pipe have been measured.

Upstream section

Excitation section   Measurement section

Speaker #3   Speaker #2   Speaker #1   Mic #4   Mic #3   Mic #2   Mic #1
2.056   1.591   1.301   0.757   0.587   0.553   0.485

50mm   Flow direction

Pitot-tube   Temp #1
2.165   0.660

1.25   1.06

Downstream section

Measurement section   Excitation section   Muffler

Mic #5   Mic #6   Mic #7   Mic #8
0.433   0.465   0.495   0.680

Flow direction
                                                                        90mm

Temp # 2   Speaker #4
0.470   2.530

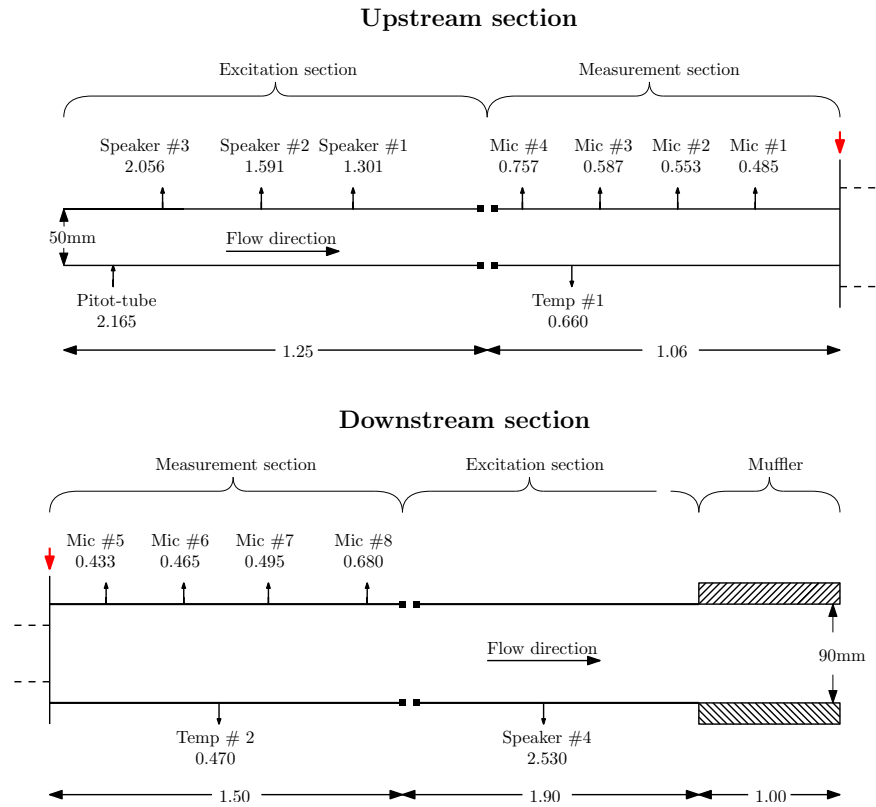1.50   1.90   1.00

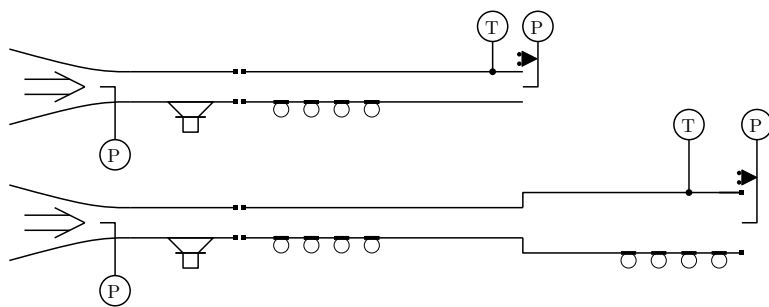**Figure A.1:** *Dimensions of the experimental setup used for the area-expansion measurements*

Figure A.2: *Schematic overview of the setups used to determine the flow profiles.*

The measurement time was much larger (~500 times) than the integral time scale of the flow, the so-called eddy turn over time. The measurement range was constricted to be smaller than the pipe radii minus 1.5 times the tube diameter. If one wants to measure closer to the wall, a correction should be applied which becomes larger than 0.25% of the dynamic pressure [125, chap 3]. Before measuring, the flow is allowed to settle, because measuring immediately after a position change will introduce an error in the measurement value. The time constant of the measurements has been set to 0.5s. Compressibility effects have been included as the highest flow speed measured is around $M \approx 0.3$, leading to a correction of 1% compared to the determined velocities with the incompressible assumption [15]. The flow velocity is calculated using the relation,

$$v = c_0 \sqrt{\frac{2}{\gamma - 1} \left[\left(\frac{p_0}{p_{stat}} \right)^{\frac{\gamma - 1}{\gamma}} - 1 \right]}, \tag{A.1}$$

in which c_0 is the speed of sound in air, γ the specific heat capacity ratio, both determined using the relations from Cramer [65], p_0 the measured stagnation pressure and p_{stat} the static (ambient) pressure.

The flow profiles for the downstream pipe have been measured with a static pitot tube with a diameter of 2.5 mm and three static pressure holes and the profile has been determined 1.5 m downstream of the area expansion equivalent to around 17 pipe diameters. For the upstream pipe a glass pitot-tube has been used with a diameter of 0.1 mm. The flow profile has been measured just at the exit of the upstream pipe, the static pressure has been measured close to the exit of the tube where quiescent conditions were present. The difference between the static and stagnation pressure has been measured with a SWEMA 3000 manometer. The temperature of the flow is monitored via a thermo-couple attached to the outer wall of the pipes and the barometric pressure has been recorded by a BK UZ001 manometer.

The flow profiles of the jet at the area expansion have been measured to determine if the fluid flow is fully developed. In figure A.3 the measured flow profile at the expansion is shown for three flow speeds corresponding to upstream Mach numbers of M $\approx$ 0.03, 0.15 and 0.3. The flow profile on the upstream side shows a good agreement with that of a fully developed turbulent profile obtained from DNS simulations [117] for all measured speeds. The slight asymmetry that is present in the flow is caused by the loudspeakers attached to the pipe. At the loudspeaker position, a pattern of holes has been drilled to be able to excite the sound field, which also influence the hydrodynamic boundary layer and the velocity profile does not fully develop itself before it reaches the area expansion.

In figure A.4 the measured velocity profile at the upstream side is shown for flow speeds corresponding to upstream Mach numbers of M $\approx$ 0.03, 0.15 and 0.3. The results show that
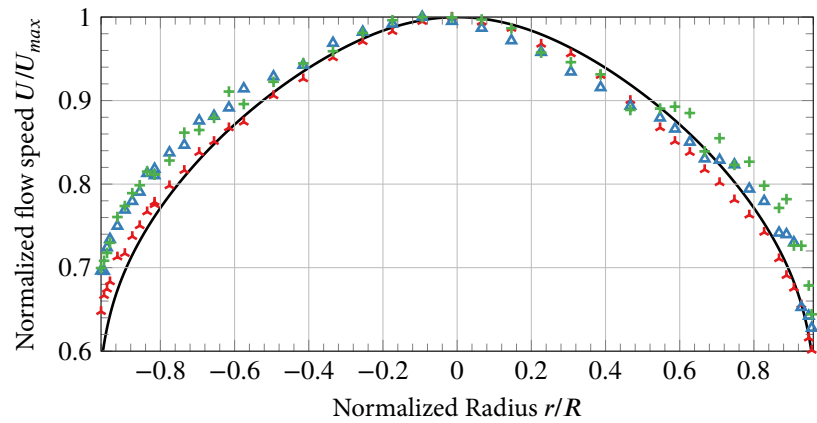
Figure A.3: *Measured flow profile at the area expansion for three flow speeds:(⋌) U$_{max}$ = 10.67 m/s, (△) U$_{max}$ = 57.93 m/s,(+) U$_{max}$ = 105.0 m/s, (———) fully developed profile from DNS modelling (Re = 24 000) [117].*
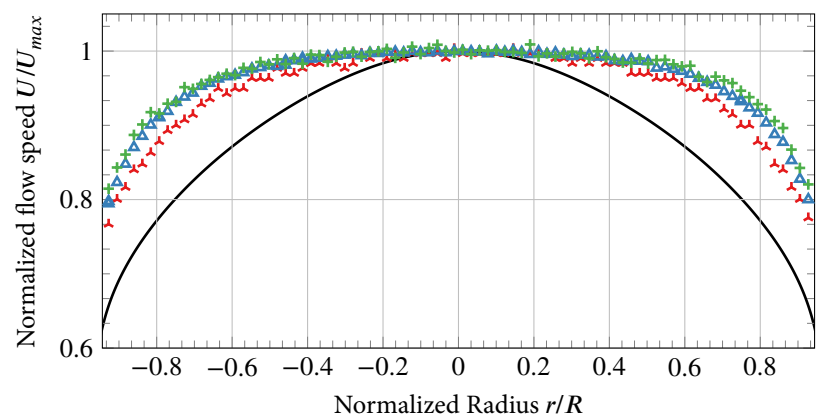
Figure A.4: *Measured flow profile of the downstream pipe for three flow speeds:(⋌) U$_{max}$ = 3.62 m/s, (△) U$_{max}$ = 19.31 m/s,(+) U$_{max}$ = 34.23 m/s, (———) fully developed profile from DNS modelling (Re = 24 000) [117].*

the flow velocity profile of the large pipe is not fully developed for all the measured flow speeds, which can be explained by the close proximity of the measurement plane to the area discontinuity.

A.3 Uncertainty in the measurands

In this section the uncertainty in the measurands is determined. The section follows the guidelines and terminology as those presented in "Guide to the Expression of Uncertainty in Measurement"[126, 127] First the measurement process is defined giving the relation between the measured quantity and the desired quantity. Thereafter the error model is developed by identifying the error sources and the error distributions. The information of the error model is used to determine the sensitivity coefficients and together with the knowledge on the error sources the uncertainty is determined. The uncertainties are presented in the form of the standard uncertainty, which is the square root of the variance, and the data is condensed in the form of tables.

The first part of each table consists of all the known constants needed to determine the uncertainty, i.e. measurement conditions and/or sensitivity components. The middle parts contains the information on the various measurement errors, their distributions, standard uncertainty of each measurand itself, the sensitivity components when the measurand is used to calculate a subject parameter and the component uncertainty of the subject parameter which is the standard uncertainty multiplied with the sensitivity. The last grey line of each table gives the information on the final output value and the uncertainty of this output value.

In the measurements presented in chapter 5, 6 and 7, the following quantities have to be measured: barometric pressure, ambient humidity, ambient temperature, pipe radii, microphone positions, acoustic pressures and flow velocity. In the following part, all these quantities are treated separately and the measurement uncertainty in each measurand is presented.

The sensitivity coefficient depend on the measuring circumstances, i.e. what are the ambient conditions and the measured flow speed. The information presented in this part is with reference to ambient conditions at SATP (25 °C and 100 kPa) and a flow speed of 105 m/s ($\approx$0.3M). The total uncertainty is determined assuming that there are no correlations between the various error sources.

The frequency accuracy of the digital source in the measurement system is $\pm$0.012% [128]. As this error is much smaller than the expected errors from the other sources it is not taken into account into the analysis.

The barometric pressure is measured using a Brüel & Kjær barometer (type UZ 0001), which has a reading accuracy of 2 hPa. The relative humidity is measured with a Brüel & Kjær hygrometer, which has a reading accuracy of 5% RH and the pipe radii are measured using a Vernier calliper. For the three devices, the two common error sources are the operator bias and the resolution error. The resolution error is assumed to have a uniform distribution, a 100% confidence level and the error limits equal to the reading accuracy. The

operator bias is assumed to have a normal distribution with a confidence level of 90% with error limits equal to half of the reading accuracy.

Unfortunately no information is available for the pressure gauge and the hygrometer on the repeatability of the device and there is no calibration history present for all the three devices. Therefore, no statement on other sources of error can be made. The evaluated uncertainty in the determination of the humidity, the ambient pressure and the pipe radii are respectively 4.81% RH and 1.93 hPa and 0.097 mm.

The positions of the microphones have been determined via a fitting procedure described in section 5.3. The determined uncertainty is 0.02% of the mean value. The variance is directly determined from the data fitting procedure and as the estimate is based upon a large number of measurement points, the distribution is assumed to be normal based on the central limit theory.

The temperature is measured using a thermocouple and circuit incorporating an AD595-AQ temperature chip. The output of the circuit has a sensitivity of 10 mV/K and is attached to the VXI system. The resolution error of the VXI system is small compared to the uncertainty of the output and therefore only the uncertainty in the measurand is taken into account. The temperature is measured with a standard uncertainty of 0.0625 °C [58].

The flow velocity is determined by measuring the pressure difference between two ports of a static-pitot tube with a SWEMA 3000 with the SWA07 pressure probe. The identified measurement errors of the determination of the differential pressure are the resolution uncertainty, the reading accuracy of the device and the temperature dependence of the device. Long term effects have been omitted because there is no information on the calibration history. The accuracy of the device is ±0.3% of the read value with a minimum of 0.3Pa. The accuracies stated in the technical documentation have a confidence level of 95% and the probability density function is assumed to be normal. The reading resolution is 0.1Pa with an uniform probability density function and a 100 % confidence interval. The temperature dependence of the probe is 0.2Pa/°C and this source of error is included into the total differential pressure uncertainty.

By determining the first order Taylor expansion of equation (A.1) with respect to the measured parameters, the uncertainty in the flow velocity due to uncertainties in the ambient conditions can be calculated. The previously determined uncertainties in the temperature and the absolute pressure will be used to determine the measurement errors in these quantities.

Error source	Value	Error limits	Conf. level	Error dist.	Estimate type	DOF	Standard uncertainty	Sensitivity coefficient	Component uncertainty
Humidity measurement									
Operator bias		±2.5% RH	90	Normal	B	∞	1.51% RH	1	1.51% RH
Resolution error		±5% RH	100	Uniform	B	∞	2.86% RH	1	2.86% RH
Output	25% RH					∞			3.23% RH
Barometric pressure									
Operator bias		±1 hPa	90	Normal	B	∞	0.61 hPa	1	0.61 hPa
Resolution error		±2 hPa	100	Uniform	B	∞	1.15 hPa	1	1.15 hPa
Output	100 kPa					∞			1.30 hPa
Temperature									
Calibration error					A	5	0.0675 ˚C	1	0.0675 ˚C
Output	25 ˚C					5			0.0675 ˚C
Pipe diameter									
Operator bias		±0.05 mm	90	Normal	B	∞	30.4 μm	1	30.4 μm
Resolution error		±0.10 mm	100	Uniform	B	∞	57.7 μm	1	57.7 μm
Output	50 mm / 90 mm					∞			65.2 μm
Flow velocity									
Nominal temperature	25 ˚C					5	0.0675 ˚C	176.2 mm/sK	11.89 mm/s
Nominal ambient pressure	100 kPa					∞	1.39 hPa	0.26 mm/sPa	36.51 mm/s
Nominal pressure difference	6450 Pa								
Accuracy	±0.3% min 0.3 Pa [129]	±23.19 Pa	95	Normal	B	∞	11.81 Pa	8.14 mm/sPa	96.29 mm/s
Resolution error		±0.1 Pa	100	Uniform	B	∞	58.7 mPa	7.39 mm/sPa	0.433 mm/s
Temperature dependence	0.2 Pa/˚C [129]								
Temperature error						∞	0.0675 ˚C	0.32 mm/sK	0.022 mm/s
Output	105 m/s					11			103.6 mm/s

Table A.1: *Measurement process uncertainties for various variables at SATP and a flow speed of 105 m/s.*

The acoustic pressure is measured by a chain of devices. It consists of a type 4938 BK (Brüel & Kjær) condenser microphone cartridge attached to a type 2670 BK pre-amplifier. The output of the pre-amplifier is attached to a BK Nexus signal conditioning amplifier and the signals are recorded by a Hewlett Packard 1432A data acquisition card inside a VXI mainframe.

To evaluate the uncertainty in the complete measurement chain of the acoustic pressure, the uncertainty in each module has to be calculated and the uncertainties of the previous modules have to be propagated until the final output is reached. In the following parts, each module is treated separately and the information about the error sources is given for each module. The information is summarized in table A.2.

The microphones are calibrated relatively to each other by exposing them to the same sound field. The repeatability of this calibration gives information about the random error present in the measurement chain such as internal noise. Such a calibration can be seen as the microphones are calibrated against an ideal reference which has no bias error associated with it [127, sec. 8.4]. The repeatability of the measurement process is determined by performing the calibration several times over a short period (2 days). The repeatability of the total measurement chain is included as an error source in the VXI system. The determined variance of the repeatability is lower than the discretization error of the VXI system, showing that the output of the microphones is very stable.

The microphone cartridge together with the pre-amplifier is considered as a complete measurement module. The relation between the input (acoustic pressure p_{ac}) and output (voltage U_{mc}) of the microphone is given by

$$U_{mc} = S_{mc} \cdot p_{ac}, \tag{A.2}$$

where S_{mc} is the sensitivity of the microphone cartridge.

The error sources for the microphone cartridge are identified from the technical data sheet and these errors are related to temperature variations and ambient pressure variations. The influence of the humidity is not taken in to account as it is negligible [130]. Furthermore the influence of electro-magnetic fields and vibrations have been omitted. The effect of flow noise is not evaluated as an error source in the microphone cartridge but as an error source at the VXI output as the flow noise is an integral part of the measurand itself.

Introducing the various error sources, the relationship between input and output can be written as

$$U_{mc} = \left[S_{mc} + S_t \Delta T + S_{p_{amb}} \Delta p_{amb} \right] p_{ac}, \tag{A.3}$$

where S_t is the temperature dependence of the microphone sensitivity, ΔT the temperature difference relative to the calibration temperature, $S_{p_{amb}}$ the dependence of the microphone

sensitivity on the ambient pressure and Δp_{amb} the difference in ambient pressure relative to the calibration conditions.

The microphones are calibrated relatively to each other and therefore the environmental influence on the measured pressures depends on the environmental conditions during the calibration. After the calibration, the measured values are not compensated for the ambient variations, leading to an additional biased error source due to changes in the ambient parameters. To determine the uncertainty in the microphone output, a first order Taylor expansion is made of equation (A.3) giving rise to,

$$\epsilon_{U_{mc}} = S_t p_{ac} \epsilon_T + S_{p_{amb}} p_{ac} \epsilon_{p_{amb}}, \tag{A.4}$$

wherein ϵ_T the error in the temperature and $\epsilon_{p_{amb}}$ the error in ambient pressure. The difference in the temperature at calibration and the temperature during the measurements is assumed to be within 2 ˚C with an associated 95% confidence limit with normal distribution. The error limits of the absolute pressure is assumed to be 100Pa with an associated 95% confidence limit and normal distribution. The inherent noise from the microphone cartridge and pre-amplifier is assumed to have a normal distribution with a 99% confidence interval. In this analysis an acoustic pressure amplitude p_{ac} of 1Pa,corresponding to 94 dB, is used to calculate the sensitivity coefficients. Assuming that there are no correlations between the error sources, the uncertainty of the output of the microphone is calculated to be 1.6mV $\pm$ 2.83μV.

The microphone is connected to a Nexus signal conditioning system which amplifies the measured input from the microphone cartridge. In this analysis the amplification is assumed to be equal to 62.5, such that the output will have a response of 100mV/Pa. The associated errors with this device is the harmonic distortion of the output signal caused by the amplification. The error sources is assumed to be normal distributed and the error limits fall within a 99% confidence interval. The amplitude accuracy and channel to channel phase match of the Nexus system are not taken into account as these error sources are assumed to be bias errors which are accounted for during the calibration procedure. By determining the error model and applying the error sources the uncertainty in the output of the Nexus system is calculated to be 100mV $\pm$ 0.109mV

The last module in the measurement chain is the data acquisition system, consisting of a VXI-mainframe with an HP1432A data acquisition module (DAQ). The DAQ stores the information digitally and thus there is a resolution error associated with this process. The resolution error of the VXI system depends on the measurement range of the chosen channels. During the measurement procedure the channels are auto-ranged to have the optimum range for the measurement. For this case, the measuring range is set to 2V, the lowest range available to the VXI system.

The repeatability of the calibration process is used to evaluate the random error, not induced by the flow noise, of the measured pressures. It is assumed that the short term variations in the channel to channel phase match and the amplitude accuracy of both the Nexus system and the DAQ are taken into account in this type A error source. The measured values are complex quantities and therefore the uncertainty has been determined as the frequency averaged deviation of the absolute value of the measured transfer function from its mean value. This definition assumes that the uncertainties in the real and imaginary parts are equal and uncorrelated. The associated degree of freedom of this estimate is $v = N - 1$, where N is the number of frequencies used to determine the calibration . The calibration data that is obtained from the calibration process is a relative quantity and therefore the obtained uncertainty has to be multiplied with the magnitude of the pressure signal to obtain the real measurement uncertainty.

Error source	Value	Error limits	Conf. level	Error dist.	Estimate type	DOF	Standard uncertainty	Sensitivity coefficient	Component uncertainty
Microphone Cartridge									
Acoustic pressure	1 1Pa								
Microphone sensitivity	1.6 mV/Pa [131]								
Temperature coefficient	0.003 dB/K [131]								
Atm Pressure coefficient	−0.003 dB/kPa [131]								
Temperature error		±5 ˚C	95%	Normal	B	∞	2.55 ˚C	1.106 μV/PaK	2.82 μV
Atm pressure error		±5 hPa	95%	Normal	B	∞	2.55 hPa	−1.106 μV/PakPa	0.28 μV
Output	1.6 mV					∞			2.83 μV
Nexus									
Input	1.6 mV					∞	2.83 μV	62.5	0.177 mV
Signal amplification	62.5								
Harmonic distortion		< 0.003% [132]	99%	Normal	B	∞	1.16 μV	1	1.16 μV
Output	100 mV					∞			0.109 mV
HP1432A									
Input	100 mV					∞		1	0.109 mV
Resolution	16bit [133]	±0.153 mV	100%	Uniform	B	∞	17.6 μV	1	17.6 μV
Repeatability amplitude				Normal	A	6600	0.99 μV	1	0.99 μV
Output	100 mV					∞			0.1104 mV

Table A.2: *Measurement process uncertainty for the acoustic pressure at SATP and a flow speed of 105 m/s.*

Measurement methods

In this chapter the procedures to obtain the experimental data are clarified. The first part introduces the measurement routine. Thereafter the signal processing, to determine the statistical parameters on the measurements is introduced. The chapter concludes with the concept of the widely linear minimum variance unbiased estimator.

B.1   Measurement routine

To obtain accurate measurements, several calibrations have to be performed before the actual measurement is conducted. In figure B.1 the flow chart of the measurements is given.

The microphones are calibrating by exposing them to an equal sound field in a calibrator and the transfer functions w.r.t. an arbitrary microphone are calculated [63]. These transfer functions are used to adjust the measured complex pressures. The microphones have been calibrated at distinct pressure with a stepped sine measurement procedure and controlling the amplitude of excitation. This procedure has been repeated 5 times to check short term repeatability and finally averaged to obtain the calibration data.

The second step is to experimentally determine the microphone positions. First the ambient conditions are noted and then a stepped sine excitation is used as an excitation source. The amplitude of the incident sound wave is iteratively adjusted to a specified value by performing the wave decomposition and adjusting the source level prior to measuring. Thereafter the pressures at the microphone positions are measured for a predetermined time together with the temperature. The microphone positions are then fitted to the measurement data to obtain the best agreement with an analytical model computing the wave-numbers
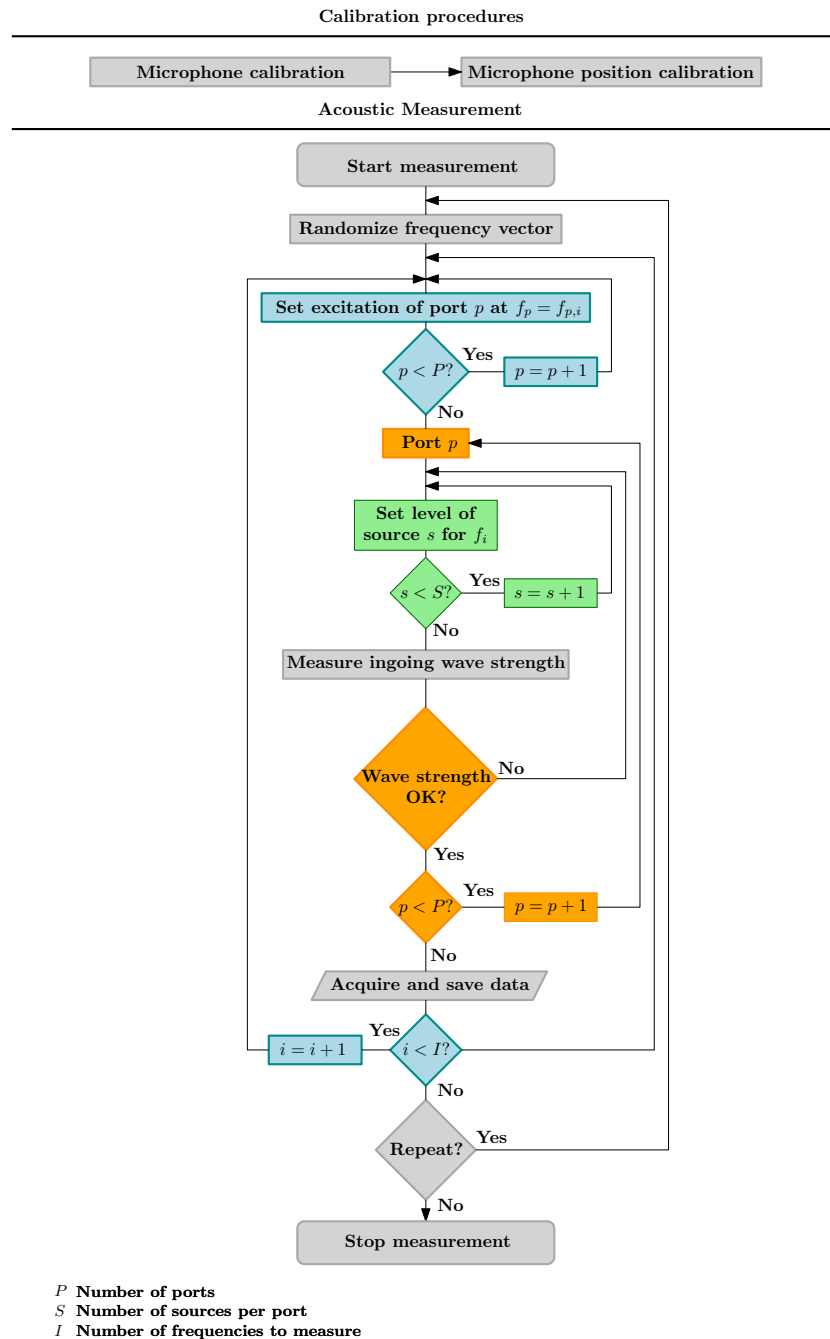
Figure B.1: *Flowchart of the acoustic measurements on the area expansion.*

for each frequency using the ambient data and the measurement temperature. This method is described in more detail in section 5.3.

The actual measurement is conducted in a similar manner, first the ambient conditions are measured and thereafter an excitation is applied. An excitation is applied at both sides of the error expansion, with different frequencies at each side of the expansion. The incoming wave strength for each side is iteratively adjusted to a specified value and when the amplitudes reach the desired levels, the time signals are recorded for a pre-specified time. The transfer function between the excitation source and the measured signal at the microphones is obtained using the synchronous demodulation technique, as explained in chapter 2. The signal processing to determine the statistical estimates will be explained in the next section.

B.2 Signal analysis

Statistical estimates

Using the time dependent transfer function, the statistical quantities of the transfer function can be obtained by measuring the transfer function at different times and determining the statistical parameters of the real and imaginary part of the transfer function.

To determine the statistical parameters, consider a vector of observed transfer functions at a specific time, obtained with the synchronous demodulation technique,

$$\boldsymbol{H} = \begin{bmatrix} H_1 \dots H_n \dots H_N \end{bmatrix},$$
(B.1)

The expected value of the transfer functions is given by

$$H_\mu = \mathrm{E}\left[\boldsymbol{H}\right],$$
(B.2)

where the expectation operator is taken over multiple observations. The covariance matrix is then given by,

$$\mathrm{Cov}\left[H\right] = \mathrm{E}\left[\left(\Re\left[\boldsymbol{H} - H_\mu\right]\right)\left(\Im\left[\boldsymbol{H} - H_\mu\right]\right)^T\right],$$
(B.3)

which gives information on the variance of the real and imaginary part of each transfer function and the correlation between the real and imaginary parts of the N measured transfer functions.

To determine the covariance matrix, the samples have to be statistically independent from each other. When performing measurements under flow conditions, the flow is a major source of noise. This noise is caused by large and small scale flow structures that induce hydrodynamic pressure fluctuations that are recorded by the microphones. Consequently,

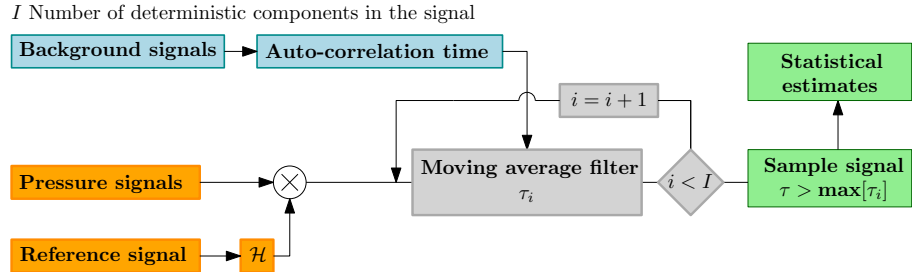I Number of deterministic components in the signal

Figure B.2: *A schematic overview of the signal processing used to obtain the transfer functions between the acoustic source and the measured acoustic pressures and their statistical parameters.*

when the flow structures are large, the measured pressure perturbations will have a finite correlation time. The correlation time of the flow is determined by measuring the pressure fluctuations and determining the autocorrelation time of the signal. The autocorrelation time is determined by measuring the time it takes for the scaled autocorrelation function to be smaller then 0.05.

Furthermore, multiple frequencies are excited during the measurements and the measured signals consists of multiple tones. As these parts are deterministic, they have to be filtered away to obtain unbiased estimates. After applying the synchronous demodulation, the tones not associated with the used reference signal will also create slow and fast oscillating parts (2.4). The frequencies of these parts are given by the difference and sum of the frequency of the tone and the reference frequency, and have to be filtered away using the appropriate integration time.

When all deterministic parts have been filtered away, the resulting signal can be sampled at times larger then the integration times of the used filter, to obtain uncorrelated samples. A flow chart of the signal processing is shown in figure B.2.

B.3 Widely linear minimum variance unbiased estimator

To decompose the acoustic field, the inverse relation between the acoustic field and the modal amplitudes, (3.62), has to be determined. The inverse problem can be seen as the regression of a linear model on observations, which is extensively used in statistics. The linear system is given by,

$$\boldsymbol{A}\boldsymbol{x} = \boldsymbol{b}, \tag{B.4}$$

where $\boldsymbol{A}$ is the model, $\boldsymbol{x}$ are the vector of model parameters and $\boldsymbol{b}$ the vector of observations. As there are more observations then unknowns, the solution to the system is not

unique. One often used estimator of the modal amplitudes is obtained by pre-multiplying the measured pressures with the Moore-Penrose pseudo inverse, which obtains the linear least square estimator for the modal amplitudes. The linear least square estimator makes assumptions on the errors on the model and the observations. The first assumption is that the model itself is true, secondly the errors on observations are assumed to have the same variance, are normally distributed and are uncorrelated with each other. If the above assumptions are not full-filled, the model coefficients will have a bias.

In general, some of these assumptions are violated when there is a flow present. As will be shown in chapter 2 the variance on the real and imaginary part of the measured transfer functions do not have to be the same and is dependent on the background spectrum. Furthermore, the variance of the measured transfer function is caused by the flow-noise. A part of this unwanted signal is caused by large scale flow structures that induce a hydrodynamic pressure at the microphones. When the length scale of these flow structures is in the order of, or larger than the microphone separation distance, the unwanted signal will be correlated between the microphone positions.

On the other hand, it can be shown that the error on the measured transfer functions can be approximated to be normally distributed, when the integration time is long enough (Chap. 2). The bias induced due the cross-correlation between the error sources can be taken into account, with a weighted estimator such as the generalized least squares solution. As the model (3.62) is given in the complex domain, some extra considerations have to be taken into account to obtain an estimator which takes into account the presence of correlated noise.

A complex number can be represented by two real numbers, but a relationship between two complex numbers is fundamentally different when the relationship is the complex domain or in the two-dimensional real space [46]. This can be appreciated by considering the $\mathbb{C}$ linear relationship between two complex scalars, $x = u + iv$ and $y = a + ib$, where i is the imaginary unit, is given by

$$y = kx. \tag{B.5}$$

This relation can be represented by a linear system of equations relating the real and imaginary part of x and y,

$$\begin{bmatrix} a \\ b \end{bmatrix} = \begin{bmatrix} \Re[k] & -\Im[k] \\ \Im[k] & \Re[k] \end{bmatrix} \begin{bmatrix} u \\ v \end{bmatrix}, \tag{B.6}$$

on the other hand, a general transformation on $\mathbb{R}^2$ is given by,

$$\begin{bmatrix} a \\ b \end{bmatrix} = \begin{bmatrix} M_{11} & M_{12} \\ M_{21} & M_{22} \end{bmatrix} \begin{bmatrix} u \\ v \end{bmatrix}, \tag{B.7}$$

where the elements of $\boldsymbol{M}$ can be freely chosen. The complex equivalent of the general transformation (B.7), called the widely linear transformation, is represented in the complex domain by using the complex conjugate, denoted by $\square^*$,

$$y = k_1 x + k_2 x^*. \tag{B.8}$$

Therefore, to obtain general results that both hold in $\mathbb{R}^{2n}$ and $\mathbb{C}^n$, the system of equations have to be represented using the equations and their complex conjugates. To do so, the augmented vector is introduced,

$$\underline{\boldsymbol{x}} = \begin{bmatrix} x \\ x^* \end{bmatrix}, \quad \underline{\boldsymbol{y}} = \begin{bmatrix} y \\ y^* \end{bmatrix}. \tag{B.9}$$

and the widely linear transformation can be represented with,

$$\underline{\boldsymbol{y}} = \underline{\boldsymbol{K}}\boldsymbol{x}, \quad \underline{\boldsymbol{K}} = \begin{bmatrix} k_1 & k_2 \\ k_1^* & k_2^* \end{bmatrix}. \tag{B.10}$$

Using the above representation, the linear system (B.4) is given by,

$$\underline{\boldsymbol{A}}\boldsymbol{x} + \underline{\boldsymbol{n}} = \underline{\boldsymbol{b}}. \tag{B.11}$$

The unbiased estimator of the above augmented linear system, the widely linear minimum variance unbiased estimator, or in statistics language the Best Linear Unbiased Estimator (BLUE), is given by,

$$\hat{\underline{\boldsymbol{x}}} = \left(\underline{\boldsymbol{A}}^H \underline{\boldsymbol{R}}_{nn}^{-1} \underline{\boldsymbol{A}}\right)^{-1} \underline{\boldsymbol{A}}^H \underline{\boldsymbol{R}}_{nn}^{-1} \underline{\boldsymbol{y}}. \tag{B.12}$$

in which $\underline{\boldsymbol{R}}_{nn}$ is the augmented covariance matrix of $\boldsymbol{n}$. The above formulation is analogous to the standard best linear unbiased estimated for linear systems in the real domain, the general linear least squares [45]. The augmented covariance matrix is given by,

$$\underline{\boldsymbol{R}}_{nn} = \mathrm{E}\left[\left(\underline{\boldsymbol{n}} - \underline{\boldsymbol{\mu}}_n\right)\left(\underline{\boldsymbol{n}} - \underline{\boldsymbol{\mu}}_n\right)^H\right]. \tag{B.13}$$

Using the signal processing as explained in the previous section, the augmented covariance matrix can be obtained and the widely linear minimum variance unbiased estimator of (3.62) can be determined.

It should be noted that when including the statistical information of the added noise into the model formulation, the linear least squares method becomes sensitive to errors in the (augmented) covariance matrix and enough samples have to be taken to ensure that the measured covariance matrix is representative for the problem and that the errors are normally distributed [134]. If this not the case, the obtained results can fall outside the confidence intervals of the observations when strong correlations are present [135–138].

Bibliography

[1]   *Burden of disease from environmental noise. Quantification of healthy life years lost in Europe.* World Health Organization, 2011.

[2]   The European Parliament and Council. „Decision No 1386/2013/EU. on a General Union Environment Action Programme to 2020 'Living well, within the limits of our planet'". In: *Official Journal of the European Union* (2013).

[3]   M. J. Lighthill. „On Sound Generated Aerodynamically. I. General Theory". In: *Proceedings of the Royal Society A: Mathematical, Physical and Engineering Sciences* 211.1107 (Mar. 1952), pp. 564–587.

[4]   S. Sack and M. Åbom. „On acoustic multi-port characterisation including higher order modes". In: *Acta Acustica united with Acustica* 102.5 (Sept. 2016), pp. 834–850.

[5]   Todd Schultz, Mark Sheplak, and Louis N. Cattafesta III. „Uncertainty analysis of the two-microphone method". In: *Journal of sound and vibration* 304 (2007), pp. 91–100.

[6]   Lin Zhou and Hans Bodén. „A systematic uncertainty analysis for liner impedance eduction technology". In: *Journal of Sound and Vibration* 356 (Nov. 2015), pp. 86–99.

[7]   Julius S. Bendat and Allan G. Piersol. *Engineering Applications of Correlation and Spectral Analysis, 2nd Edition.* Wiley-Interscience, 1993.

[8]   H. Van der Auweraer et al. „Accurate modal analysis measurements with programmed sine wave excitation". In: *Mechanical Systems and Signal Processing* 1.3 (July 1987), pp. 301–313.

[9]   R. Pintelon, Y. Rolain, and W. Van Moer. „Probability density function for frequency response function measurements using periodic signals". In: *Proceedings of the 19th IEEE Instrumentation and Measurement Technology Conference* (2002).

[10]   Todd Schultz, Mark Sheplak, and Louis N. Cattafesta. „Application of multivariate uncertainty analysis to frequency response function estimates". In: *Journal of Sound and Vibration* 305.1-2 (Aug. 2007), pp. 116–133.

[11]   Michael Feldman. „Hilbert transform in vibration analysis". In: *Mechanical Systems and Signal Processing* 25.3 (Apr. 2011), pp. 735–802.

Bibliography

[12]   S. O. Rice. „Mathematical analysis of random noise". In: *Bell System Technical Journal* 23.3 (July 1944), pp. 282–332.

[13]   Allan D. Pierce. *Acoustics: an introduction to its physical principles and applications*. Acoustical Society of America, 1994.

[14]   S.W. Rienstra and A. Hirschberg. *An introduction to acoustics*. July 2012.

[15]   John D. Anderson. *Modern Compressible Flow: With Historical Perspective*. McGraw-Hill Science/Engineering/Math, 2002.

[16]   L. Fritsche. „Theorie des akustischen Zylinderresonators unter Berücksichtigung der Schallanregung (II)". In: *Acustica* (1960).

[17]   M. Thiesen. „Zur Theorie des geschlossenen Resonators". In: *Annalen der Physik* 329.13 (1907), pp. 401–438.

[18]   Sjoerd W. Rientsra. *Fundamentals of duct acoustics*. 2015.

[19]   L. J. Eriksson. „Higher order mode effects in circular ducts and expansion chambers". In: *Journal of the acoustical society of america* 68 (1980), pp. 545–550.

[20]   Chenyang Weng, Susann Boij, and Ardeshir Hanifi. „On the calculation of the complex wavenumber of plane waves in rigid-walled low-Mach-number turbulent pipe flows". In: *Journal of Sound and Vibration* 354 (Oct. 2015), pp. 132–153.

[21]   Chenyang Weng and Friedrich Bake. „An analytical model for boundary layer attenuation of acoustic modes in rigid circular ducts with uniform flow". In: *Acta Acustica united with Acustica* 102.6 (Nov. 2016), pp. 1138–1141.

[22]   Ralph E. Beatty. „Boundary layer attenuation of higher order modes in rectangular and circular tubes". In: *Journal of the Acoustical Society of America* 22.6 (1950), p. 850.

[23]   G. Kirchhoff. „Über den Einfluss der Wärmeleitung in einem Gase auf die Schallbewegung". In: *Annalen der Physik und Chemie* 210.6 (1868), pp. 177–193.

[24]   Marten Nijhof. „Viscothermal Wave Propagation". Phd thesis. University of Twente, 2010.

[25]   Chenyang Weng et al. „Experimental investigation of sound field decomposition with higher order modes in rectangular ducts". In: *22nd AIAA/CEAS Aeroacoustics Conference*. American Institute of Aeronautics and Astronautics (AIAA), May 2016.

[26]   E. Dokumaci. „Sound transmission in narrow pipes with superimposed uniform mean flow and acoustic modelling of automobile catalytic converters". In: *Journal of Sound and Vibration* 182.5 (May 1995), pp. 799–808.

[27]   Erkan Dokumaci. „On the effect of viscosity and thermal conductivity on sound propagation in ducts: A re-visit to the classical theory with extensions for higher order modes and presence of mean flow". In: *Journal of Sound and Vibration* 333.21 (Oct. 2014), pp. 5583–5599.

[28]   C. Ahrens and D. Ronneberger. „Luftschalldämpfung in turbulent durchströmten, schallharten Rohren bei verschiedenen Wandrauhigkeiten". In: *Acustica* (1971).

[29] Chenyang Weng. „Theoretical and numerical studies of sound propagation in low-Mach-number duct flows". PhD thesis. Kungliga Tekniska Högskolan, 2015.

[30] R.B. Marks and D.F. Williams. „A general waveguide circuit theory". In: *Journal of Research of the National Institute of Standards and Technology* 97.5 (1992), pp. 533–562.

[31] Ernest S. Kuh and R.A. Rohrer. *Theory of linear active networks*. Holden-Day Inc., 1967.

[32] Carl Gerhold, Randolph Cabell, and Martha Brown. „Development of an experimental rig for investigation of higher order modes in ducts". In: *12th AIAA/CEAS Aeroacoustics Conference (27th AIAA Aeroacoustics Conference)*. American Institute of Aeronautics and Astronautics (AIAA), May 2006.

[33] Stefan Sack et al. „Generation and scattering of acoustic modes in ducts with flow". In: *20th AIAA/CEAS Aeroacoustics Conference* (June 2014).

[34] Chenyang Weng. „Modeling of sound-turbulence interaction in low mach number duct flows". Licentiate Thesis. Royal institute of Technology Stockholm Sweden, 2013.

[35] Mats Åbom and Hans Bodén. „Error analysis of two-microphone measurements in ducts with flow". In: *Journal of the Acoustical Society of America* 83 (1988), pp. 2429–2438.

[36] Hans Bodén. „Influence of errors on the two-microphone method for measuring acoustic properties in ducts". In: *The Journal of the Acoustical Society of America* 79.2 (1986), pp. 541–549.

[37] H.Hudde and U. Letens. „Untersuchung zum akustischen Meßleitverfahren mit festen Meßorten". In: *Acustica* 56.4 (1984), pp. 258–268.

[38] Brian F. G. Katz. „Acoustic absorption measurement of human hair and skin within the audible frequency range". In: *The Journal of the Acoustical Society of America* 108.5 (2000), pp. 2238–2242.

[39] René Boonen et al. „Calibration of the two microphone transfer function method with hard wall impedance measurements at different reference sections". In: *Mechanical Systems and Signal Processing* 23.5 (July 2009), pp. 1662–1671.

[40] Paul Dickens, John Smith, and Joe Wolfe. „Improved precision in measurements of acoustic impedance spectra using resonance-free calibration loads and controlled error distribution". In: *The Journal of the Acoustical Society of America* 121.3 (2007), pp. 1471–1481.

[41] Vincent Gibiat and Franck Laloë. „Acoustical impedance measuremetns using the two microphone three calibration method." In: *Journal of the acoustical society of america* 88 (1990), p. 2533.

[42] Takao Suzuki and Benjamin J. Day. „Comparative study on mode-identification algorithms using a phased-array system in a rectangular duct". In: *Journal of Sound and Vibration* 347 (July 2015), p. 2745.

[43] Hugh W. Coleman and W. Glenn Steele. *Experimentation, Validation, and Uncertainty Analysis for Engineers*. Wiley, 2009.

Bibliography

[44] J. Lavrentjev and M. Åbom. „Characterization of fluid machines as acoustic multi-port source". In: *Journal of Sound and Vibration* 197.1 (Oct. 1996), pp. 1–16.

[45] Richard A.Johnson and Dean W. Wichern. *Applied Multivariate Statistical Analysis*. 2007.

[46] Peter J. Schreier and Louis L. Scharf. *Statistical Signal Processing of Complex-Valued Data*. Cambridge University Press (CUP), 2009.

[47] Travis V. Anderson and Christopher A. Mattson. „Propagating skewness and kurtosis through engineering models for low-cost, meaningful, nondeterministic design". In: *Journal of Mechanical Design* 134.10 (2012), p. 100911.

[48] B.D. Hall. *Note on complex measurement uncertainty - part 1*. Tech. rep. Measurement standards laboratory of New Zealand, 2010.

[49] G. W. Stewart and Ji-Guang Sun. *Matrix Perturbation Theory*. ACADEMIC PR INC, 1990. 374 pp.

[50] Assem Deif. *Sensitivity Analysis in Linear Systems*. Springer, 1986. 240 pp.

[51] A. J. Geurts. „A contribution to the theory of condition". In: *Numerische Mathematik* 39.1 (Feb. 1982), pp. 85–96.

[52] Mario Arioli, Marc Baboulin, and Serge Gratton. „A Partial Condition Number for Linear Least Squares Problems". In: *SIAM Journal on Matrix Analysis and Applications* 29.2 (Jan. 2007), pp. 413–433.

[53] Marc Baboulin et al. „Computing the conditioning of the components of a linear least-squares solution". In: *Numerical Linear Algebra with Applications* 16.7 (July 2009), pp. 517–533.

[54] S. Gratton. „On the condition number of linear least squares problems in a weighted Frobenius norm". In: *BIT Numerical Mathematics* 36.3 (Sept. 1996), pp. 523–530.

[55] Per-Åke Wedin. „Perturbation theory for pseudo-inverses". In: *BIT* 13.2 (June 1973), pp. 217–232.

[56] S. Chandrasekaran and I. C. F. Ipsen. „On the Sensitivity of Solution Components in Linear Systems of Equations". In: *SIAM Journal on Matrix Analysis and Applications* 16.1 (Jan. 1995), pp. 93–112.

[57] Philip McCord Morse and K. U. Ingard. *Theoretical Acoustics*. Princeton University Press, Jan. 1, 1987. 949 pp.

[58] L.B.W. Peerlings. „Methods and techniques for precise and accurate in-duct aero-acoustic measurements". Licentiate Thesis. Kungliga Tekniska Högskolan Stockholm, 2015.

[59] Stefan Busse-Gerstengarbe et al. „Comparative Study of Impedance Eduction Methods, Part 1: DLR Tests and Methodology". In: *19th AIAA/CEAS Aeroacoustics Conference*. American Institute of Aeronautics and Astronautics (AIAA), May 2013.

[60] D. F. Williams, C. M. Wang, and U. Arz. *In-Phase/Quadrature Covariance-Matrix Representation of the Uncertainty of Vectors and Complex Numbers*. Tech. rep. National Institute of Standards and Technology, 2004.

[61] P.E. Doak. „Excitation, transmission and radiation of sound from source distributions in hard-walled ducts of finite length (I): The effects of duct cross-section geometry and source distribution space-time pattern". In: *Journal of Sound and Vibration* 31.1 (Nov. 1973), pp. 1–72.

[62] P.E. Doak. „Excitation, transmission and radiation of sound from source distributions in hard-walled ducts of finite length (II): The effects of duct length". In: *Journal of Sound and Vibration* 31.2 (Jan. 1973), pp. 137–174.

[63] G. Krishnappa. „Cross-spectral method of measuring acoustic intensity by correcting phase and gain mismatch errors by microphone calibration". In: *The Journal of the Acoustical Society of America* 69.1 (1981), p. 307.

[64] Brian F. G. Katz. „Method to resolve microphone and sample location errors in the two-microphone duct measurement method". In: *The Journal of the Acoustical Society of America* 108.5 (2000), pp. 2231–2237.

[65] Owen Cramer. „The variation of the specific heat ratio and the speed of sound in air with temperature, pressure, humidity, and CO_2 concentration". In: *The Journal of the Acoustical Society of America* 93.5 (1993), pp. 2510–2516.

[66] R. D. Fay. „Attenuation of Sound in Tubes". In: *Journal of the Acoustical Society of America* 10.3 (1939), p. 259.

[67] Thomas Lavergne et al. „Dynamic behavior of the circular membrane of an electrostatic microphone: Effect of holes in the backing electrode". In: *The Journal of the Acoustical Society of America* 128.6 (Dec. 2010), pp. 3459–3477.

[68] Dorel Homentcovschi and Ronald N. Miles. „An analytical-numerical method for determining the mechanical response of a condenser microphone". In: *The Journal of the Acoustical Society of America* 130.6 (Dec. 2011), pp. 3698–3705.

[69] J. Han, D.W. Herrin, and A.F. Seybert. „Accurate measurement of small absorption coefficients". In: *23rd International Congress on Sound & Vibration*. 2007.

[70] Francesco Taddei et al. „Setup of a test rig for the characterization of devices for acoustic measurements in hot flow". In: *23rd International congress on sound and vibration*. 2016.

[71] W. P. Mason. „The Propagation Characteristics of Sound Tubes and Acoustic Filters". In: *Physical Review* 31.2 (Feb. 1928), pp. 283–295.

[72] E. von Waetzmann and W. Wenke. „Schalldämpfung in Rohren und Schlauchen". In: *Akustische Zeitung* 1 (1939), pp. 1–9.

[73] Leo L. Beranek. „Precision Measurement of Acoustic Impedance". In: *Journal of the Acoustical Society of America* 12.1 (1940), p. 3.

[74] P. S. H. Henry. „The tube effect in sound-velocity measurements". In: *Proceedings of the Physical Society* 43.3 (1931), p. 340.

Bibliography

[75]   D.E. Weston. „The Theory of the Propagation of Plane Sound Waves in Tubes". In: *Proceedings of the Physical Society. Section B* 66.8 (Aug. 1953), pp. 695–709.

[76]   D.E. Weston and I.D. Campbell. „Experiments on the Propagation of Plane Sound Waves in Tubes I: The Adiabatic Region: II: The Transition Region". In: *Proceedings of the Physical Society. Section B* 66.9 (Sept. 1953), pp. 769–774.

[77]   H. Roesler. „Der Zylinderresonator für Präzisionsmessungen der Schallabsorption in Gasen". In: *Acustica* 17 (1966).

[78]   M.C.A.M. Peters et al. „Damping and reflection coefficient measurements for an open pipe at low Mach and low Helmholtz numbers". In: *Journal of Fluid Mechanics* 256 (1993), pp. 499–534.

[79]   L. B. Evans. „Atmospheric Absorption of Sound: Theoretical Predictions". In: *Journal of the Acoustical Society of America* 51.5B (1972), p. 1565.

[80]   H. E. Bass. „Atmospheric absorption of sound: Update". In: *Journal of the Acoustical Society of America* 88.4 (1990), p. 2019.

[81]   H. E. Bass. „Atmospheric absorption of sound: Further developments". In: *Journal of the Acoustical Society of America* 97.1 (1995), p. 680.

[82]   Allan J. Zuckerwar. „Low-frequency absorption of sound in air". In: *Journal of the Acoustical Society of America* 78.3 (1985), p. 946.

[83]   Allan J. Zuckerwar. „Resonant tube for measurement of sound absorption in gases at low frequency/pressure ratios". In: *Journal of the Acoustical Society of America* 68.1 (1980), p. 218.

[84]   F.F. Legusha. „The Konstantinov effect and sound absorption in inhomogeneuos media". In: *Soviet Physics Uspekhi* 27.11 (1984).

[85]   F.F. Legusha. „Impedance effet of a liquid interface with allowance for the Konstantinov effect". In: *Sovjet Physics Technical Physics* (1984).

[86]   A. Ya Savel'ev. „Konstantinov effect in certain acoustical problems". In: *Sovjet Physical Acoustics* 19.2 (1973).

[87]   M. Bruneau et al. „General formulation of the dispersion equation in bounded visco-thermal fluid, and application to some simple geometries". In: *Wave Motion* 11.5 (Sept. 1989), pp. 441–451.

[88]   L. Fritsche. „Präzisionsmessung der klassischen Schallabsorption mit hilfe des Zylinderresonators (I)". In: *Acustica* 10.4 (1960).

[89]   T. Yazaki, Y. Tashiro, and T. Biwa. „Measurements of sound propagation in narrow tubes". In: *Proceedings of the Royal Society A: Mathematical, Physical and Engineering Sciences* 463.2087 (Aug. 2007), pp. 2855–2862.

[90]   C. Zwikker and C. W. Kosten. *Sound absorbing materials*. 1949.

[91]   H. Tijdeman. „On the propagation of sound waves in cylindrical tubes". In: *Journal of Sound and Vibration* 39.1 (Mar. 1975), pp. 1–33.

[92]   P. T. Tsilingiris. „Thermophysical and transport properties of humid air at temperature range between 0 and 100˚C". In: *Energy Conversion and Management* 49.5 (May 2008), pp. 1098–1110.

[93]   Baron Rayleigh John William Strutt. *The theory of sound*. Vol. 2. London Macmillan and CO, 1878.

[94]   John Miles. „The Reflection of Sound due to a Change in Cross Section of a Circular Tube". In: *The Journal of the Acoustical Society of America* 16.1 (1944), p. 14.

[95]   J. Kergomard and A. Garcia. „Simple discontinuities in acoustic waveguides at low frequencies: Critical analysis and formulae". In: *Journal of Sound and Vibration* 114.3 (May 1987), pp. 465–479.

[96]   D. Ronneberger. „Experimentelle untersuchungen zum akustischen reflexionsfaktor von unstetigen querschnittsanderungen in einem luftdurchströmten rohr". In: *Acustica* 19 (1967), pp. 222–235.

[97]   A. Cummings. „Sound transmission at sudden area expansions in circular ducts, with superimposed mean flow." In: *Journal of sound and vibration* 38 (1975), pp. 149–155.

[98]   A. Cummings. „Sudden area change in flow ducts: Further thoughts". In: *Journal of sound and vibration* 54 (1977), pp. 611–612.

[99]   Renzo Arina. „Validation of a Discontinuous Galerkin Implementation of the Time-Domain Linearized Navier–Stokes Equations for Aeroacoustics". In: *Aerospace* 3.1 (Feb. 2016), p. 7.

[100]   S. Föller and W. Polifke. „Identification of aero-acoustic scattering matrices from large eddy simulation. Application to a sudden area expansion of a duct". In: *Journal of sound and vibration* 331 (2012), pp. 3096–3113.

[101]   A. Kierkegaard, S. Boij, and G. Efraimsson. „Simulations of the scattering of sound waves at a sudden area expansion". In: *Journal of Sound and Vibration* 331.5 (2012), pp. 1068–1083.

[102]   G. Kooijman, A. Hirschberg, and Y. Aurégan. „Influence of mean flow and geometrical ratio on scattering of sound at a sudden area expansion in a duct". In: *Journal of sound and vibration* 329 (2010), pp. 607–626.

[103]   Susann Boij. „Flow effects on the acoustic end correction of a sudden in-duct area expansion". In: *The Journal of the Acoustical Society of America* 126.3 (2009), pp. 995–1004.

[104]   I. D. J. Dupére, re, and A. P. Dowling. „Absorption of Sound near Abrupt Area Expansions". In: *AIAA Journal* 38.2 (Feb. 2000), pp. 193–202.

[105]   I.D.J. Dupére and A.P. Dowling. „The absorption of sound near abrupt axisymmetric area expansions". In: *Journal of sound and vibration* 239.4 (2001), pp. 709–730.

[106]   R. F. Lambert. „Acoustic synthesis of a flowduct area discontinuity". In: *The Journal of the Acoustical Society of America* 67.1 (1980), p. 59.

Bibliography

[107]   D. Ronneberger. *Theoretische und experimentelle Untersuchung der Schallausbreitung durch Querschittssprünge und Lochplatten in Strömungskanälen*. Tech. rep. Drittes Physikalisches Institut der Universität Göttingen, 1987.

[108]   S. Boij and B. Nilsson. „Scattering and absorption of sound at flow duct expansions". In: *Journal of Sound and Vibration* 289.3 (2006), pp. 577–594.

[109]   D.G. Crighton. „Radiation Properties of the semi-infinite vortex sheet". In: *Proceedings of the Royal society of London. Series A, Mathematical and Physical Sciences* 1581 (330 Oct. 3, 1972), pp. 185–198.

[110]   A. M. Cargill. „Low-frequency sound radiation and generation due to the interaction of unsteady flow with a jet pipe". In: *Journal of Fluid Mechanics* 121.-1 (Aug. 1982), p. 59.

[111]   M. S. Howe. „Attenuation of sound in a low Mach Number nozzle flow". In: *Journal of Fluid Mechanics* 91.02 (Mar. 1979), p. 209.

[112]   A. Michalke. „On spatially growing disturbances in an inviscid shear layer". In: *Journal of Fluid Mechanics* 23.03 (Nov. 1965), p. 521.

[113]   D. Ronneberger and C. D. Ahrens. „Wall shear stress caused by small amplitude perturbations of turbulent boundary-layer flow: an experimental investigation". In: *Journal of Fluid Mechanics* 83.03 (Dec. 1977), p. 433.

[114]   Harold Levine and Julian Schwinger. „On the Radiation of Sound from an Unflanged Circular Pipe". In: *Physical Review* 73.4 (Feb. 1948), pp. 383–406.

[115]   C.L. Morfey. „Sound transmission and generation in ducts with flow". In: *Journal of Sound and Vibration* 14.1 (Jan. 1971), pp. 37–55.

[116]   Y. Aurégan and R. Starobinski. „Determination of acoustical energy dissipation production potentiality from the acoustical transfer function of a multiport". In: *Acta acustica* 85 (1999), pp. 788–792.

[117]   Xiaoha Wu and Parviz Moin. „A direct numerical simulation study on the mean velocity characteristics in turbulent pipe flow". In: *Journal of Fluid Mechanics* 608 (July 2008).

[118]   Ascher H. Shapiro. *The dynamics and thermodynamics of compressible flow*. Vol. 2. 1954.

[119]   C. Lahiri et al. „Attenuation of sound in wide ducts with flow at elevated pressure and temperature". In: *Journal of Sound and Vibration* 333.15 (July 2014), pp. 3440–3458.

[120]   Andreas Holmberg, Mats Åbom, and Hans Bodén. „Accurate experimental two-port analysis of flow generated sound". In: *Journal of Sound and Vibration* 330.26 (Dec. 2011), pp. 6336–6354.

[121]   Lewis F. Moody and N.J. Princeton. „Friction factors for pipe flow". In: *Transactions of the ASME* 66.8 (1944), pp. 671–684.

[122]   Y. Aurégan, A. Debray, and R. Starobinski. „Low frequency sound propagation in a coaxial cylindrical duct: application to sudden area expansions and to dissipative silencers". In: *Journal of Sound and Vibration* 243.3 (June 2001), pp. 461–473.

[123]   G. Kooijman et al. „Multimodal method for scattering of sound at a sudden area expansion in a duct with subsonic flow". In: *Journal of sound and vibration* 310 (2008), pp. 902–922.

[124]   S. Boij and B. Nilsson. „Reflection of sound at area expansions in a flow duct". In: *Journal of Sound and Vibration* 260.3 (2003), pp. 477–498.

[125]   P. Bradshaw. *Experimental Fluid Mechanics Second Edition*. Pergamon Press, 1970.

[126]   *Evaluation of measurement data - Guide to the expression of uncertainty in measurement*. Tech. rep. Bureau International des Poids et Mesures, 1995.

[127]   National Aeronautics and space administration. *Measurement uncertainty analysis principles and methods, NASA Measurement Quality Assurance Handbook - ANNEX 3*. Tech. rep. NASA-HDBK-8739.19-3. 2010.

[128]   *Agilent E1434A 4-Channel 25.6 kHz Arbitrary Source Technical Specifications*. Agilent Technologies.

[129]   *Manual for Swema 3000*. Version 1151 5.21. Swema AB.

[130]   *Microphone Handbook*. BE 1447-11. Brüel & Kjær. 1996.

[131]   *Product Data Quarter inch Pressure- Field Microphone Type 4938*. Brüel and Kjær.

[132]   *The NEXUS ™Range of Conditioning Amplifiers Types 2690, 2691, 2692 and 2693 User Manual: Operation and Interface*. BE 1522-13. Brüel Kjær. 2007.

[133]   *Agilent E1432A 4-16 Channel 51.2 kSa/s Digitizer plus DSP*. Agilent Technologies.

[134]   Michael Burger and Jozef Repiský CSc. „Problems of Linear Least Square Regression And Approaches to Handle Them". In: *Advanced Research in Scientific Areas*. 2012.

[135]   Kenneth M. Hanson. „Probabilistic Interpretation of Peelle's Pertinent Puzzle and its Resolution". In: *AIP Conference Proceedings* (2005).

[136]   Tom Burr et al. „Defense of the Least Squares Solution to Peelle's Pertinent Puzzle". In: *Algorithms* 4.4 (Feb. 2011), p. 2839.

[137]   Tom Burr et al. „Alternatives to the Least Squares Solution to Peelle's Pertinent Puzzle". In: *Algorithms* 4.2 (June 2011), pp. 115–130.

[138]   D. Neudecker et al. „Adequate Treatment of Correlated Experimental Data in Nuclear Data Evaluations Avoiding Peelle's Pertinent Puzzle". In: *Nuclear Data Sheets* 118 (Apr. 2014), pp. 364–366.